

---

[All ETDs from UAB](#)

[UAB Theses & Dissertations](#)

---

2006

## **Carbon microballoons and syntactic foams: Microstructure and properties.**

Kipp B. Carlisle  
*University of Alabama at Birmingham*

Follow this and additional works at: <https://digitalcommons.library.uab.edu/etd-collection>

---

### **Recommended Citation**

Carlisle, Kipp B., "Carbon microballoons and syntactic foams: Microstructure and properties." (2006). *All ETDs from UAB*. 5568.

<https://digitalcommons.library.uab.edu/etd-collection/5568>

This content has been accepted for inclusion by an authorized administrator of the UAB Digital Commons, and is provided as a free open access item. All inquiries regarding this item or the UAB Digital Commons should be directed to the [UAB Libraries Office of Scholarly Communication](#).

**CARBON MICROBALLOONS AND SYNTACTIC FOAMS:  
MICROSTRUCTURE AND PROPERTIES**

by

**KIPP B. CARLISLE**

**KRISHAN K. CHAWLA, COMMITTEE CHAIR  
RICHARD C. BRADT  
GARY M. GLADYSZ  
MATT LEWIS  
BURTON R. PATTERSON**

**A DISSERTATION**

**Submitted to the graduate faculty of The University of Alabama at Birmingham,  
in partial fulfillment of the requirements for the degree of  
Doctor of Philosophy**

**BIRMINGHAM, ALABAMA**

**2006**

UMI Number: 3253044

### INFORMATION TO USERS

The quality of this reproduction is dependent upon the quality of the copy submitted. Broken or indistinct print, colored or poor quality illustrations and photographs, print bleed-through, substandard margins, and improper alignment can adversely affect reproduction.

In the unlikely event that the author did not send a complete manuscript and there are missing pages, these will be noted. Also, if unauthorized copyright material had to be removed, a note will indicate the deletion.

**UMI**<sup>®</sup>

---

UMI Microform 3253044

Copyright 2007 by ProQuest Information and Learning Company.

All rights reserved. This microform edition is protected against unauthorized copying under Title 17, United States Code.

ProQuest Information and Learning Company  
300 North Zeeb Road  
P.O. Box 1346  
Ann Arbor, MI 48106-1346

# CARBON MICROBALLOONS AND SYNTACTIC FOAMS: MICROSTRUCTURE AND PROPERTIES

KIPP B. CARLISLE

## ABSTRACT

Microballoons (MBs) are used in many applications, ranging from drug delivery to syntactic foams; however, their mechanical properties and microstructures are little-studied and poorly understood at best. This research focuses primarily on characterizing carbon microballoons (CMBs) and, to a lesser degree, a three-phase syntactic foam in which CMBs and a bismaleamid binder are the major constituents. These MBs are classified by the manufacturer according to tap density (ASTM B 527). A nanoindenter, modified to do compression testing of individual CMBs, was used to study four different tap densities, 0.143, 0.166, 0.177 and 0.192 g/cm<sup>3</sup>. These tests yielded data that included failure load, failure strain, fracture energy, and stiffness for each CMB. The results of compression testing showed inter-tap density trends relating failure strain to diameter and failure load to stiffness. Intra-tap density comparison revealed trends toward increasing average wall thickness, failure load, and stiffness with increased tap density. Experimentation on the foams composed of CMBs from or near these tap densities revealed intra-tap density trends of increasing dynamic modulus with both bulk density and foam packing. Both optical and SEM quantitative microscopy have been used to evaluate the wall thicknesses and diameters of the MBs, and the volume fractions of various phases in the foam. Furthermore, microscopy results proved the existence of several important, undiscovered flaws in these CMBs, including through-wall thickness holes, joined CMBs, nested CMBs, and CMBs wherein the inner and outer wall surfaces were not concentric. Extensive finite element modeling, using ANSYS 8.0, of idealized

CMB microstructures was performed, simulating the experimental uniaxial compression testing procedure. Stress states at failure in these CMBs have been predicted for the average failure conditions of each tap density lot. Intra-tap density trends were found. Parametric studies involving the idealized microstructure's radii and wall thickness revealed that buckling and bending are both possible failure mechanisms for these CMBs. Experimental support for dual flaw populations was provided by Weibull statistics. Using this, failure maps were created and applied to the experimental data in an attempt to estimate the contribution of buckling failure. LA-UR-06-6129.

## ACKNOWLEDGMENTS

I would like to thank my advisor, Dr. K.K. Chawla, for his mentoring and guidance during my graduate career. I also appreciate the help, support, and attentiveness of the members of my graduate committee (Dr. R.C. Bradt, Dr. G.M. Gladysz, Dr. M. Lewis, and Dr. B.R. Patterson) throughout this work. Special thanks to the Research Engineer/Lab Manager for our research group, Mr. Mark Koopman, for his help, advice, and support. The assistance of the past and present members of our Composites Research Group at UAB (A. Goel, Dr. G. Gouadec, R. Kulkarni, L. McCall, B. Patel, A. Rossillon, and J. Zhang) was also appreciated during this endeavor. This research was financially supported by Los Alamos National Laboratory/ U.S. Department of Energy subcontract #44277-SOL—02 4X. Additionally, my personal thanks to the U.S. Department of Defense, for the National Defense Science and Engineering Graduate Research Fellowship that partially funded by graduate career.

I would like to gratefully acknowledge all of the help and encouragement I have received along this road from my parents, family, and friends. And finally, I am extremely grateful to Jessica Kilgore, not only for being herself, but also for having patience with me throughout this process.

## TABLE OF CONTENTS

	<i>Page</i>
ABSTRACT.....	ii
ACKNOWLEDGMENTS .....	iv
LIST OF TABLES .....	vii
LIST OF FIGURES .....	viii
INTRODUCTION .....	1
1. Foams .....	1
1.1. <i>Two-phase syntactic foams</i> .....	2
1.2. <i>Three-phase syntactic foams</i> .....	5
2. Microballoons .....	11
2.1. <i>Production of carbon microballoons by spray drying</i> .....	12
2.2. <i>Production of carbon microballoons by pyrolysis</i> .....	16
2.3. <i>Production of carbon microballoons via emulsion</i> .....	17
2.4. <i>Compression of filled microballoons</i> .....	18
3. Thermosetting Binders .....	19
4. Organization of Work .....	20
STRUCTURE AND MECHANICAL PROPERTIES OF MICRO AND MACRO BALLOONS: AN OVERVIEW OF TEST TECHNIQUES .....	24
CHARACTERIZATION OF CARBON MICROBALLOON SYNTACTIC FOAMS .....	57
CHARACTERIZATION OF THE BINDER PHASE IN A THREE-PHASE CARBON MICROBALLOON SYNTACTIC FOAM .....	71
MICROSTRUCTURE AND COMPRESSIVE PROPERTIES OF CARBON MICROBALLOONS .....	85
UNIAXIAL COMPRESSIVE PROPERTIES OF BISMALAMID-COATED CARBON MICROBALLOONS .....	112
FINITE ELEMENT MODELING OF THE UNIAXIAL COMPRESSION BEHAVIOR OF CARBON MICROBALLOONS I: IDEALIZED MODEL .....	126

TABLE OF CONTENTS (Continued)

	<i>Page</i>
FINITE ELEMENT MODELING OF THE UNIAXIAL COMPRESSION BEHAVIOR OF CARBON MICROBALLOONS II: FLAWED MICROSTRUCTURES.....	152
CONCLUSIONS.....	174
GENERAL LIST OF REFERENCES .....	178

## LIST OF TABLES

<i>Table</i>	<i>Page</i>
<b>CHARACTERIZATION OF CARBON MICROBALLOON SYNTACTIC FOAMS</b>	
1 Measured volume fraction of constituents in CMB foams. ....	67
<b>MICROSTRUCTURE AND COMPRESSIVE PROPERTIES OF CARBON MICROBALLOONS</b>	
1 Average Properties of CMBs by Category. ....	101
<b>UNIAXIAL COMPRESSIVE PROPERTIES OF BISMALAMID-COATED CARBON MICROBALLOONS</b>	
1 Average and standard deviation for the compressive properties of 0.192 g/cm <sup>3</sup> tap density CMBs. ....	121
<b>FINITE ELEMENT MODELING OF THE UNIAXIAL COMPRESSION BEHAVIOR OF CARBON MICROBALLOONS I: IDEALIZED MODEL</b>	
1 Material properties for FE models . ....	142
2 ANSYS elements used in CMB modeling.....	143
3 Boundary conditions for FEM .....	143
4 Weibull moduli for various tap density CMBs.....	143
<b>FINITE ELEMENT MODELING OF THE UNIAXIAL COMPRESSION BEHAVIOR OF CARBON MICROBALLOONS II: FLAWED MICROSTRUCTURES</b>	
1 Material properties for FE models.....	163
2 ANSYS elements used in CMB modeling.....	163
3 Boundary conditions for FEM .....	163

## LIST OF FIGURES

<i>Figure</i>	<i>Page</i>
<b>STRUCTURE AND MECHANICAL PROPERTIES OF MICRO AND MACRO BALLOONS: AN OVERVIEW OF TEST TECHNIQUES</b>	
1 Phenolic microballoons, showing size range and many broken balloons.....	45
2 GMBs (3M A16/500).....	45
3 0.177 g/cm <sup>3</sup> tap density CMBs, showing general spherical morphology. ....	46
4 Wall thickness measurement of CMB fragments. ....	46
5 Polished cross-section of CMBs mounted in epoxy. ....	47
6 Schematic of MB sectioned above its great circle. ....	48
7 Optical interferometry image of 0.143 g/cm <sup>3</sup> tap density CMBs mounted in epoxy, allows direct measurement of wall thickness.....	49
8 Laser confocal microscope image of 0.143 g/cm <sup>3</sup> tap density CMBs mounted in epoxy.....	49
9 Schematic of interference light microscope configuration use to measure wall thickness of transparent MBs. ....	50
10 Schematic of tap density test apparatus for ASTM B 527.....	50
11 Schematic of nanoindenter modified for use in compression testing of MBs. ....	51
12 Compression curves from MBs composed of different materials. ....	51
13 Possible types of compression behavior for brittle CMBs.....	52
14 Direct correlation of failure load to MB diameter for GMBs (3M A16/500). ....	52
15 Work of fracture correlated favorably with MB diameter for GMBs (3M A16/500). ....	53

## LIST OF FIGURES (Continued)

Figure	Page
16 Failure load vs. measured wall thickness for GMBs, showing $P_f \propto t^2$ .....	53
17 Strength vs. relative density squared for Al <sub>2</sub> O <sub>3</sub> macroballoons.....	54
18 Compression curve from isostatic testing of batches of MBs, as per ASTM D 3102. ....	54
19 Aspect ratio vs. isostatic buckling pressure for individual GMBs. ....	55
20 Optical image of CMBs used for nanoindentation. ....	55
21 Modulus vs. displacement curve for the indent in Fig. 20.....	56
 <b>CHARACTERIZATION OF CARBON MICROBALLOON SYNTACTIC FOAMS</b>	
1 Example micrograph for volume fraction determination.....	68
2 Schematic of the configuration for impulse excitation determination of Young's modulus. ....	68
3 Micrograph of carbon microballoon syntactic foam surface. ....	69
4 Modulus and bulk density vs. foam packing. ....	69
5 Modulus vs. bulk foam density.....	70
 <b>CHARACTERIZATION OF THE BINDER PHASE IN A THREE-PHASE CARBON MICROBALLOON SYNTACTIC FOAM</b>	
1 Chemical structure of cured APO-BMI. ....	79
2 DSC curve of neat APO-BMI.....	80
3 DSC curve for blend of 60 weight percent CMBs and 40 weight percent APO-BMI.....	81
4 DSC curve of cured syntactic foam. ....	82
5 Micrograph of <i>in situ</i> nanoindentation of APO-BMI. ....	83
6 Optical micrograph of nanoindentations in APO-BMI.....	84

## LIST OF FIGURES (Continued)

<i>Figure</i>		<i>Page</i>
<b>MICROSTRUCTURE AND COMPRESSIVE PROPERTIES OF CARBON MICROBALLOONS</b>		
1	Micrograph of 3-phase carbon microballoon (CMB) syntactic foam.....	102
2	Polished cross-section of CMB mounted in epoxy.....	102
3	Schematic illustrating sectioning a CMB either below or above its great circle.....	103
4	Schematic of nanoindenter modified for use in compression testing of CMB. ....	103
5	Sample compression curve for a single wall CMB, showing parameters extracted from graph.....	104
6	Micrograph showing variation in CMB size and morphology. ....	104
7	Polished cross-section of CMB foam. ....	105
8	Examples of different CMB compressive behavior based on CMB morphology.....	106
9	CMB diameter vs. wall thickness. ....	106
10	Calculated average CMB wall thickness vs. tap density. ....	107
11	Schematic representation of nested compression curve, with initial and ultimate properties labeled.....	107
12	Fracture energy vs. diameter for single wall CMBs, with bold lines for experimental and thin lines for calculated trends.....	109
13	Failure load vs. predicted thickness for single walled CMBs, revealing a parabolic dependence of failure load on thickness.....	109
14	Compressive strain trend for single wall CMBs.....	110
15	Load vs. pseudo-stiffness trend for all tap density single wall CMB.....	110
16	Schematic of speculated flaw size limitations in smaller diameter CMBs.....	111

## LIST OF FIGURES (Continued)

<i>Figure</i>	<i>Page</i>
<b>UNIAXIAL COMPRESSIVE PROPERTIES OF BISMALEAMID-COATED CARBON MICROBALLOONS</b>	
1	Compression curve for a single CMB.....121
2	Average property comparison for all four tap densities of CMBs.....122
3	Compressive strain at failure vs. CMB diameter for all tap densities. ....122
4	Failure load vs. pseudo-stiffness for all tap densities. ....123
5	Micrograph of APO-BMI coated CMBs, post-cure.....123
6	Micrograph of APO-BMI-coated CMB fragments.....124
7	Compressive strain at failure vs. CMB diameter for uncoated and APO-BMI coated, cured 0.192 g/cm <sup>3</sup> tap density CMBs. ....124
8	Failure load vs. pseudo-stiffness for uncoated and APO-BMI coated, cured 0.192 g/cm <sup>3</sup> tap density CMBs. ....125
9	Representative confined compression curves for bulk uncoated CMBs and three-phase CMB foams.....125
<b>FINITE ELEMENT MODELING OF THE UNIAXIAL COMPRESSION BEHAVIOR OF CARBON MICROBALLOONS I: IDEALIZED MODEL</b>	
1	Experimental compressive strain at failure vs. radius for all tap density CMBs. ....144
2	$\sigma_{\text{von}}$ distributions. ....145
3	$\sigma_p$ distributions.....146
4	Predicted FE stress distributions for 3D model of 0.143 g/cm <sup>3</sup> tap density. ....147
5	Buckled and unbuckled stress distributions for CMB of R = 10.99 $\mu\text{m}$ .....148
6	Failure mechanism map for CMBs. ....149
7	Compressive strain vs. R/t for minimum, maximum, average with standard deviation, and critical values. ....150

## LIST OF FIGURES (Continued)

<i>Figure</i>	<i>Page</i>
8 Weibull plot of CMB compressive failure strains, for CMBs of three different tap densities.....	151
<b>FINITE ELEMENT MODELING OF THE UNIAXIAL COMPRESSION BEHAVIOR OF CARBON MICROBALLOONS II: FLAWED MICROSTRUCTURES</b>	
1 Representative micrographs of flawed CMBs.....	164
2 $\sigma_{\text{von}}$ distribution for CMB of $R = 20 \mu\text{m}$ and $t_{\text{avg}} = 1.67 \mu\text{m}$ , with thin region on loading axis.....	165
3 $\sigma_{\text{p}}$ distribution for CMB of $R = 20 \mu\text{m}$ and $t_{\text{avg}} = 1.67 \mu\text{m}$ , with thin region on loading axis.....	166
4 $\sigma_{\text{von}}$ distribution for CMB of $R = 20 \mu\text{m}$ and $t_{\text{avg}} = 1.67 \mu\text{m}$ . ....	167
5 $\sigma_{\text{p}}$ distribution for CMB of $R = 20 \mu\text{m}$ and $t_{\text{avg}} = 1.67 \mu\text{m}$ . ....	168
6 Schematic of 3D models. ....	169
7 Effect of hole position on $\sigma_{\text{von}}$ . ....	170
8 Effect of hole position on $\sigma_{\text{p}}$ . ....	171
9 Effect of varying wall thickness on $\sigma_{\text{von}}$ distribution around hole in MB wall. ....	172
10 Effect of varying wall thickness on $\sigma_{\text{p}}$ distribution around hole in MB wall. ....	173

## INTRODUCTION

### 1. Foams

All foams are structures composed of three-dimensional arrangements of voids amongst structural components. While technically the structural members surrounding the voids could be liquid, as is the case for froth, we will only consider solid foams here. Foam may be conceptualized as a collection of hollow structural cells. The aggregate of cells for traditional foams can completely enclose the internal voids to form a closed-cell foam, partially enclose the internal voids such that an open-cell foam results, or it may be a combination of the two. Traditional foams are formed via a variety of blowing processes, where a liquid is forced to solidify containing entrapped gas. The gas may have been introduced into the melt by either mechanically mixing or by evolution from the decomposition reaction of a solid or liquid blowing agent. There are, however, other types of foams besides the blown varieties. One category of non-traditional foam is produced by bonding together previously formed hollow particles. The foams made from hollow particles exist in two primary subcategories: sintered foams and syntactic foams. Sintered foams result when a packed arrangement of hollow particles is heated and diffusionally bonded together to form a foam [1]. The other type, syntactic foams, will be described in detail below, since it is the focus of this research.

Syntactic foams are usually a type of polymer matrix composite, but they may also be metal matrix or even ceramic matrix composites, depending on the application. The name itself, syntactic — meaning to arrange, is insightful into the production

process for these foams. In syntactic foams, the voids are incorporated via the introduction of microballoons (MBs) — namely small, hollow, spherical shells. These foams are lightweight and often have very high specific properties because of their low densities, making them ideal cores for beams for use in transportation, aerospace, and defense applications. Syntactic foams may be classified as two-phase, three-phase, or multiphase, with the demarcation delineated by their void contents. A two-phase foam consists of MBs surrounded by a continuous, nominally void-free matrix material, whereas a three-phase foam has an intentionally void-filled, matrix (often termed binder) that may only be sufficient to coat the MB surfaces and pool at the inter-MB contact locations. Multiphase foams merely build upon two- or three-phase foams by adding additional reinforcing phases to the foam, namely fibers, particles, whiskers, etc. [2-6].

### *1.1. Two-phase syntactic foams*

While two-phase foams are not the primary subject of this research, it is important to understand their behavior. There are numerous studies of these materials in the literature, expounding upon a wide variety of subjects, including production techniques, tensile testing, flexural strengths, compressive properties, impact behavior, and the effect of fiber reinforcements [2, 3, 7-21]. Some researchers, instead of performing the common variational study on the effect of different MB and matrix volume fractions [2, 12, 20, 22, 23], have varied the MB content by its location within the foam [24-26]. Some have even evaluated the effect of different MB wall thicknesses and radii on the strength of the syntactic foams [22, 27-29]. While a detailed review of this literature is outside the scope of this dissertation, a synopsis of the general trends will be presented.

The effect of adding MBs to a neat thermosetting polymer has proven to provide improved mechanical properties to the newly-formed composite, as compared to the neat polymer. Several studies have reported increases in compressive strength of 50 % over the neat polymer matrix, although the effect on compressive modulus is less pronounced. Additionally, both increases and decreases in tensile and flexural strength and modulus have been reported, depending on the volume fraction of the foam's constituents [2, 12, 15, 20, 23].

The focus of most research, however, has not been to determine the effect of creating syntactic foam from a neat polymer, but rather to investigate the changes in syntactic foam properties induced by varying the constituents of the syntactic foam. Many researchers have studied the variation of two-phase foam properties with increasing microballoon volume fraction. Indeed, the volume fraction of microballoon reinforcement is seen as one of the major controllers of two-phase foam properties [2, 12, 20, 22, 23]. The other key property seems to be the nature of the microballoons themselves, i.e., their wall thickness, radius, and composition. Most syntactic foams seem to use glass microballoons (GMBs), but there are foams using polymer microballoons (PMBs), carbon microballoons (CMBs), metallic microballoons, or other ceramic microballoons, for instance fly ash cenospheres. Some important research on these foams involves the effect of the MB radius to wall thickness ratio on the foam properties. Fine et al. [22], Gupta et al. [28, 29], and Woldesenbet et al. [18] have determined that foams produced with a constant volume fraction of MBs may still have variable density, by varying the wall thickness of the MBs. In these materials, the microballoons with the higher wall thicknesses yielded foams with higher compressive strengths and moduli,

with little change in tensile or flexural properties [18, 22, 27-29]. Indeed, it has been claimed that changing the wall thickness of the MBs is “more effective than changing the microballoon volume fraction to change the syntactic foam density as it considerably increases the strength to the weight ratio” [27].

Multi-phase foams originating from two-phase foams have also been well characterized by various researchers. Apparently, the most common additional reinforcements are glass fiber, nanoclay, and rubber [15, 30-39]. The addition of glass fibers significantly increases the tensile, flexural, and compressive strengths and moduli of two-phase foams [15, 31, 35-38]. These results were hardly surprising, since the addition of fibers to a two-phase syntactic foam is essentially transforming it into an MB-containing fiber reinforced plastic (FRP), although with lower fiber loading than most FRPs. The goal of the other two major additions, nanoclay and rubber, was to increase the toughness of the system. Nanoclay or rubber particle additions, when properly dispersed in a resin, have proven to be effective tougheners in many polymer systems, for instance the highly commercialized rubber toughened acrylonitrile-butadiene-styrene system. Thus, researchers have successfully increased the toughness, as measured by the area under the stress-strain curve, of many two-phase syntactic foams by small (2-5 volume %) nanoclay or rubber additions to the polymer matrix. These toughness increases are often anywhere from 80 to 200 % and are achieved without decreasing other mechanical properties of the material [30, 32-34, 39].

## 1.2. Three-phase syntactic foams

Three-phase syntactic foams, the primary focus of this literature review, are a much less used and studied variety of syntactic foam than their two-phase counterparts. However, there is evidence that this should not be the case. Following Gibson and Ashby [1], for a given strength part, the highest bending stiffness is achieved by the greatest volume fraction of MBs, i.e., “the structural integrity of the materials is retained at a minimum binder amount [15].” This is a powerful argument favoring the use of three-phase syntactic foams over their two-phase counterparts, yet they are still under-utilized, as evidenced by the quantity of research available on each type. Originally, this disparity may have stemmed from the later origins of the three-phase system, which was only formally defined in the 1970s by Price and Nelson [6]. They defined the three-phase foam as “an aggregate of microspheres bonded together by a *small* [emphasis added] amount of polymer which may not form a continuous phase [6].” A ternary phase diagram was constructed to describe syntactic foams, wherein two-phase foams fell along the MB-binder (matrix) binary, and three-phase foams existed in the space of the diagram. Thus, binary sections are required to investigate the properties of these foams, suggesting that composition should be a more important characterization tool than density for three-phase foams [6].

The earliest available research on three-phase foams dates from the early 1970s, although upon perusal, it is clear that work was underway on these materials in the late 1960s, as evidenced by several British and Belgian patents or patent applications cited by Thomas [5]. Thomas [5] does an excellent job of describing the types of microballoons and binders employed at the time in the construction of what are termed carbon

syntactics, with lesser attention given to carbon/resin syntactics. The difference is that carbon syntactics consist of carbonized microballoons and carbonized binder, producing an entirely carbonaceous material with only trace amounts of other elements, whereas carbon/resin syntactics are the more traditional mixture of carbon microballoons and a polymeric binder. Carbon syntactics were designed for high temperature insulating and structural properties. Their manufacturing routes were described in detail, both when forming from CMBs and a precursor resin and when starting from PMBs and a precursor resin. In both cases, the key step is pyrolysis of the molded foam structure at suitably slow rates to convert the polymer constituents into carbon. Some generalities regarding the density, thermal conductivity, and electrical conductivity of these materials were presented, but little mechanical property data were given [5].

Benton and Schmitt [4] provide an account of the characterization of carbon-based syntactic foam. They reported on the manufacturing of a high temperature insulation that also possessed low density and high compressive strength. CMBs or PMBs were mixed with a thermosetting binder of furfuryl alcohol, maleic anhydride, pitch, and acetone. This blend was then molded to the desired shape and heat treated in argon at 900 °C to carbonize the binder. Characterization of the resulting foam was performed via compression testing and scanning electron microscopy (SEM). Compressive strength of all foam samples increased linearly with foam density, and foams composed of MBs of different average wall thickness followed different trendlines. Analysis of the relation between these trends showed that foams of thinner-walled MBs had higher specific properties. Finally, comparison between carbon syntactics in which CMBs were used and those in which PMBs were carbonized

simultaneously with the binder showed that simultaneous carbonization led to stronger foams, presumably because of better bonding between the MB and binder [4].

Extensive research work on three-phase syntactic foams is due to the research group of Narkis, Putterman, Kenig, Gerbovich and Boneh [40-45], who published extensive studies on phenolic MBs or GMBs mixed with varying volume fractions of polyimide (Kerimid 601) or epoxy binders. These six papers cover preparation and characterization of syntactic foams through a variety of techniques.

The common liquid infiltration technique used for two-phase foam processing can also be employed for three-phase foams [45], but more attention is given to powder mixing. This powder process, used to manufacture the foams currently under investigation, consists of two main foam formation steps. First, the desired quantity of solid binder (in particle form) is combined with the corresponding necessary amount of MBs and blended thoroughly. Gentle mixing is recommended to avoid MB breakage. The second major step is molding. The desired amount (by weight) of mixed, solid solution is placed into a mold of known volume (hence allowing the desired final part density to be achieved), followed by heating of the mold, often under pressure, to cure the thermosetting binder. The curing temperature profile will depend on the curing behavior of the binder. It is reported [45] that the addition of a liquid to the mixing step often aids in powder/MB dispersion, although the fluid must then be evaporated from the mixture before molding. Mechanical property characterization of these foams was also performed via compression testing [41, 43]. The compressive strength and modulus were observed to increase with both increasing foam density and increasing volume fraction of binder. The rate of increase was greatest at low density and low volume fractions of resin, with

the (logarithmic) trendlines leveling off at resin volume fractions greater than 0.26. Additionally, compression was performed at several temperatures. The compressive modulus was seen to decrease with temperature more rapidly than the compressive strength, emphasizing the softening of the resin at higher temperature [41, 43-45].

A third, advantageous, production method involved the coating of the MBs with the binder, and then using the resin coated spheres to mold the foam. The key benefits included a more uniform distribution of the binder throughout the resulting foam structure and elimination of the powder mixing step, which so easily resulted in broken MBs. This procedure would begin by dissolving the polymer in solvent and adsorbing a thin film of the resulting solution onto the MB surfaces. The solution plus MB slurry would then be vacuum filtered and rinsed, to obtain a thin film of precipitated polymer uniformly coating the MB surface. Once the coated MBs were vacuum dried, mold filling could commence. It was shown that the compressive and flexural properties of foams formed via this technique were similar to those from powder mixing, and the uniformity of the coating and foam properties suggested that this method would be superior to powder techniques for large parts [40, 41, 44].

A final method of producing three-phase syntactic foams is rotational molding. In this technique, a powder mixing approach is followed, where powdered binder and MBs are charged into a commercial rotational molding machine. The resulting foam parts consisted of loose-packed MBs and therefore were of lesser density than those produced in the other techniques for forming three-phase syntactic foams, although complex part designs are possible. This type foam revealed that compressive strength and modulus were linear functions of resin weight fraction and logarithmic functions of bulk density.

Comparison to three-phase foams produced by powder mixing or MB coating revealed similar properties in the limited range of densities where a syntactic foam could be formed by all three techniques.

In more recent three-phase syntactic foam research, Bruneton et al. [46] studied an all-carbon three-phase foam, composed of CMBs and a carbonized phenolic binder in compression under various temperatures from ambient up to 3000 °C. They observed, in compression, initial linear elastic behavior, followed by a trend toward ductile behavior as the test temperature was increased. Observations showed that the main cause of failure in the foams was the binder. Elastic deformation in both CMBs and binder occurred on loading, until the critical load for crack propagation in the binder was reached. Beyond this point, “plasticity” was determined to result from binder cracking, with foam failure occurring only after enough binder to MB linkages were destroyed [46].

Both McEachen [47] and Gladysz et al. [48] conducted extensive studies on variants of the CMB syntactic foams. McEachen [47] detailed the basic production procedures for producing CMB foam billets, from mixing of the bismaleamid (APO-BMI) binder pre-polymer with the MBs, to the molding and curing process for the foam billet. Additionally, mechanical testing of the resulting foams was conducted in compression. The failure stresses ranged between 1.38-6.89 MPa, with all values below 4.83 MPa indicating an unacceptable production part. Subsequent processing changes to the foam cure cycle increased strength to as high as 10.34 MPa. McEachen [47] also measured the thermal conductivity to be  $0.22 \text{ W m}^{-1}\text{K}^{-1}$ , and the heat capacity as  $1.004 \text{ J g}^{-1}\text{K}^{-1}$  via DSC [47].

Gladysz et al. [48] performed considerable characterization on these foams. Their results include compression and flexural testing of foams with varying CMB tap density and varying foam bulk density. In compression, elastic loading followed by a long plateau of graceful failure was observed, with the failure mode being fracture of both CMB and APO-BMI. The trend of increased strength and modulus with increased volume percent CMBs was observed, and higher tap density CMBs produced a higher strength and modulus as well. However, when the same strength and modulus data were re-plotted versus bulk density of the foam, the foams of the lower tap density showed higher strengths and moduli at any given bulk density. Thus, the packing arrangement of the lower tap density CMBs in the structure affects foam performance. In three-point bend testing, different results were documented. Linear elastic loading was seen, but failure was brittle at very low strains. Strength and modulus of the foam again increased with greater volume percent of CMBs, but this time there was no difference between the tap densities. When the data were plotted as a function of bulk foam density, the flexural strength was about the same for different CMB tap densities, but the modulus data showed lower tap densities to have higher modulus at a given bulk foam density. The explanation for this, which agrees with other findings on a GMB syntactic foam of the same type [49], was that a major factor controlling failure of the foams in flexure is binder-CMB interfacial failure. The lower tap density CMBs, which were packed into the structure more tightly, possessed a greater number of shorter APO-BMI ligaments, and hence distributed the loading across a larger interfacial area [48].

## 2. Microballoons

Microballoons (MBs), often called cenospheres, microbubbles, or hollow microspheres, are hollow spherical shells that may be composed of ceramics, polymers, or even metals. Microballoons were originally viewed as fillers for plastics, reducing the amount of polymer used in a product. While many MB manufacturers still emphasize this role, the reinforcement value of microballoons is also being realized. MBs are now considered a reinforcement phase in many composites that can significantly increase specific properties, especially compressive and impact strengths. Additionally, MBs can be used in adhesives, washing powders, drug delivery, and water testing. Of this myriad of uses, one, syntactic foam, is the focus of this research [2, 3].

One of the first steps to understanding the microstructure and mechanical properties of a material is to acquire the basic background about it. In the present research, this means that significant background information on the production and testing of microballoons needs to be acquired. Specifically, what are the manufacturing processes that are used in CMB production? How do these processes affect the morphology of the resulting MBs? What experimental techniques may be used to quantitatively and qualitatively evaluate the morphology and mechanical properties of MBs? These are the questions to be addressed in the following subsections, where an overview of the literature on microballoon production and testing will be provided, with one exception—many MB test techniques are detailed in a later chapter, and this information will not be duplicated in the literature review.

### *2.1. Production of carbon microballoons by spray drying*

Spray drying is defined as, “the transformation of feed [material] from a fluid state into a dried particulate form by spraying the feed material into a hot drying medium” [50]. This process was first conceived in 1865, was patented in 1872, and became of commercial significance in the food and household goods market as early as the 1920s.

The basic setup for any spray drying procedure consists of two primary mechanisms, as suggested by the name itself. The spraying process actually goes by the term atomization, referring to the breakup of the liquid feed material into small discrete droplets. Under normal conditions, these droplets are small spheres, but in MB production, the process is often termed foam spray drying, referring to the hollow nature of the particles created during atomization. Usually, this hollowness is imparted by a trapped gas, which is formed from additives placed in the material feed for just such a purpose. Thus, the term foaming is indeed correct. The drying of the atomized material is usually accomplished via the application of a heated atmosphere, together with humidity control applied to the atmosphere so that evaporation of moisture can occur—this evaporation would be necessary for polymeric solutions, but not for metals. Once dried, the end product is then recovered from the drying medium, sorted, etc.

Atomization may be achieved by two methods, disk or nozzle atomization. These are further categorized as either pressure, centrifugal, kinetic, or sonic. The main reason for selecting a specific type is that each type produces a different particle size and particle size distribution. Generally, rotating disk atomizers produce a fine particle size (30-120  $\mu\text{m}$ ), with nozzles yielding coarser particles (120-250  $\mu\text{m}$ ) but better control over the

distribution width, e.g., narrow distribution widths are possible with this method. Another selection criterion is the volume of material that must be produced. Larger volumes lend themselves more to the centrifugal methods, i.e., the rotating disk atomizer [50]. This is the method prescribed by Veatch and Burhans [51] in their patent governing the production of microballoons. They described the production of hollow particles of any film-forming material via the addition of a latent gas to a solution containing a volatile solvent. During atomization of this solution, the outer layers of the droplets formed will quickly dry in the heated atmosphere, while the simultaneous evolution of the latent gas within the dried shell expands, forming and maintaining an internal hollow. Thus, the internal pressure of the latent gas prevents collapse of the hollow, drying particle by atmospheric pressure. The latent gas may be any form of material added to the feedstock which has the desired gas-forming effect. Examples are carbonates, sulfites, and ammonium salts, which produce blowing gases when small amounts of acids are introduced into the system. The patent defined the film-forming materials for which it functions to be limited only by the materials' ability to form a strong skin on evaporation from solution. Thus, organics like cellulose acetate may form microballoons, as can most thermoplastics and thermosets. Even inorganics like sodium silicates and polyborates are included in the patent's definition of film-forming materials suitable for microballoon production [51].

Aside from the addition of the blowing agent, the general atomization techniques of spray drying apply for microballoon production. The resulting particles are often analyzed via sieving and statistics for mean particle size, particle size distribution, and distribution type, e.g. normal, log normal, empirical, etc. [50]. Veatch and Burhans [51]

found that the concentration of the film-former was not that important, although it did directly control mean particle size. Flotation testing of the final product was used to prove that the particles were indeed hollow and hole-free.

Analytically, some of the relevant production parameters may be predicted. Of especial importance is the relationship between the particle size ( $D_1$ ) and droplet size ( $D_2$ ) from atomization, given by the following expression

$$D_1 = D_2 \sqrt{\frac{d}{p\rho}} \quad (1)$$

in terms of the particle density ( $d$ ), the solution density ( $\rho$ ), and the weight fractional concentration of the solution ( $p$ ). This equation is merely a rearrangement of one of the several equations for a disk atomizer. All have the general form:

$$\frac{A_1}{A_2} = \left( \frac{B_1}{B_2} \right)^n \quad (2)$$

where  $A_1$  and  $A_2$  are two droplet or particle sizes,  $n$  is a fractional power that depends on the process and parameter, and  $B_1$  and  $B_2$  are any of the following variables for two different runs of solution: wheel speed ( $N$ ), feed rate ( $M$ ), solution viscosity ( $\mu$ ), solution surface tension ( $\sigma$ ) and solution density ( $\rho$ ). Typical values for  $n$  range between 0.1 and 0.5.

The other equations of interest are those that govern the particle velocity (in ms) in the tangential ( $V_t$ ) or radial ( $V_r$ ) directions, given by

$$V_r = 0.0024 \left( \frac{\rho \pi^2 N^2 d Q^2}{\mu h^2 n^2} \right)^{\frac{1}{3}} \quad (3)$$

$$V_t = \pi d N \quad (4)$$

where the terms are: density ( $\rho$ ), diameter ( $d$ ), feed rate ( $Q$ ), rotational speed of atomizer disk ( $N$ ), viscosity ( $\mu$ ), number of vanes on the atomizer disk ( $n$ ), and vane height ( $h$ ). They can be summed vectorially to find the overall velocity [50].

Drying too is covered by the patent. In this patent, the inventors specified that the drying of MBs take place in a drying tower, using air or other heated gas as the drying media [51]. The standard variables in the drying step of spray drying are the gas flow, heat and mass balance, and residence time in the drying chamber. Of course, these parameters will be calculated differently based upon the gas used, and whether the drying gas flow is with the atomizer particle flow, against the particle flow, or of mixed character. As Veatch and Burhans [51] prescribed that the drying gas be air flowing concurrently with the atomized droplets, the simplest form of the equation for droplet evaporation time—and hence the drying time during which a droplet would need to be kept suspended in the drying tower—is:

$$t = \frac{\lambda \rho_l}{2\Delta T} \int_{D_1}^{D_0} \frac{D \, d(D)}{2K_d} \quad (5)$$

This equation is in terms of the time ( $t$ ), droplet size ( $D$ ), temperature difference in the droplet and the gas, the density of the liquid ( $\rho_l$ ), and the thermal conductivity of the film around the droplet ( $K_d$ ). This is the simplest case, considering only heat transfer effects. Consideration of the velocity difference between particles and drying gas or of the deceleration of the droplets causes the equations become much more complicated [50, 52, 53]. Meanwhile, even an estimate of drying time, like that in Eqn. 5, does provide, when combined with particle velocity, the ability to determine the necessary size of the drying chamber. It should be large enough in diameter that particles do not impact the walls

during the initial stage of drying and tall enough so that sufficient drying of the particles will have occurred upon settling to its bottom [50].

The spray drying method for MB production is the oldest, and still most heavily used, method for MB production [53]. It is the method of production used by Asia Pacific for the precursor phenolic MBs, trade named Phenoset, from which the CMBs used in this work were derived. The CMBs from these precursors were produced at Honeywell Aircraft Landing Systems (South Bend, IN). The process involves a proprietary high-temperature carbonization step [47, 48]. The end result of this carbonization treatment is the conversion of the phenolic MB carbon MB.

Although the CMBs studied here were produced by disk atomizer spray drying, it may be instructional to provide an additional overview of other, more recently developed methods of producing CMBs. Currently, MBs are produced using ultrasonic nozzle atomizers, where the momentum of the particles is greatly reduced during atomization, and thus smaller drying chambers may be used. This process is now at the stage where it may yield MBs of as small or smaller than MBs produced by the disk atomization technique, but with both a narrower size distribution and less defects in the balloons [52].

## *2.2. Production of carbon microballoons by pyrolysis*

Sharon et al. [54] manufactured and characterized carbon nanobeads of both solid and hollow geometries using a pyrolysis technique. Carbon can be formed from any number of organic precursors, i.e., pitch, rayon, etc., or from synthetic polymer sources. Of interest in this technique is the pyrolysis of camphor under controlled conditions. Camphor is  $C_{10}H_{16}O$ , when pyrolyzed, converts to a double ring structure that is highly

reactive, and readily suited to the formation of curved carbon structures. Sharon et al. [54] used a container of camphor mixed with ferrocene, heated it to 50 °C to produce vapor, and then forced the vapors into a quartz tube at 1000 °C in a furnace with a flow of argon. The flow rate was kept to 0.0131 l/s. The end result was a 30 % yield of an amorphous carbon material deposited on the inside of the quartz tube. FTIR and XRD analysis showed the nanobeads to be amorphous, with a thin graphitic shell. SEM and TEM observations showed that the novel production technique led to CMBs of 250 nm and 500 nm sizes [54].

### *2.3. Production of carbon microballoons via emulsion*

An emulsion technique has been used to produce CMBs in a most unusual manner. The CMBs were the byproduct that remained after the water was evaporated from a water-in-oil emulsion of a specific composition. That composition was 1-20 weight percent urea dissolved in 30 ml of aqueous ammonia at pH 12, with a very small amount of amphiphilic carbonaceous material (1.8 g) dissolved therein as well. This was added to 500 ml of olive oil and stirred at 90 °C until the water evaporated, leaving gel beads. The resulting beads were found to be hollow, with SEM observations revealing diameters ranging from 2-15  $\mu\text{m}$  and wall thicknesses averaging about 1  $\mu\text{m}$ . It was hypothesized that the evolution of  $\text{CO}_2$  gas from the decomposition of the urea at 80 °C in the ammonia water formed within the microballoons. Further additions of polyvinyl alcohol (PVA), polyvinyl pyrrolidone (PVP), or polyethylene glycol (PEG) were observed to alter the MB surfaces. PVA additions resulted in dimples or pores in the surfaces, whereas PVP and PEG additions produced smooth MBs. The resulting

carbonaceous gel PMBs were then heat treated at 500, 750, or 1000 °C to convert the structure to carbon, thus producing CMBs of a size that so far has heretofore been difficult to achieve [55, 56].

#### *2.4. Compression of filled microballoons*

While much of the specifics of the mechanical testing of MBs will be presented in a subsequent chapter, there is a test technique for liquid-filled MBs, e.g., microcapsules, that will be presented here. Liu et al. [57-59] tested filled polyurethane MBs in compression. Their experimental setup consisted of a motorized stage mounted on an inverted optical microscope. A force transducer was used to measure the force applied to a microcapsule as the motorized stage was slowly moved upward, crushing the filled MB between the upper platen attached to the transducer and the glass slide atop which the microcapsule was placed. The entire compression test was recorded on digital video through the microscope lens beneath the microcapsule, allowing measurement of lateral extension as well as estimation of the contact area between the microcapsule and the lower platen. Liu et al. [57-59] used a theoretical model for a filled non-linear elastic membrane to calculate the theoretical burst strength, Young's modulus, and pressure difference across the microcapsule wall. However, given that they only investigated filled polyurethane MBs, little further comparison with the current research is warranted [57, 59, 60].

### 3. Thermosetting Binders

The matrix material in three-phase syntactic foams, which contains significant intentional void content, is often termed the binder. This terminology may have been a deliberate attempt to convey the low volume fraction and potential discontinuity of the polymer in the foam and definitely was used to emphasize that the polymer bound the MBs in place in the system [6, 40-45]. For convenience of molding of polymeric syntactic foams, thermosetting polymers are often chosen as binders in both two- and three-phase syntactics [2, 3, 6, 9-21, 23, 25-34, 36-38, 40-45, 61-65].

The foam used in this investigation possessed a very different polymer binder, a bismaleamid known as APO-BMI [47, 48]. APO-BMI was the replacement for the polyimide binder Kerimid 601, which contained the carcinogenic curing agent 4, 4'-Methylenedianiline (MDA) and was used previously in carbon syntactic foams. APO-BMI is produced exclusively by Honeywell FM&T (Kansas City, MO) for Los Alamos National Laboratory to use in this application. The material is a single-part thermosetting material that undergoes both melting at approximately 130 °C and a curing reaction at about 210 °C. During curing, the polymer is cross-linking by homopolymerization [48]. Unfortunately, APO-BMI is very brittle and solid samples of any size were impossible to obtain. However, some characterization of the very limited samples available was performed and the results of differential scanning calorimetry (DSC) and nanoindentation will be delineated in a later chapter.

#### 4. Organization of Work

The following seven journal articles, reprinted with permission for the two already published, provide a succinct overview of the mechanical property and morphology characterization of the CMBs used in a three-phase syntactic foam composite. These articles, whose inter-relationship will be detailed below, contain the bulk of the research and testing data performed at UAB on these CMBs, and represent testing of four different lots of CMBs (ASTM B 527 tap density). Additionally, one of the articles describes characterization of an APO-BMI coated tap density of CMBs. While the main focus of this research has been characterization of the CMBs themselves, some testing of the APO-BMI binder phase of this syntactic foam and of the complete syntactic foam has also been performed; each of these are the subject of one of the articles included below.

The first article, "Structure and Mechanical Properties of Micro and Macro Balloon: An Overview of Test Techniques," [66] is intended to provide a comprehensive review of the techniques that have been used to evaluate the mechanical properties and morphology of MBs. While a considerable portion of this article is literature review, there is also some original content. Test methods described include: pycnometry, tap density, bulk isostatic compression, single MB isostatic compression, individual MB uniaxial compression, single MB uniaxial tension, tensile burst testing, nanoindentation, optical microscopy, SEM, interferometry, and laser confocal microscopy. Throughout the presentation of these techniques, explanation is given as to how they may be used to determine parameters including wall thickness, Young's modulus, strength, strain, etc. from MBs of polymer, metallic, or ceramic composition [66].

The second article, "Characterization of Carbon Microballoon Syntactic Foams," delineates the impulse excitation and quantitative microscopy work that has been performed on the foam. Data on the variations in Young's modulus as a function of the tap density of the constituent CMBs and a function of bulk density are presented. Additionally, measured trends in the volume fractions of carbon, APO-BMI, multi-compartmented CMBs, and broken CMBs in the foam are presented, and explanations for the observed trends were postulated.

The third article, "Characterization of the Binder Phase in a Three-Phase Carbon Microballoon Syntactic Foam," details the characterization of the thermal properties and Young's modulus of the bismaleamid binder that is used in these carbon microballoon syntactic foams. Since limited samples of this material were available in bulk, the only mechanical property characterization presented is nanoindentation, of neat APO-BMI and of APO-BMI *in situ* in the syntactic foam. Supplementing this data is differential scanning calorimetry of the APO-BMI, neat and in the foam. Average Young's modulus was reported, as were the melting and curing temperatures for the APO-BMI. Trends in cure behavior depending on the presence of CMBs were noted, and explanations for them were postulated.

The fourth article, "Microstructure and Compressive Properties of Carbon Microballoons," [67] describes the characterization of three lots (ASTM B 527 tap density) of CMBs. The research described in the paper involves the determination of wall thickness, diameter, shape, and compressive properties of CMBs. The compressive properties include stiffness, failure strain, and work-of-fracture, with discussion of the

relevant trends between tap densities. These trends were linked back to microstructural parameters for each tap density, and the differences in each tap density explained [67].

The fifth article, “Uniaxial Compressive Properties of Bismaleamid-Coated Carbon Microballoons,” investigates the uniaxial compressive behavior of a fourth tap density of CMBs, and compared their behavior to the other three. Once this tap density has been characterized and determined to follow the prior trends, it serves as a control for the characterization of the uniaxial compressive properties of CMBs which are coated in cured APO-BMI. The trends in the behavior of the coated CMBs are noted, and compared to the uncoated samples. Additionally, conclusions are drawn regarding the effect of a thin APO-BMI coating on the behavior of CMBs in the foam.

The final two articles, “Finite Element Modeling of the Uniaxial Compressive Behavior of Carbon Microballoons I: Idealized Model” and “Finite Element Modeling of the Uniaxial Compressive Behavior of Carbon Microballoons II: Flawed Microstructures,” address the issue of understanding the stress states and their distributions in the CMBs previously experimentally studied. The first paper focuses specifically on the compression of CMBs which are assumed to be defect-free spherical shells, whereas the second paper is concerned with the behavior of microstructures containing the main flaws observed in CMBs. In both articles, finite element modeling (FEM), using commercially available ANSYS 8.0, was performed on two-dimensional (2D) and three-dimensional (3D) models of CMBs. These models are of three varieties: a perfect shell, a flawed shell in which the internal hollow is not concentric with the external surface, and a flawed shell with a through-thickness hole. These models were used to predict the stress states in CMBs possessing the average properties of the

previous three tap densities, the effect of varying wall thickness-radius ratio on the failure mode of the CMBs, and the relative detriment of basic flaws to the structural integrity of the CMBs. The results have provided insight into the explanations for the experimental trends in the CMB behavior, and Weibull statistics were combined with the FEM results to prove the existence of the failure modes predicted in these materials.

Together, these seven articles represent a comprehensive study of the background, morphology, compressive properties, and modeling of individual CMBs, coated CMBs, the APO-BMI binder, and the complete foam. In combination with the foam characterization work by Gladysz et al. [48], Chavez et al. [68], Shabde et al. [69] and McEachen [47], this provides a thorough study of a previously little-studied syntactic foam system.

STRUCTURE AND MECHANICAL PROPERTIES OF MICRO AND MACRO  
BALLOONS: AN OVERVIEW OF TEST TECHNIQUES

by

K.B. CARLISLE, K.K. CHAWLA, G.M. GLADYSZ, M. KOOPMAN

*Journal of Materials Science* 41 (2006) 3961.

Copyright

2006

by

Springer Science + Business Media, Inc.

Used by permission

Format adapted and errata corrected for dissertation

## Abstract

A recently developed technique for obtaining uniaxial compression properties of individual microballoons by using a nanoindentation instrument equipped with a flat-ended tip of cylindrical or square cross-section will be described. A variety of useful parameters can be extracted from load vs. displacement curves such as: failure load, strain to failure, fracture energy, and a pseudo-stiffness or spring constant of each microballoon tested. The technique allows for a comparison of compression properties between individual microballoons of varying size or morphology. Other techniques for compression of both individual and large numbers of microballoons simultaneously, will be compared to this new test procedure. Two novel tensile test techniques will be reviewed. Additionally, the use of complementary test methods—including quantitative microscopy, SEM, interferometry, and nanoindentation—for characterizing the structure and properties of microballoons will be discussed.

## 1. Introduction

Originally, microballoons and macroballoons (note that microballoons will henceforth be abbreviated MBs, whereas macroballoons will not be abbreviated) were viewed as fillers, i.e. they provided increased specific properties while simultaneously reducing the amount of polymer used. A perusal of the product information sheets from current MB manufacturers still shows the emphasis on this role. Increasingly, however, the reinforcement values of microballoons are also being realized. MBs are no longer relegated to the role of fillers but have become a second phase in polymer composites that can increase the material's properties significantly, especially compressive and impact strengths. Thus, a polymer part containing MBs can more appropriately be called a composite. Other uses of MBs are becoming more common as well. MBs can facilitate a sustained release of drugs contained in their interior in the pharmaceutical industry, provide a mechanism for storage and release of adhesive in Post-It® notes, and release perfumes and moisturizers when broken in household products like detergents and skin care creams [1]. All of these applications are aided from a design standpoint by knowledge of the structure and properties of the MBs.

What has led to the proliferation of MB uses? Mostly, it is continued advances in production techniques, combined with an expanding range of materials from which microballoons may be manufactured. The original patents for producing polymer microballoons (PMBs), like those shown in Fig. 1, or glass microballoons (GMBs), see Fig. 2, were merely the beginning of microballoon production. Techniques for producing MBs from other polymers, from the polyglycolic acid and polylactic acid used in drug encapsulation to hydrogels, have been developed. In producing such MBs, methods

besides disk atomization of polymeric solutions containing blowing agents are being replaced by ultrasonic atomization for better particle size distribution control or even by emulsion techniques, where the microballoons are formed completely without the aid of blowing agents. Template methods for production have been considered. Additional advances have led the original MB technology to new applications, such as the production or modification of glass microballoons for specialized applications and the polymeric microballoons that are being produced specifically for conversion via heat treatment to other materials, e.g., the carbon microballoons (CMBs) shown in Fig. 3 [2-4].

With this growth in the use of MBs and the technology associated with their production, so too must the ways of characterizing MBs grow. One of 3M's early patents for producing glass microballoons specifically refers to a test technique using isostatic compression for measuring the strength of MBs. This technique would later become ASTM D 3602, which is still used for testing glass microballoons today, although the standard has been discontinued for unknown reasons. Other techniques that were used during the developmental phase of microballoons are in similar states and are often the only tests routinely utilized to measure the mechanical characteristics of microballoons. However, many of today's applications differ greatly from those initial applications and thus require more thorough mechanical property and structural information of the microballoons. This, then, becomes the primary goal of this review. We will strive to present the older established methods of microballoon characterization, the newer small scale test techniques that have been recently developed, and revisit some novel tests that never gained wide usage in microballoon testing. The goal is to describe the type and

utility of the information obtained from each test technique, as well as to explore how a synergy of these methods may best provide an overall characterization of microballoons [5, 6].

## 2. Microscopic Examination of Microballoons

Scanning electron microscopy provides an invaluable tool for analyzing MB morphology. Provided that non-conducting samples are properly coated, almost any MB may be successfully imaged and useful data taken regarding its diameter as well as shape. Imaging of broken MBs can provide wall thickness data; wall thickness is often a property-controlling parameter of considerable interest. Figure 4 provides some examples of CMB wall thickness measurements taken on broken MB via SEM [7, 8]. For accurate measurement of wall thickness, the broken wall must be perpendicular to the microscope axis, or the angle of inclination known, for correction.

Optical microscopy techniques complement SEM measurements, giving a cross sectional interior view of mounted and polished MBs. Optical images can be useful in analyzing the MB's internal structure, wall thickness, and diameter. Conventional reflected light microscopy, as well as laser confocal microscopy and interference fringe microscopy, can be employed to advantage. Reflected light microscopy provides the traditional two dimensional images of a polished surface, as shown in Fig. 5. Care must be taken in the polishing procedure to minimize MB wall collapse and pull out during sample preparation. These images provide planar slices through MB mounted in epoxy, and thus any measurements made on the images do not necessarily reflect the actual diameter of the MB. Only those sections where an MB has been cut along its great circle

provide accurate measurements of MB wall thickness and diameter. Figure 6 illustrates this point. Fortunately, taking measurements of a 3-D structure on a 2-D image has been well studied in stereology, so solutions are readily available. In order to obtain correct values we must calculate, statistically, values of diameter and wall thickness from the mean lineal intercept data measured on each image. Specifically, to correct diameter ( $\phi$ ) and wall thickness ( $t$ ), the formulas are

$$\phi = \left(\frac{3}{2}\right)\lambda_{diameter} \quad (1)$$

$$\lambda_{wall} = \frac{4t(t^2 - 1.5t\phi + 0.75\phi^2)}{3(t^2 - t\phi + 0.5\phi^2)} \quad (2)$$

where  $\lambda$  is a measurement of thickness or diameter taken from mean lineal intercepts of the object of interest on the image [9, 10].

Both laser confocal and interference fringe analysis optical techniques yield similar 3D images of a polished microstructure. An optical microscope is used to image the sample surface, and computer software is used to construct a true 3D image of the sample surface. In the interferometry based system, the interference fringe patterns are analyzed and a 3D structure is calculated based on the analysis, whereas in the laser confocal microscope one uses monochromatic laser illumination and calculates where the in-focus portion of the image will be as the sample stage is moved vertically through focus. A movable aperture is used by the computer system to select only the focused area, and a stack of several focused two-dimensional (2D) images is formed such that the final 3D image is constructed by merging them along the vertical axis. Both systems yield similar results, as seen in Figs. 7 and 8. Both figures are 3D topologies of the sample shown in Fig. 5, and could easily be used to measure MB diameters and wall thicknesses.

A final optical microscopy technique, again interferometry-based, can be used to extract size measurements from MBs. This technique is applicable only to transparent MBs, such as GMBs and some PMBs. A dual-mirror interference microscope is used to image a single MB that is placed on one of the mirrors. The mirrors are then set so as to be slightly non-parallel. This yields an interference fringe pattern of light and dark concentric circles visible on the mirror. The focus is then adjusted until the darkest fringe is positioned on the MB, and the light source is switched from white to monochromatic. Figure 9 demonstrates the correct setup. Then, one simply counts the number of reference fringes between the darkest fringe outside the MB and the MB itself. The wall thickness ( $t$ ) of the MB can be calculated from the number of fringes ( $x$ ), the wavelength of the monochromatic light source ( $\lambda$ ), and the refractive index of the material ( $n'$ ) by using the following expression,

$$t = \frac{x\lambda}{4(n' - 1)} \quad (3)$$

This method has been shown to be accurate to within 0.05  $\mu\text{m}$  for measuring GMB wall thickness [10].

### 3. Density of Microballoons

Often, the density of MBs is of interest in determining other mechanical properties or can be used to distinguish between grades of MBs. Two separate methods are often used. One is pycnometry, where the volume occupied by a known mass of microballoons is measured by the volume of gas the MBs displace in a pressure chamber. Then, the balloon density is simply mass divided by volume. This method provides density measurements that are highly sensitive to MB quality, i.e., cracked or broken

MBs will be penetrated by the gas, resulting in higher density values than would be the case for undamaged MBs. The other method uses ASTM Standard B 527, originally designed to measure the average settled density of metal or ceramic powder, to measure the average settled density of a manufacturing lot of MBs. To perform this test,  $50 \pm 0.2$  g of MBs are placed in a 100 ml graduated cylinder, and then tapped 3000 times. The tap density of the MBs is their measured mass divided by the volume to which they settled after the vibration treatment. Note that this test depends on the settling behavior of the MBs, thus their surface characteristics, morphology, etc. will affect the settled density. A schematic of this test is shown in Fig. 10 [11].

#### 4. Compression Test Methods

##### *4.1 Nanocompression of individual microballoons*

Perhaps the most recent development in MB testing has been that of the compression of individual MBs. This was done by adapting a nanoindenter to function as a compression test frame, replacing the Berkovich tip with a flat-ended punch-like tip, and placing a flat, polished stub into the sample stage to function as a lower platen. The flat-ended punch is usually a sapphire cylinder with a flat tip of 90  $\mu\text{m}$  diameter, but, a smaller square cross-sectioned diamond tip of 25  $\mu\text{m}$  side length has proved successful. A schematic of this arrangement can be seen in Fig. 11. These compression tests give very accurate measures of failure load and indenter tip displacement.

Many different types of MBs have been tested via this technique, including CMBs, GMBs, partially cured phenolic MBs, and cured phenolic MBs. Figure 12 shows the different types of load-displacement behavior exhibited by these materials. As

expected, MBs of traditionally brittle materials have well defined, mostly linear curves, whereas phenolic MBs display more ductility. The partially cured phenolic does not even display a fracture point, but instead plastically deforms until totally flattened on the substrate. This ductile vs. brittle behavior is not the only characteristic observable in load-displacement data. Morphological differences in microballoons may also be inferred from the shape of the curves. Figure 13 provides an example, wherein we see three types of behavior from CMBs that can be related to their morphology. Single-walled microballoons possess one of the first two types of loading curves, whereas balloons with several internal compartments show the confusing behavior labeled nested in the figure. Figures 2, 3, and 6 provide visual proof of the existence of nested MBs in both glass and carbon. The flawed single-walled category of MB behavior was hypothesized to result from single walled microballoons that have holes or other imperfections in their walls.

Compression data provide several useful engineering parameters. Load ( $P_f$ ) and displacement ( $\delta_f$ ) at failure are obtained directly from most load-displacement curves, the slope of the loading segment provides a pseudo-stiffness ( $k$ ), and the work of fracture ( $W_f$ ), defined as the area under the loading portion (or portions, for nested MBs) of the curve. The diameter of the MB in the loading direction, or vertical diameter ( $\phi_v$ ), is merely the difference in the displacement at initial loading and that when the indenter impinges upon the substrate. The compressive failure strain ( $\epsilon_f$ ) is calculated as the quotient of the displacement at failure and the vertical diameter, thus:

$$\epsilon_f = \frac{\delta_f}{\phi_v} \quad (4)$$

These parameters provide a fairly wide range of property data, and average properties may of course be calculated for each type of MB. Additionally, trends between various

parameters have been observed. For glass microballoons, which appear to be the most uniform type of MB under microscopic inspection, the authors have observed the trends shown in Figs. 14 and 15, relating failure load of GMB and work of fracture to diameter. Other types of microballoons examined by this technique have not shown these correlations, but tend to possess other, weaker correlations, due to their more irregular natures [7, 8, 12].

#### *4.2 Microcompression of individual microballoons*

This test technique, from Bratt et al. [14], utilized a custom developed compression apparatus to perform uniaxial compression on glass microballoons. The aim was to characterize the compressive strength of GMBs, especially focusing on testing that would relate to the durability of the MBs during mixing into polymer matrix composites. The test apparatus consisted of a motorized  $x$ - $y$  stage, a stationary platen, and a conical flat-tipped rod to which an LVDT was attached. The MB was crushed between the platen and rod tip in essentially uniaxial compression, save for the affixing of the MB to the rod with epoxy. A force-time plot in compression was obtained for each MB, which was combined with a very precise measure of the wall thickness and diameter of each MB to yield stress-strain curves as explained below. These curves are generated based on an assumed failure at the equator of each MB due to tensile stress. With this assumption, the stress and strain may be extracted from a “flexure test” model, giving stress at the MB’s surface as

$$\sigma = \frac{F}{2\pi^2} \quad (5)$$

and strain as

$$\varepsilon = \frac{54et}{d^2} \quad (6)$$

In Equations 5 and 6,  $F$  is the applied uniaxial compressive force,  $d$  is the MB diameter, and  $t$  is the wall thickness. Once stress and strain are known, Young's modulus of the glass wall material was calculated from Hooke's Law. One overall trend was the clear dependence of failure load upon wall thickness, as seen in Fig. 16 [14]. Note that the trend line shown corresponds to an average failure strength ( $\sigma$ ) of 2.2 GPa, which compares favorably to the well-documented tensile strengths of glass fibers [13].

#### 4.3 Compression of individual macroballoons

Alumina hollow spheres of 1 – 5 mm diameters and 25 – 200  $\mu\text{m}$  wall thickness were tested in uniaxial compression using a traditional mechanical test frame [14]. Raw data for this test was the failure load ( $F_c$ ) of each hollow macroballoon. Unique to the Chung et al. [14] analysis is their definition of macroballoon strength ( $\sigma_s$ ) as the quotient of the failure load of the macroballoon and its projected area, thus

$$\sigma_s = \frac{F_c}{0.25 \pi d^2} \quad (7)$$

Equation 7 might appear to make an unprecedented use of the area of the macroballoons' great circle to normalize the raw loading data. This is not totally without justification, however. In the oil industry, small hollow particles were considered as proppants—small particles that will hold fissures in rock formations open—in petroleum wells. The strength of these proppants was successfully modeled in terms of a number of diametral contacts between close-packed hollow spheres that transfer a given force along each

contact. When only a single contact is considered, the strength reduces exactly to that employed by Chung et al. [14]. Failure behavior of these macroballoons was also predicted via finite element modeling, and both experimental and modeling results confirmed failure primarily along horizontal or vertical diameters. Relative density of the macroballoons, relative to solid  $\text{Al}_2\text{O}_3$ , was found to correlate with macroballoon strength, as Fig. 17 shows for both the experiments and the modeling [14]. It can be seen that model overestimated the slope of the curve substantially; this discrepancy was attributed to “imperfections such as non-uniform wall thickness, imperfect sphere geometry, flaws, small tails, etc. [14].”

#### *4.4 Bulk isostatic compression of microballoons*

This test method for microballoon characterization stems from the industrial need to characterize production lots of microballoons according to their compressive properties in a more efficient manner than individual compression provides. At one time, the procedure was an ASTM Standard, bearing designation D 3102-78, but it was withdrawn, for unknown reasons, in May 1984. Despite its withdrawal, it is still in use today as often the only test performed by MB manufacturers to characterize the compressive strength of their MBs. 3M, for example, performs a slightly modified form of this test (3M QCM 14.1.5) on all of their GMBs except the highest strength grade, which is tested via the original ASTM method.

The basic premise of the test is to expose a batch of MBs to a high isostatic pressure, during which some of the MBs will collapse. The percent of MBs that collapse (or survive) is measured, and the MBs are classified according to the isostatic pressure at

which a given volume percent of the MBs tested collapse (or survive). Both test methods place the MBs in a rubber container filled with either glycerin or isopropyl alcohol inside a pressure chamber. The ASTM test used oil as the working fluid, whereas the 3M test employs nitrogen gas. Once the MB sample is in the pressure chamber, it is pressurized to a predetermined pressure while recording both pressure and volume. This process is repeated to get a second set of pressure-volume data, and both data sets are plotted as pressure vs. volume curves. The initial pressurization is known as the collapse curve, and the second pressurization provides the system compression curve. Figure 18 provides an example of the two curves, which are used to determine the percentage of collapsed MBs in the test. Since air comparison pycnometry and a scale were used to determine the volume and mass of both the MBs and their rubber container prior to isostatic pressurization, the density of the MB wall material ( $\rho$ ) can be used to find the volume of wall material ( $V_m$ ) using the MB mass ( $M$ ):

$$V_m = \frac{M}{\rho} \quad (8)$$

Next, the original volume ( $V_v$ ) of the MB's interior void space is found by subtracting the volume of the wall material from the volume occupied by the MBs ( $V_{ap}$ ), which is determined via the pycnometer.

$$V_v = V_{ap} - V_m \quad (9)$$

In Fig. 18,  $V_t$  refers to the total volume collapse, and is the difference in the collapse and compression curve values at zero pressure. To calculate the fraction of collapsed MBs at a certain pressure level, the void volume collapsed at that pressure ( $V_p$ ) is found as

$$V_p = V_t - (V_{compression}(P) - V_{Collapse}(P)) \quad (10)$$

where  $V_{Compression}(P)$  and  $V_{Collapse}(P)$  are the volume values of the compression and collapse curves at the pressure of interest. Then, the percent volume collapse ( $V_{Collapse}$ ) is found as

$$V_{collapse} = 100 \left( \frac{V_p}{V_v} \right) \quad (11)$$

According to the ASTM standard, this percent void collapse was the only reportable parameter from isostatic testing; however, since the demise of the standard, the percent surviving MBs is often reported instead [6].

#### 4.5 Isostatic compression of individual microballoons

Another variation of the isostatic pressure testing for MBs is to test each MB individually. This is not a variation of the ASTM test, in that it places a single MB into a special holder, which is located inside a pressure chamber with a quartz window. A stereomicroscope is used to image the MB in the chamber as pressure is applied. When visual observation indicates that the MB has collapsed, the chamber pressure is recorded and testing ceases. Bratt et al. [13] used the equations for the accepted failure mechanism, i.e., shell wall buckling, for a spherical pressure vessel subjected to external isostatic pressure to predict a failure stress ( $\sigma_{Failure}$ ) for MBs tested in this fashion as

$$\sigma_{Failure} = \frac{2E}{\left( \frac{\phi}{t} \right) \sqrt{3(1-\nu^2)}} \quad (12)$$

where  $E$  is the Young's Modulus and  $\nu$  the Poisson's ratio of the MB wall material.

Figure 19 provides the results of this test for several GMBs, where the trend line was

calculated using a Young's modulus of 56.5 GPa and a Poisson's ratio of 0.21. Note the agreement between the calculated curve and the experimental data points [13].

## 5. Tensile Test Methods

### *5.1 Mechanical Tensile Testing*

Surprisingly, MBs have been successfully tested in tension, although the test doubtlessly was not purely tensile loading. The test technique, developed and employed solely at Los Alamos National Labs in the late 1970s, involves bonding two small brass rods to opposite ends of a GMB's diameter. Care is taken during bonding to ensure that a small region between the rods was left free of epoxy, providing the gage length. These rods provided the grip regions for the ensuing tensile pulling of the MB in a loading frame designed specially for the test. The loading apparatus consisted of a dynamometer (mounted on a xyz translation table), from which load at failure was recorded. This test method appears to have been the only one of its kind, and was only used on a few specific batches of KMS and 3M microballoons [15].

### *5.2 Tensile burst testing*

This method was also conceived and executed solely at Los Alamos National Labs during the late 1970s for quality verification of KMS and 3M GMBs. It is performed by sealing a single GMB inside a quartz tube and heating to 350 °C while pressurizing the tube with helium. The critical step here is the pressurization rate, which must be carefully increased to avoid bursting of the MB by external pressure, allow sufficient time for the helium to diffuse through the MB walls, and allow pressure

equalization between the interior and exterior of the MB. According to Milewski and Marsters [15], for a 1  $\mu\text{m}$  wall thickness GMB of 500  $\mu\text{m}$  diameter, a final pressure of 2.07 MPa can be reached at 30.23 MPa/min, and must be held for 10 minutes to achieve equilibrium conditions. Then, the temperature is decreased to room temperature, and the pressure in the quartz tube is decreased until the MB bursts due to internal pressure. The MB is observed throughout the experiment via a stereomicroscope, and upon failure, the pressure difference supported by the MB walls is recorded. The pressure differential can be used to calculate the maximum tensile stress in the MBs wall according to the relationship

$$\sigma = \frac{\Delta P \phi}{4t} \quad (13)$$

Equation 13 is in terms of the tensile stress ( $\sigma$ ), the pressure differential at failure ( $\Delta P$ ), the MB's diameter ( $\phi$ ), and the wall thickness ( $t$ ) of the MB. The results of this test were compared to the uniaxial tensile testing technique and were observed to yield similar but lower values. These lower values were expected, due to the greater probability of stressing a critical flaw when subjecting the entire MB to loading, rather than just a particular gage length [15].

## 6. Nanoindentation

Nanoindentation has become a routine method for determining the modulus and hardness of a material or of a phase therein, but, until recently, had not been applied to MBs. The method for indenting MBs successfully involved a single key step—the mounting and polishing of MBs in epoxy resin. Figure 5 provides an example of such a cross-section. Several samples such as this were indented in an MTS Nanoindenter XP II,

and the continuous stiffness measurement technique was used to determine the hardness and Young's Modulus from indents located in the thick regions of the carbon walls. Data from these tests must only be taken from relatively shallow indentation depths, as the wall beneath the surface curves, and therefore limits the volume of material available for indentation. The necessity of 500 nm or less indentation depths placed instrument calibration and tip sharpness as critical parameters that were carefully checked before each test batch. The white arrow in Fig. 20 shows the location of a successful indentation on a 0.143 g/cm<sup>3</sup> tap density CMB, and Fig. 21 provides the corresponding Young's modulus vs. displacement into surface curve for this point. Overall, this technique has provided the only measure of Young's Modulus for these CMBs (average was 12.76 GPa), and could be adapted to any type of MB that could be mounted in epoxy and polished.

## 7. Synergy of test techniques

Obviously, thorough characterization of the morphology and properties of microballoons requires a combination of the above techniques to obtain structure - property relationships. Information on morphology requires some sort of microscopic examination, but there are advantages and disadvantages to most methods. If the MBs to be examined are transparent, then the interference technique described by Weinstein [10] will yield the best measure of wall thickness and diameter; however, for opaque MBs, the best method depends on what type of information is needed. SEM is a direct measurement method, but suffers if large amounts of data must be gathered, i.e., a wide variation in wall thicknesses exists in the study population or a small confidence interval

is desired. Conventional optical microscopy coupled with statistically valid stereological formulas is best suited to analyzing large amounts of data, but then calculation accuracy in statistical correction becomes an issue. The interference fringe analysis and laser confocal techniques both would seem to alleviate this difficulty with optical imaging, since direct measurements of diameter and thickness are possible.

For evaluation of MB density, both pycnometry and tap density techniques can be used, although they each have limitations to their probative value. The gas pycnometer is sensitive to particle density and to the large volume change that occurs when MBs are fractured or broken. It is not at all sensitive to surface condition and particle geometry. Tap density is a measurement that takes into account the particle density as well as settling properties (particle geometry, friction, surface condition, etc.) and is important especially in three-phase syntactic foams [17]. However, tap density measurement would not differentiate, all else being equal, a sample containing 0% cracked MB and another that has 10% cracked MBs, assuming the cracked particles retain their spherical shape. Thus, each method yields different but complementary information regarding density.

Characterization of MB mechanical properties also requires a combination of testing techniques, depending upon what mechanical property is relevant. To predict the MBs load-bearing ability in conventional syntactic foams, isostatic pressure testing provides a reasonable measure of the balloons' survivability under multi-point loading, as is also true with their ability to be injection molded. Of the two isostatic test methods, the bulk test is clearly faster and more applicable to industry. Uniaxial compression data from microballoons is thought to relate more to the MBs durability in handling and mixing with polymers for syntactic foam construction. Of the methods for MB

compression, none would scale well for commercial use, although the nanoindenter compression technique has been used for initial product evaluation and comparison between small populations with different processing parameters. The additional benefit here is the growing availability and reliability of nanoindentation equipment; not only can compressive properties be obtained, but the same instrument can also provide Young's modulus of MBs. Of course, these techniques need simultaneous application of microscopic examination to extract both wall thickness and diameter from the MBs to realize maximum utility. In the realm of tensile testing of MBs, neither method has seen significant use outside a laboratory setting. While the burst test could provide useful data to complement isostatic crushing of single MBs, the uniaxial tensile procedure does not necessarily test the MB in pure tension. So, the choice of method for mechanical property assessment should be based upon the anticipated stress states likely to be encountered in specific applications.

Further, evaluation of actual and potential reactions of MB, and foams in which they are incorporated, can be aided by 2D and 3D modeling. Commercially available software packages, as well as application specific programs, require input values from many of the techniques described. Both idealized and actual microstructures and MB morphologies can be hypothesized and evaluated for given applications.

## 8. Conclusions

By combining electron and optical microscopic techniques with novel mechanical testing, microballoons may be characterized in terms of both their morphology and mechanical properties. Microballoon wall thickness, diameter, and sphericity are all

determinable by microscopy, and these results aid in the analysis of the compressive loading data from various test procedures. Isostatic compression of both individual and bulk microballoon samples can be used to determine failure strengths, uniaxial compression tests are available for failure load determination, and some tensile testing has been performed. Additionally, nanoindentation of microballoon wall materials has been proven to be a method for obtaining hardness and modulus. Together, all of these techniques can provide both manufacturers and customers a better understanding of microballoons' performance.

## 9. Acknowledgements

Partial support for this work was provided by Los Alamos National Laboratory/DOE subcontract #44277-SOL—02 4X. K.B. Carlisle is grateful to the Department of Defense for a National Defense Science and Engineering Graduate Fellowship.

## 10. References

1. H.L. PRICE and J.B. NELSON, *J. Composite Materials* **10** (1976) 314.
2. F. VEATCH and R.W. BURBANS, Process of Producing Hollow Particles and Resulting Product. (The Standard Oil Company, United States, 1953). US Patent 2,797,201.
3. K. ESUMI, S. ESHIMA, Y. MURAKAMI, H. HONDA, and H. ODA, *Colloids and Surfaces A: Physicochemical and Engineering Aspects* **108** (1996) 113.
4. A. BOURLINOS, N. BOUKOS, and D. PETRIDIS, *Adv. Mater* **14** (2001) 21.
5. W.R. BECK and D.L. O'BRIEN, Glass Bubbles Prepared by Reheating Solid Glass Particles. (Minnesota Mining and Manufacture Co., United States, 1963). US Patent 3365315.

6. ASTM D 3102-78: Standard Practice for the Determination of Isostatic Collapse Strength of Hollow Glass Microspheres, in "Annual Book of ASTM Standards" (American Society for Testing and Materials, 1984).
7. G. GOUADEC, K. CARLISLE, K.K. CHAWLA, M.C. KOOPMAN, G.M. GLADYSZ, and M. LEWIS, Nano-compression of carbon micro-balloons with a flat-ended cylindrical indenter, in Proceedings of Indentation Techniques in Ceramic Materials Characterization, Apr 27-30 2004, Nashville, TN., United States (American Ceramic Society, 2004). pp. 143-152.
8. K. CARLISLE, K.K. CHAWLA, G. GOUADEC, M. KOOPMAN, and G.M. GLADYSZ, Nanocompressive properties of carbon microballoons and mechanical properties of carbon based syntactic foam composites, in Proceedings of ICCM-14, San Diego, CA, July 2003 (Society of Manufacturing Engineers, 2003).
9. E.E. UNDERWOOD, Surface Area and Length in Volume, in "Quantitative Microscopy", R.T. Dehoff and F.N. Rhines, eds. (McGraw-Hill, New York, 1968) pp. 96-97.
10. B.W. WEINSTEIN, *Journal of Applied Physics* **46** (1975) 5305.
11. ASTM B 527: Standard Test Method for Determination of Tap Density of Metallic Powders and Compounds, in "Annual Book of ASTM Standards" (American Society for Testing and Materials, 2000).
12. M. KOOPMAN, G. GOUADEC, K. CARLISLE, K.K. CHAWLA, and G. GLADYSZ, *Scripta Materialia* **50** (2004) 593.
13. P.W. BRATT, J.P. CUNNION, and B.D. SPIVAK, Mechanical Testing of Glass Hollow Microspheres, in "Advances in Materials Characterization", D.R. Rossington, R.A. Condrate, and R.L. Snyder, eds. (Plenum Press, New York, 1983) pp. 441-447.
14. J.H. CHUNG, JOE K. COCHRAN, AND KON J. LEE, Compressive Mechanical Behavior of Hollow Ceramic Spheres, in Proceedings of Mat. Res. Soc. Symp. (Materials Research Society, 1995). pp. 179-186.
15. J.V. MILEWSKI and R.G. MARSTERS, *J. Vac. Sci. Technology* **18** (1981) 1279.

## 11. Figures

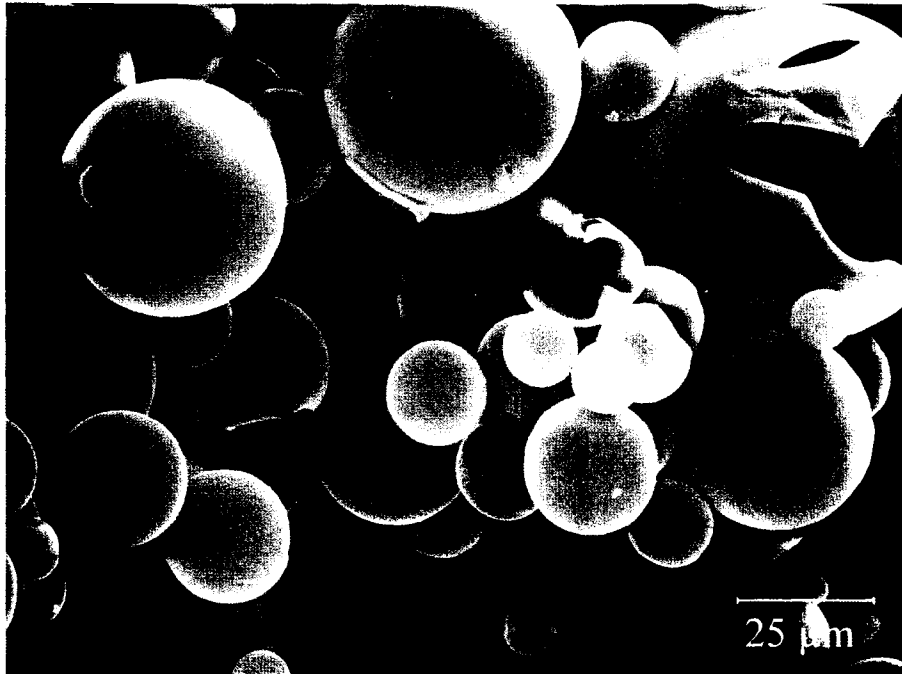


*Figure 1* Phenolic microballoons, showing size range and many broken balloons. SEM

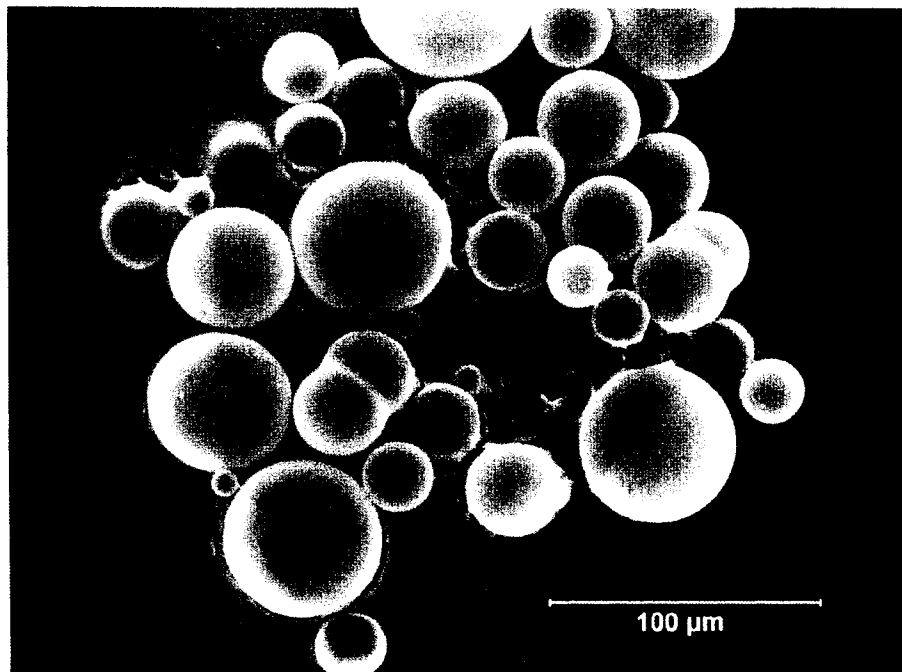


*Figure 2* GMBs (3M A16/500). Note the size range and regular morphology. SEM

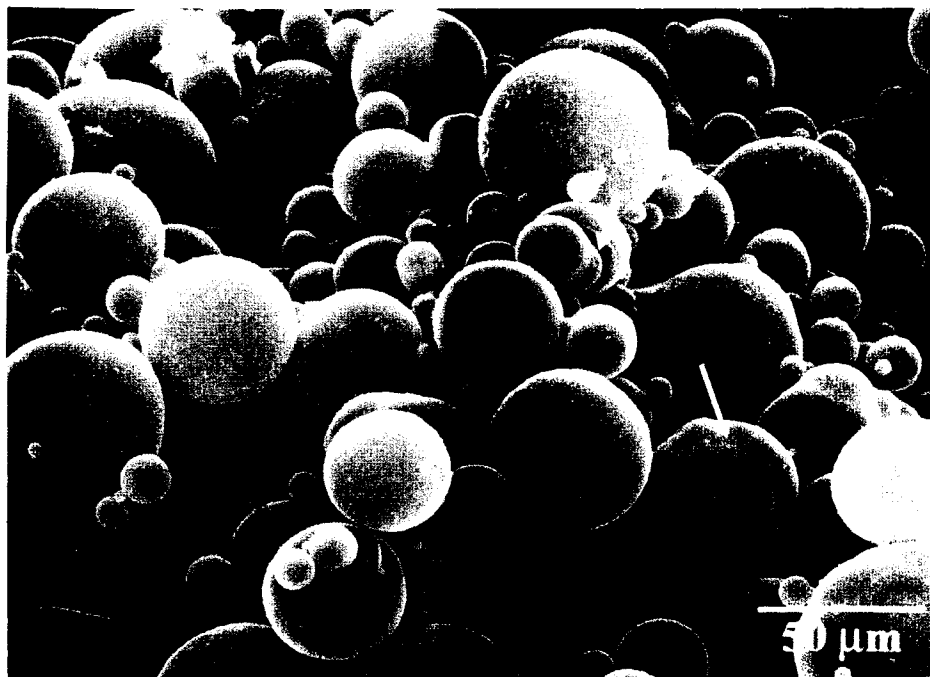


*Figure 3* 0.177 g/cm<sup>3</sup> tap density CMBs, showing general spherical morphology. Defects like multi-compartmented and broken MBs are also visible (arrows) SEM.

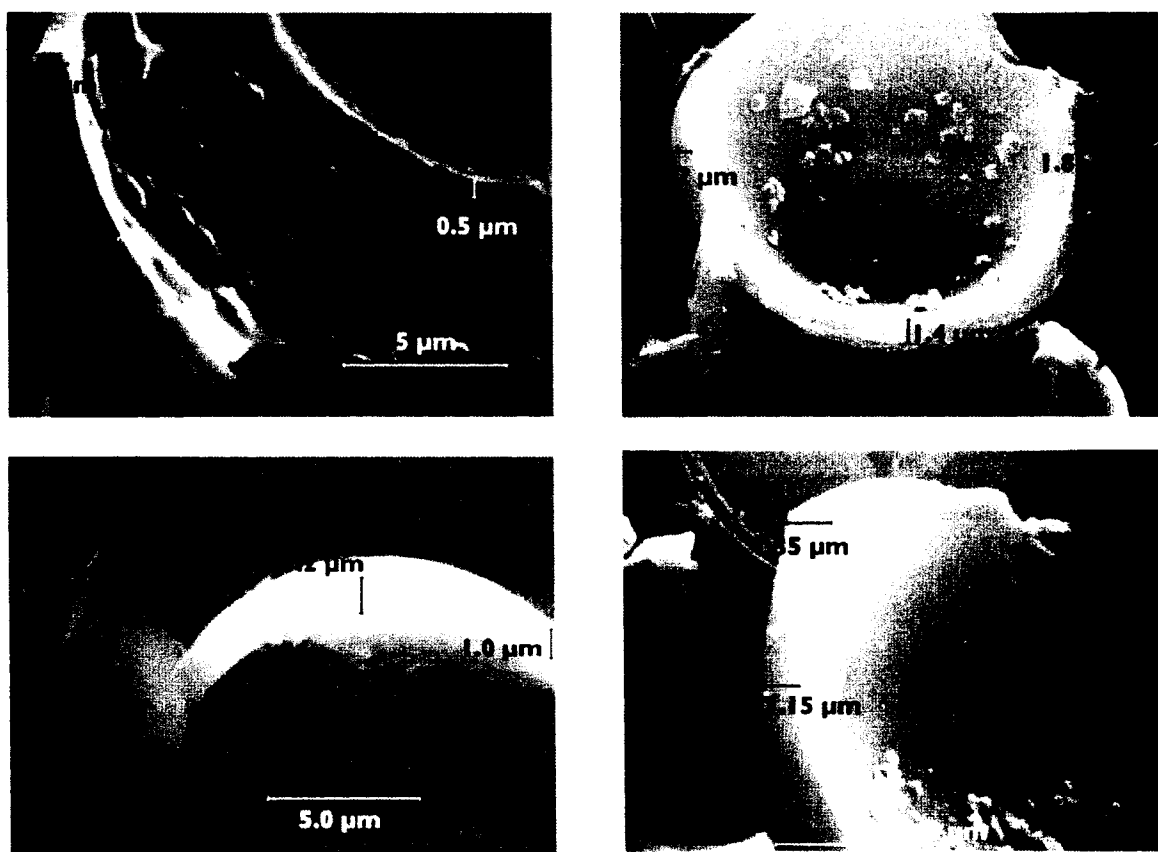


*Figure 4* Wall thickness measurement of CMB fragments. Range of observed thickness in the figure is 0.5 to 2.4  $\mu\text{m}$ . SEM. After refs. [7, 8].



*Figure 5* Polished cross-section of CMBs mounted in epoxy. This representative image of those used for quantitative microscopy also shows internal structure and variation in MB wall thickness.

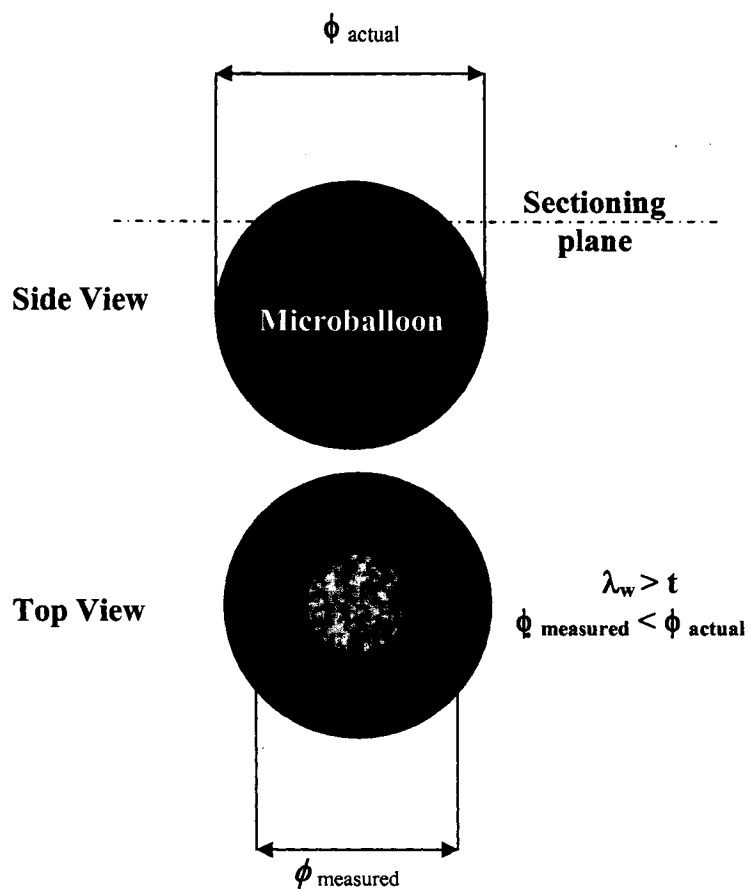


*Figure 6* Schematic of MB sectioned above its great circle. Light grey region represents the sectioned surface, with diameter and thickness on the sectioning plane inaccurate as shown.

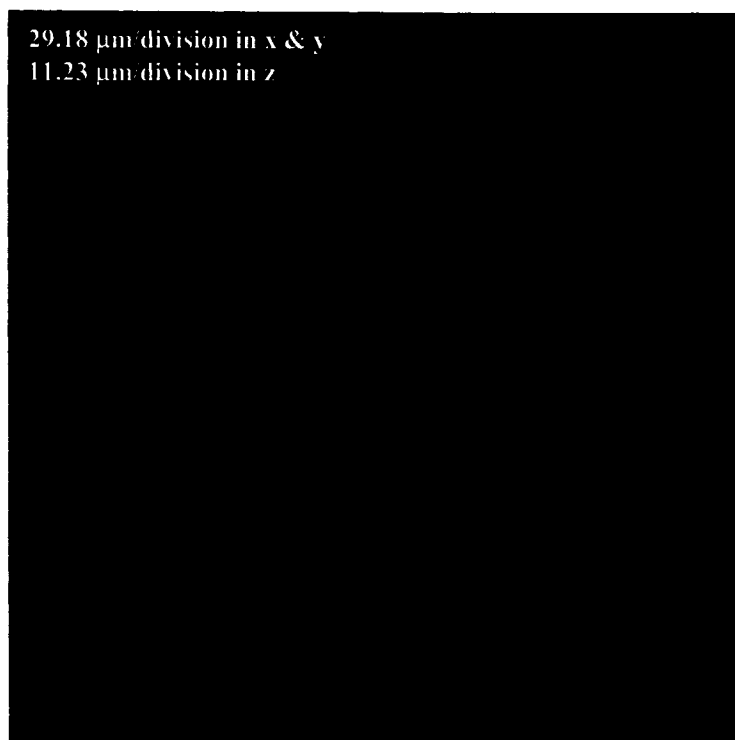


*Figure 7* Optical interferometry image of  $0.143 \text{ g/cm}^3$  tap density CMBs mounted in epoxy, allows direct measurement of wall thickness.

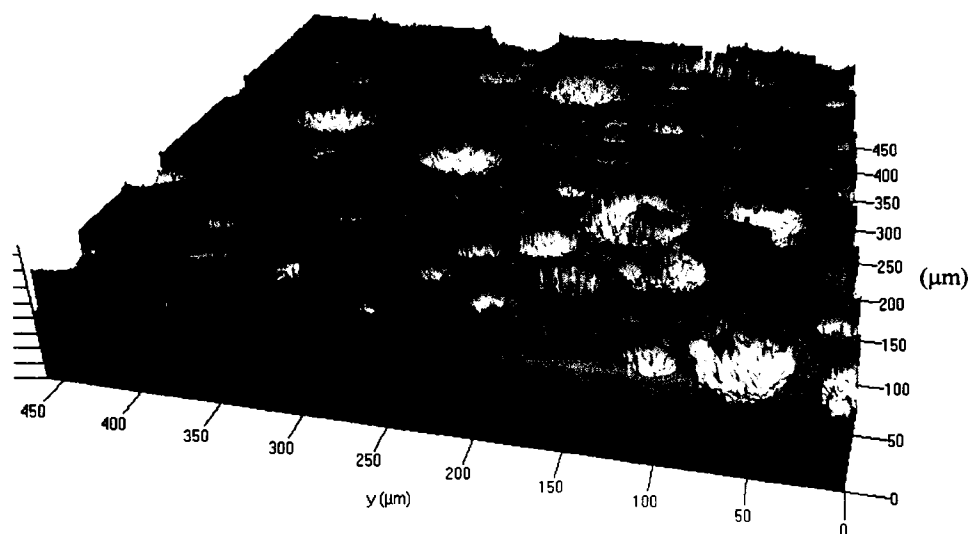


*Figure 8* Laser confocal microscope image of  $0.143 \text{ g/cm}^3$  tap density CMBs mounted in epoxy. Wall thicknesses standing proud with respect to the mount resin.

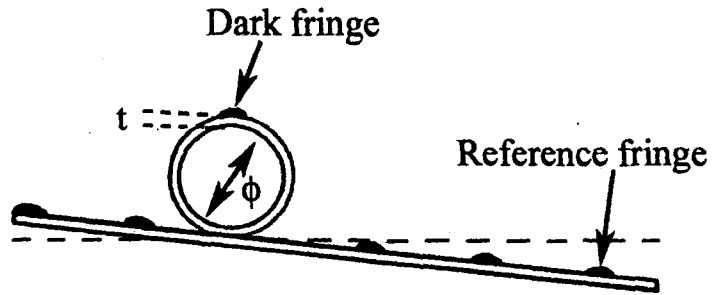


Figure 9 Schematic of interference light microscope configuration use to measure wall thickness of transparent MBs. After ref. [10].

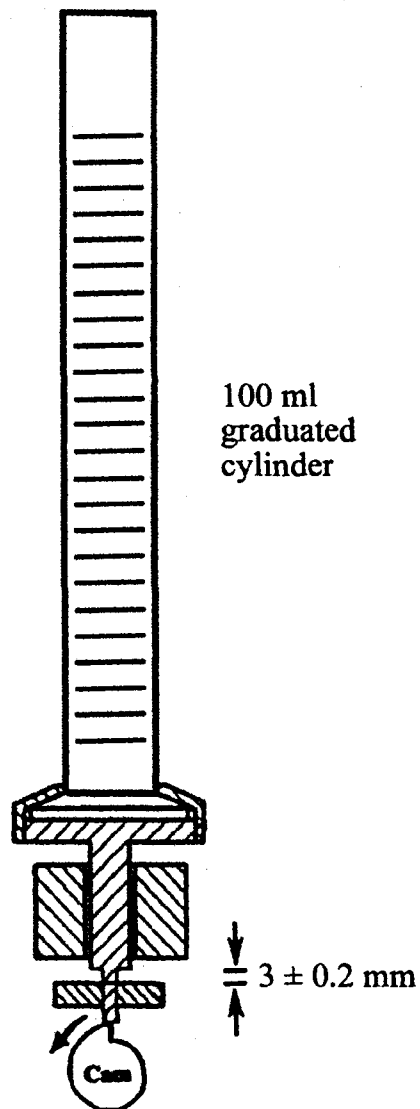


Figure 10 Schematic of tap density test apparatus for ASTM B 527. After ref. [11].

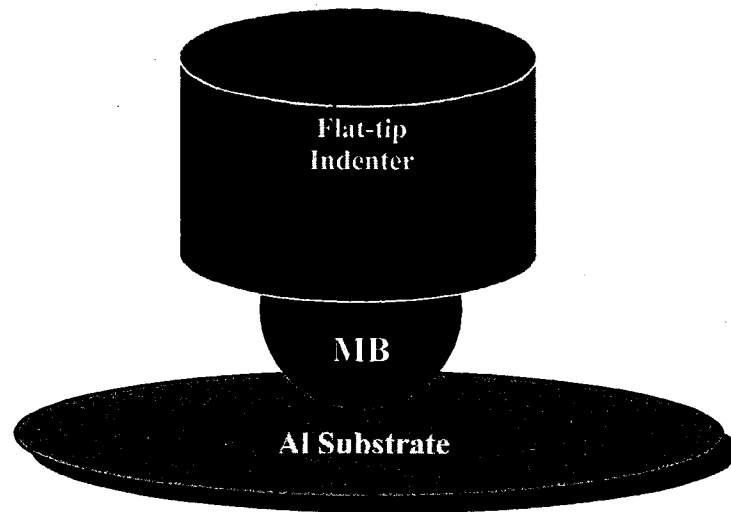


Figure 11 Schematic of nanoindenter modified for use in compression testing of MBs. After refs. [7, 8].

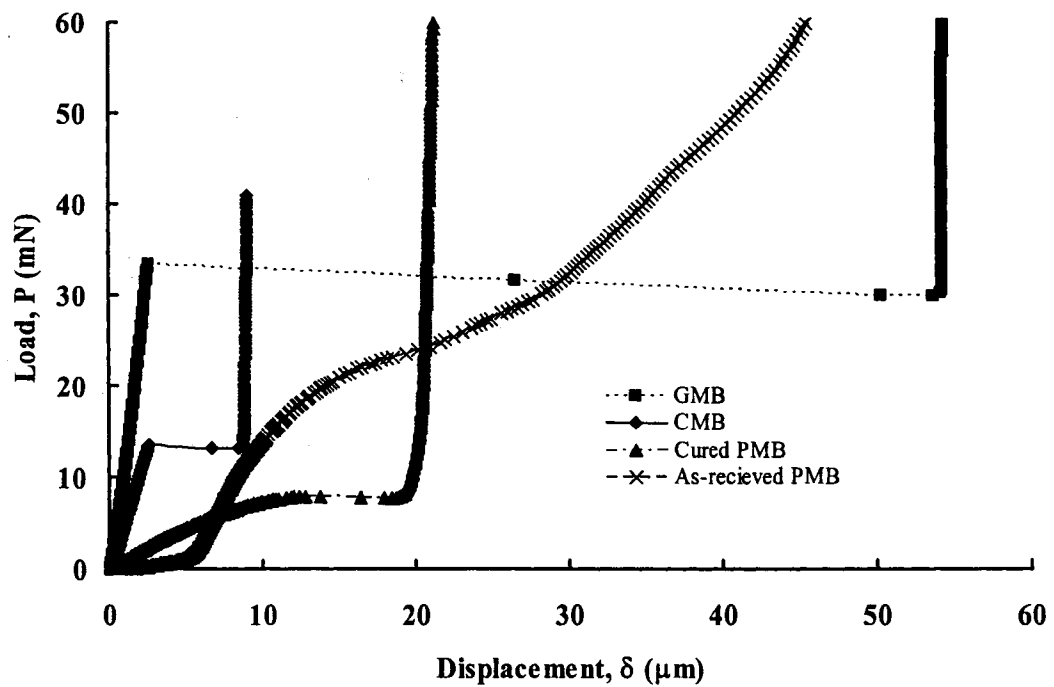


Figure 12 Compression curves from MBs composed of different materials. Note the brittle vs. ductile behavior.

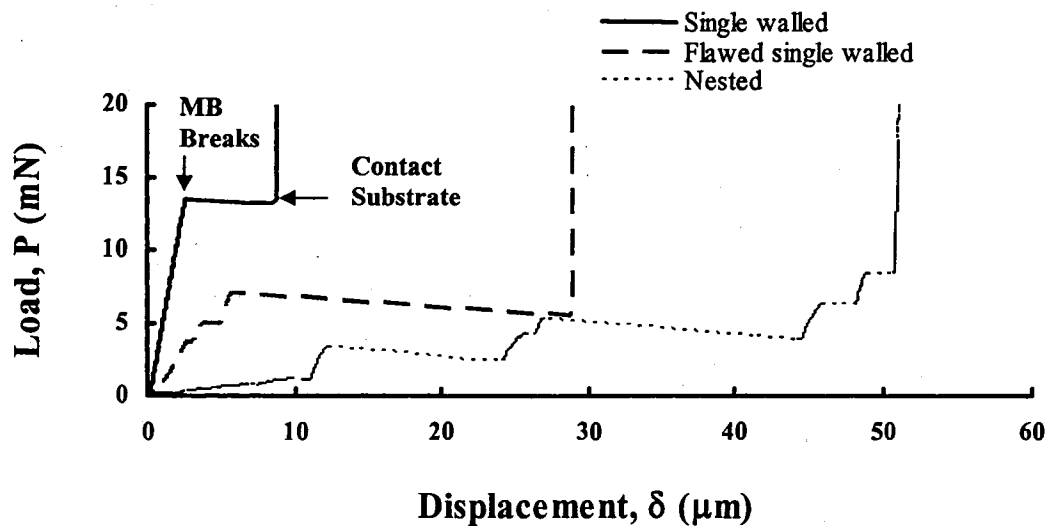


Figure 13 Possible types of compression behavior for brittle CMBs. After refs. [7, 8].

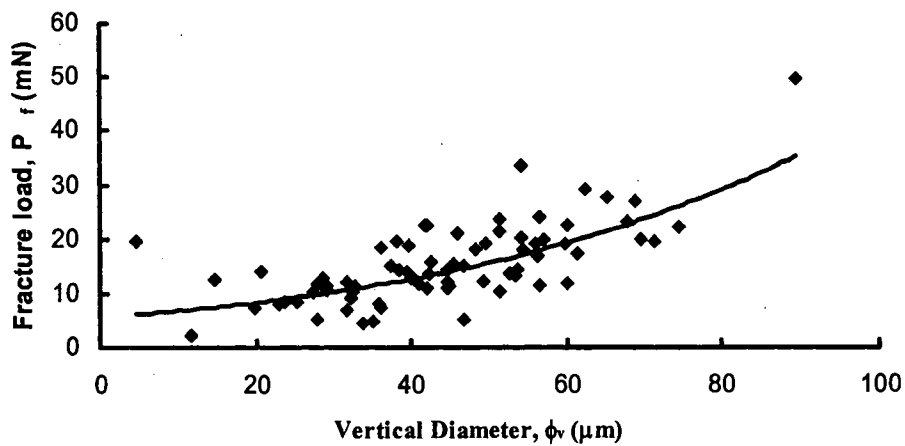


Figure 14 Direct correlation of failure load to MB diameter for GMBs (3M A16/500). After ref. [12].

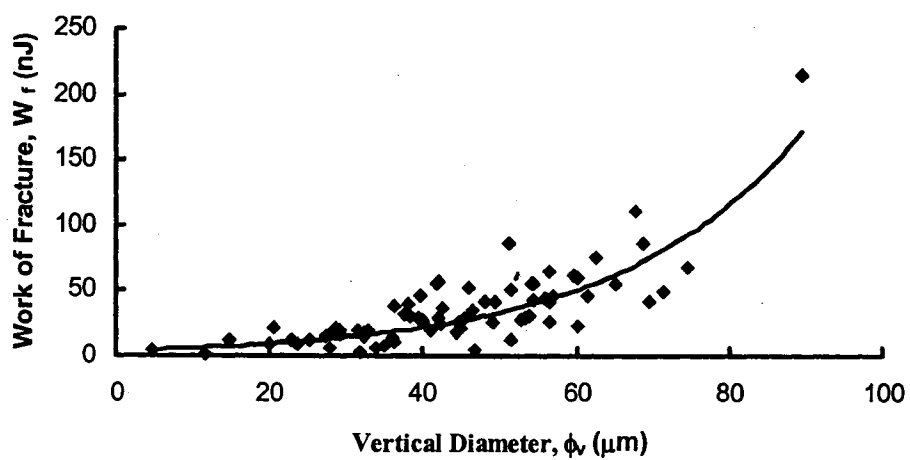


Figure 15 Work of fracture correlated favorably with MB diameter for GMBs (3M A16/500). After ref. [12].

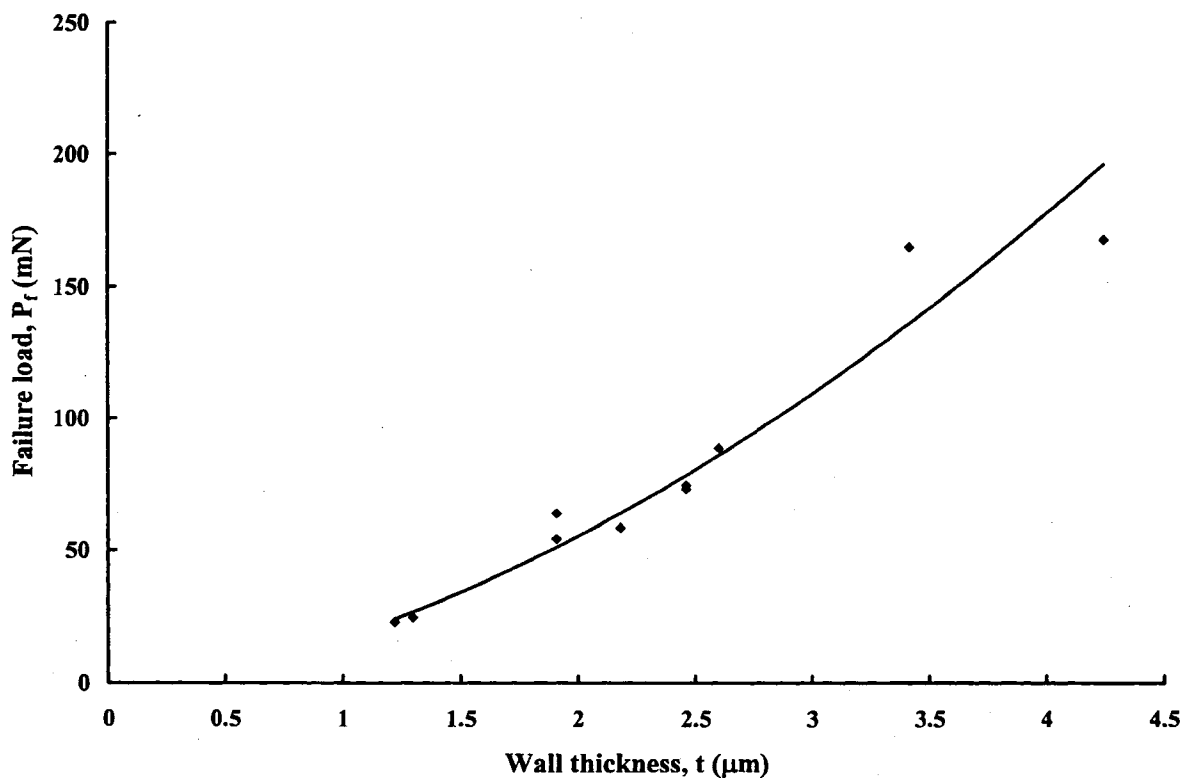


Figure 16 Failure load vs. measured wall thickness for GMBs, showing  $P_f \propto t^2$ . After ref. [13].

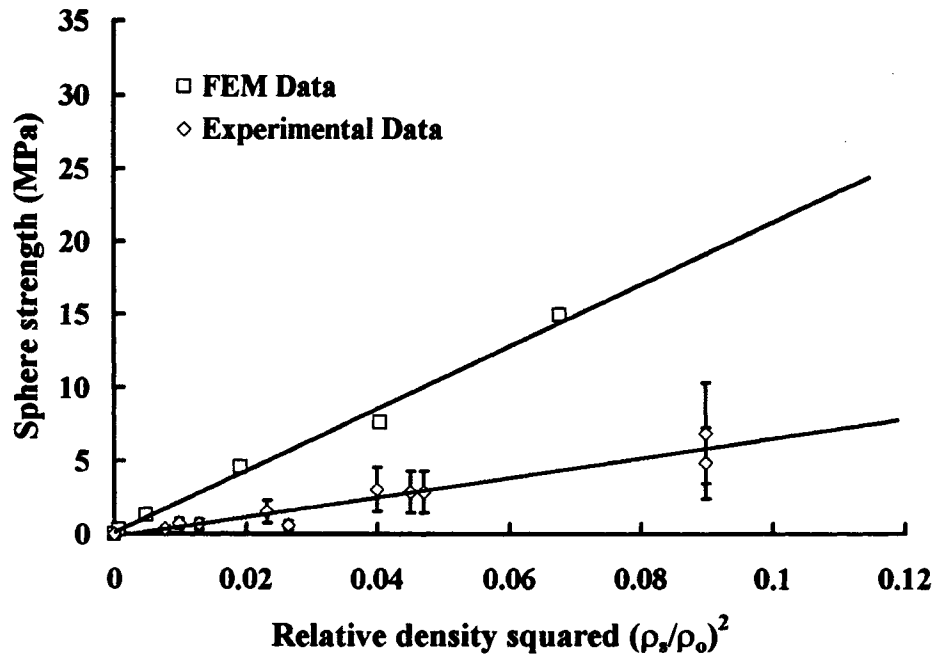


Figure 17 Strength vs. relative density squared for  $\text{Al}_2\text{O}_3$  macroballoons. Linear relationships for both predicted and theoretical curves. After ref. [14].

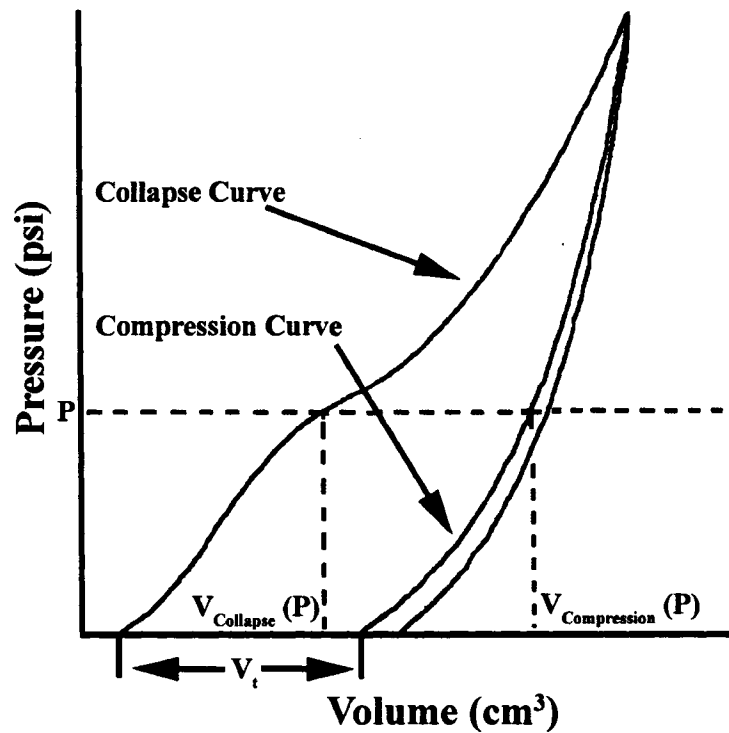


Figure 18 Compression curve from isostatic testing of batches of MBs, as per ASTM D 3102. % Survivors found from difference in compression and collapse curves. After ref. [6].

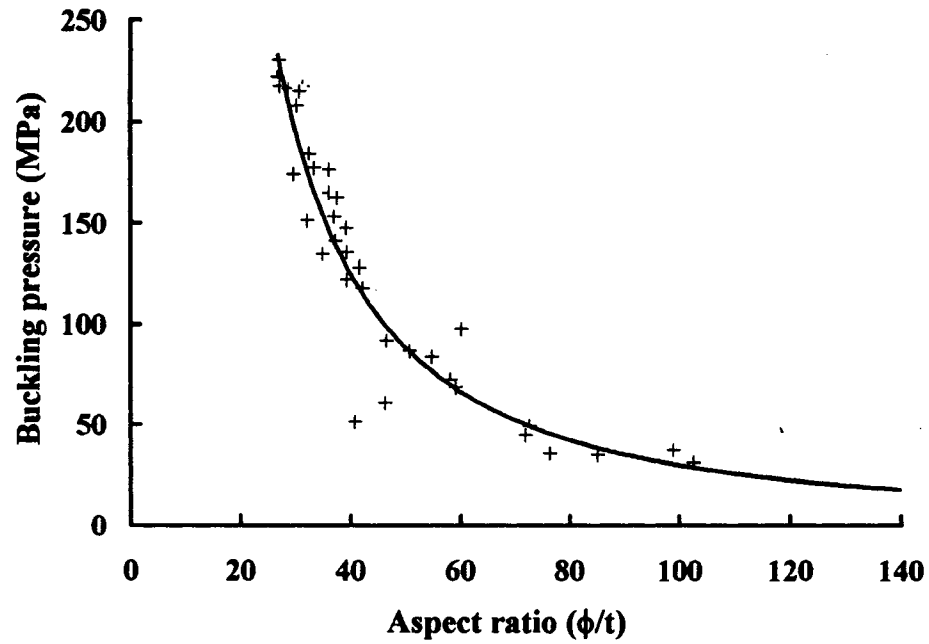


Figure 19 Aspect ratio vs. isostatic buckling pressure for individual GMBs. After ref. [13].

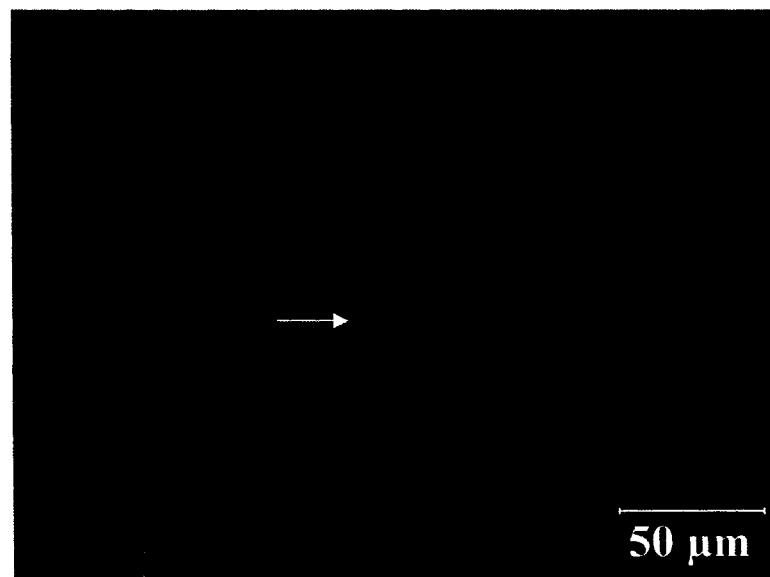
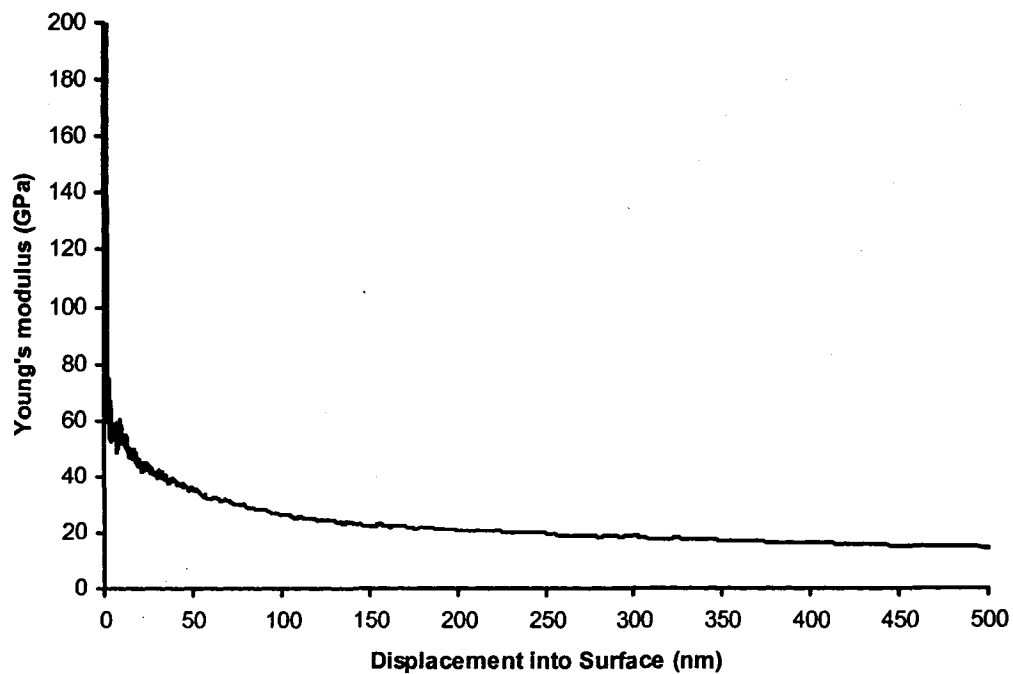


Figure 20 Optical image of CMBs used for nanoindentation. Indent located in CMB wall at white arrow. Fiducial indents also visible at lower left.



*Figure 21* Modulus vs. displacement curve for the indent in Fig. 20. Average modulus between 100 and 500 nm was 20.409 GPa.

CHARACTERIZATION OF CARBON MICROBALLOON SYNTACTIC FOAMS

by

K. B. CARLISLE, M. KOOPMAN, K.K. CHAWLA, G.M. GLADYSZ, M. LEWIS

Submitted to *Materials Science and Engineering A*

Format adapted for dissertation

## Abstract

In this paper, we report on some aspects of the microstructural and mechanical characterization of a three-phase syntactic foam composed of carbon microballoons, a bismaleamid binder, and interstitial voids. Quantitative microscopy was performed on polished cross-sections of samples of these foams, with the impetus being determination of the volume fractions of several phases in these materials. The volume fractions of nested microballoons, intact microballoons, bismaleamid binder, and carbon wall material were defined and evaluated from point counts on foam micrographs. As the percent packing of the foams evaluated increased, trends toward decreasing intact microballoons and increasing carbon wall material were observed. Foam packing was seen to have little effect on the volume fraction of bismaleamid or on nested microballoon content. Impulse excitation of parallelepipeds of this foam was also conducted, in conformance with ASTM E 1876, to determine the dynamic flexural Young's modulus of these materials at several different foam densities. Linear relationships between Young's modulus and bulk density of the foam were observed, as were similar trends with foam overpacking. Additionally, the moduli of foams composed of different microballoon tap densities were observed to fall on different linear curves.

## 1. Introduction

Syntactic foams are a class of composite materials that are of particular interest to designers of lightweight components for transportation, aerospace, or submersibles. Syntactic foams possess very good specific properties, especially compressive characteristics, due to the tailorability of their microstructures. Specifically, these materials consist of hollow particles dispersed in a binder, or matrix, phase. The microstructure of these materials is considered a designer microstructure because, unlike blown foams, the foaming operation is based on mechanically incorporating the hollow microspheres, i.e. microballoons (MBs), into the binder. Varying amounts of MBs of different average size, wall thickness, or material may be chosen to tailor the foam's properties to the application. Additionally, the binder material may be adjusted in both type and amount to achieve a particular property set for the resulting syntactic foam [1-9].

Syntactic foams may be further subdivided into three main categories: two-phase, three-phase, and multi-phase. The material characteristic distinguishing between the first two categories is interstitial void content. Foams wherein the interstitial void content is small and unintentional are two-phase foams, whereas foams that are consciously designed to possess interstitial voids, usually significant volume fractions, are three-phase foams. The multi-phase foams build upon these foams by the addition of reinforcing phases, namely fibers, rubber particles, or nanoclay [4, 7, 8, 10-13].

In this paper, we report on a specific three-phase syntactic foam, composed of carbon microballoons (CMBs), a bismaleamid binder (APO-BMI), and interstitial voids. While compressive, flexural, thermal, and shear testing of this material is available in the

literature [14-17], there is a lack of data characterizing the foam microstructurally. Specifically, we have performed quantitative microscopic measurements on polished samples of the foam microstructure and impulse excitation determination of dynamic Young's modulus for foam samples of several different bulk densities. The goals of this evaluation were to determine the modulus of this three-phase CMB syntactic foam and to gain insight into the microstructural origins of this foam's behavior in compression and flexural testing.

## 2. Experimental Procedures

### 2.1 *Quantitative microscopy*

Foams composed of 60 weight percent of CMBs (0.179 g/cm<sup>3</sup> tap density) and 40 weight percent APO-BMI (8.5 volume percent) were mounted via resin-impregnation and polished using a specially developed procedure. This procedure involved grinding on 500, 1200, and 4000 grit SiC papers with water as a lubricant, followed by a 3 μm diamond polish, and finished with a 0.04 μm SiO<sub>2</sub> chemical polish [18]. After polishing, the samples were imaged at a magnification of 500 X; at this magnification, the phases were resolved. These images were then processed in Adobe Photoshop using a digitally superimposed counting grid with 192 grid intersections on each image. The volume fractions ( $V_f$ ) of the relevant microstructural features of interest (intact CMBs, nested CMBs, APO-BMI, and carbon wall material) were found from point counts ( $P$ ) of grid intersections with the phase of interest, thus:

$$V_f = \left( \frac{P}{192} \right) \quad (1)$$

This equation is merely a restatement of the well-known equality between point fraction, areal fraction, and volume fraction for isotropic materials, adapted for use with our 192-intersection counting grid. Figure 1 provides an example of a micrograph with the superimposed count grid, where the colored dots are point counts for the features of interest. For all volume fraction measurements, counting was performed until a 95 percent confidence interval for the measurement was achieved.

## 2.2 Dynamic modulus by impulse excitation

Young's modulus was measured dynamically by impulse excitation as per ASTM E 1876. In this technique, rectangular parallelepipeds of sample are placed such that their flexural nodes of vibration rest on supports at 22.4 % of the length of the sample from either end of the parallelepiped. The bar is struck with an elastic tap and the sample's resonant frequency is measured with a handheld transducer or microphone. Figure 2 shows a schematic of the sample configuration. The dynamic, flexural Young's modulus of the sample can be calculated from the equations below [19]:

$$E = 0.9465 \left( \frac{mf^2}{b} \right) \left( \frac{L^3}{t^3} \right) T_1 \quad (2)$$

$$T_1 = 1 + 6.585(1 + 0.0752\nu + 0.8109\nu^2) \left( \frac{t}{L} \right)^2 - 0.868 \left( \frac{t}{L} \right)^4 - \left[ \frac{8.34(1 + 0.2023\nu + 0.8109\nu^2) \left( \frac{t}{L} \right)^4}{1 + 6.338(1 + 0.1408\nu + 1.536\nu^2) \left( \frac{t}{L} \right)^2} \right] \quad (3)$$

Equations (2) and (3) assume that the density and modulus of the sample are constant throughout and involve the sample's fundamental resonant frequency ( $f$ ), mass ( $m$ ), length ( $L$ ), width ( $b$ ), Poisson's ratio ( $\nu$ ), and thickness ( $t$ ).  $T_1$  is a correction factor accounting for finite sample size. The Poisson's ratio (0.15) used for these materials was

calculated based on measured Young's and shear modulus values and the assumption of isotropy.

### 3. Results and Discussion

Quantitative microscopy was performed using optical microscope images of two of the CMB foams with the primary objective of quantifying the volume fractions ( $V_f$ ) occupied by various features and phases found in the foams. Volume fractions for the following were measured: the APO-BMI binder phase, the intact CMBs, the nested CMBs, and the carbon wall material. By definition, an intact CMB was any CMB that did not fill with mounting resin during vacuum impregnation, and a nested CMB was one with an internal wall structure resulting in a multi-compartmented CMB. The amounts of both intact and nested CMBs are important to overall foam properties. Intact CMBs will have greater structural integrity than flawed CMBs [20], and nested CMBs were shown to have lower failure loads and stiffness but often higher failure strains and fracture energies than single-walled CMBs [21]. Examples of these features are shown in Fig. 1. The volume fractions were determined from manual point counts on foam microstructures, using Eqn. 1.

These data were collected for foams containing CMBs ( $0.179 \text{ g/cm}^3$  tap density, per ASTM B 527 [22]) in two different manufacturing conditions (or foam overpacking conditions). An overpacking condition in these foams is achieved by either overfilling or underfilling the mold with CMBs during foam manufacture. The tap density standard provides a measure of the volume occupied by a known mass of MBs after settling by mechanical vibration. From this tap density measurement, the mass of CMBs required to

fill a mold of a known volume may be calculated; this mass corresponds to zero percent overpacking and is often referred to as the tapped dense condition. If the volume of CMBs is increased by a given percentage above that for a tapped dense foam, the foam has that given positive percent overpacking; conversely, a foam may be produced using less CMBs than for the tapped dense condition. This foam will have a negative percent overpacking. The conditions upon which volume fractions were measured were 10 and 20 percent overpacked.

The average and standard deviation values for the microscopic parameters previously discussed are given in Table I. Analysis of the data revealed a difference in the volume fraction of APO-BMI measured in the foam compared to the amount that was expected (8.5 volume percent) from manufacturing. As Fig. 3 shows, this discrepancy is due to the resolution limits of the optical microscope. A 0.25  $\mu\text{m}$  thick layer of APO-BMI coating on each CMB wall is observed by high resolution scanning electron microscopy but could not be resolved optically; thus some undercounting was inevitable. We saw that increased overpacking caused an increase in the volume fraction of carbon and a statistically insignificant decrease in the percentage of intact CMBs, proving that overpacking resulted in a more close-packed arrangement of CMBs in the structure without inducing significant CMB breakage. The increase observed in nested CMBs, although also not statistically significant, may be due to more CMBs present as the result of overpacking and/or the higher fracture energies of nested CMBs [21].

The ultrasonic testing of this material was conducted on foams composed of CMBs of two different tap densities (0.15 and 0.179  $\text{g}/\text{cm}^3$ ). Young's modulus was measured dynamically for foams manufactured in the following conditions: 0, 10, 20, and

30 (for  $0.179 \text{ g/cm}^3$  only) percent overpacking. Figures 4 and 5 show the results.

Modulus and bulk density both increased with increased overpacking, and modulus also increased with increasing bulk density, as Gladysz et al. [14] observed in mechanical testing. The effect of tap density composition of the foams was also seen, as the modulus data sets separated by tap density. Although the two tap density foams in Fig. 5 did not overlap in bulk density, the trendlines suggest that the lower tap density would have a higher modulus at a constant bulk density. Since the lower tap density CMBs have been shown to possess thinner walls and lower failure strengths [18, 21, 23], this trend seems unexpected. However, the arrangement of carbon in the low tap density foam results in a larger number of thinner CMB walls over which loading will be distributed, because the lower tap density CMBs are overpacked to achieve the same bulk density foam as that formed from a higher tap density [14]. Furthermore, a larger number of thin CMB walls in a more close-packed arrangement results in a greater number of shorter binder bonds and more load-bearing CMB-binder interfacial area, as observed by Gladysz et al. [14] in flexural testing. Thus, our non-destructive measurements of the modulus of these carbon microballoon foams also emphasize the effect of both CMBs and binder on the foam's mechanical properties.

#### 4. Conclusions

Quantitative microscopy and impulse excitation testing of the three-phase CMB syntactic foams were performed. From image analysis, we found that the volume fraction of APO-BMI was only  $\sim 6\%$ , instead of the  $8.5\%$  expected from the manufacturer. This discrepancy was explainable by the sub-micrometer thick, optically undetectable, film of

APO-BMI distributed throughout the foam microstructure on the surfaces of most of the CMBs. Additionally, the volume fraction of carbon in the structure increased with increased overpacking, as expected. The impulse excitation data for foams of 0.15 and 0.179 g/cm<sup>3</sup> tap densities confirmed the trends in Young's modulus observed from mechanical testing of these materials. In any tap density, Young's modulus was seen to increase linearly with foam bulk density and with percent overpacking. Inter-tap density, we observed that the higher tap density samples tended to have higher Young's modulus and density values, indicative of the higher average wall thickness of the higher tap density CMBs.

## 5. Acknowledgments

This work was financially supported by Los Alamos National Laboratory/DOE subcontract #44277-SOL—02 4X. KBC is grateful to the Department of Defense for a National Defense Science and Engineering Graduate Fellowship. The authors would also like to thank O. Wilhelmi at FEI Co. LA-UR-06-6129.

## 6. References

1. G.M. GLADYSZ and K.K. CHAWLA, Composite Foams, in "Encyclopedia of Polymer Science & Technology" (John Wiley, New York, 2004) pp. 267-281.
2. N. GUPTA and E. WOLDESENBET, *Journal of Cellular Plastics* **40** (2004) 461.
3. N. GUPTA, E. WOLDESENBET, and P. MENSAH, *Composites Part A: Applied Science and Manufacturing* **35** (2004) 103.
4. M. NARKIS, S. KENIG, and M. PUTERMAN, *Polymer Composites* **5** (1984) 159.
5. M. NARKIS, M. PUTERMAN, and S. KENIG, Three-phase Glass Microballoon-containing Syntactic Foams, in Proceedings of 38th Annual Reinforced

Plastics/Composites Institute, Society of the Plastics Industry, RP/C '83: Composite Solutions to Material Challenges., Houston, TX, USA (SPI, New York, NY, USA, 1983). p. 8.

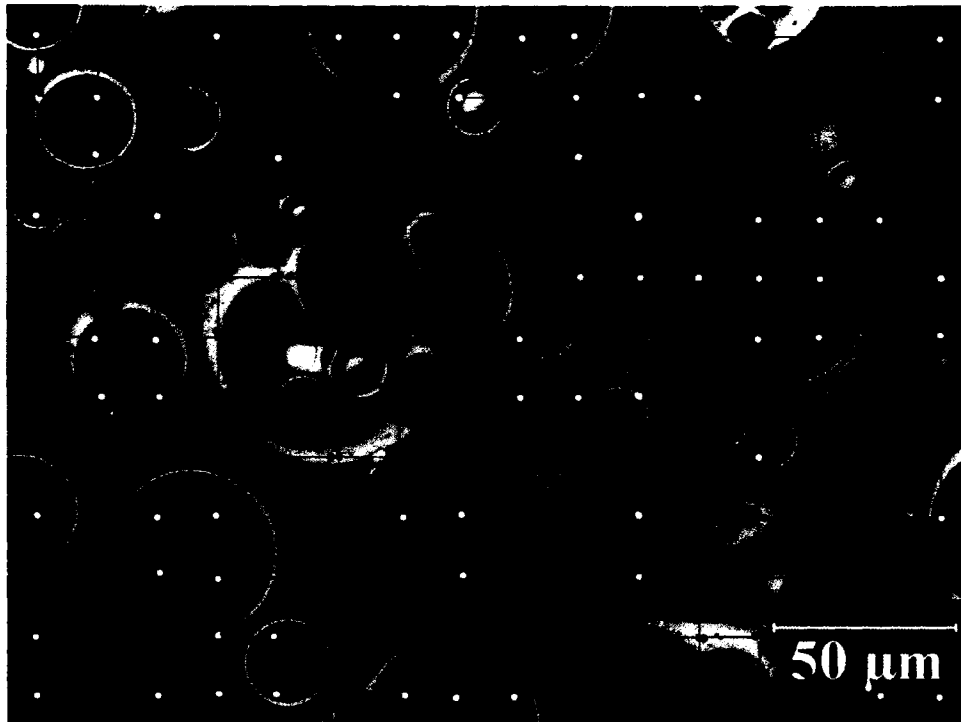
6. K. OKUNO and R.R. WOODHAMS, *Cellular Plastics* **10** (1973) 237.
7. H.L. PRICE and J.B. NELSON, *J. Composite Materials* **10** (1976) 314.
8. E.M. WOUTERSON, F.Y.C. BOEY, X. HU, and S.-C. WONG, Effect of the filler content on the specific properties of syntactic foam, in Proceedings of ANTEC 2004, Chicago, IL., United States (Society of Plastics Engineers, 2004). pp. 3176-3180.
9. E.M. WOUTERSON, F.Y.C. BOEY, X. HU, and S.-C. WONG, *Composites Science and Technology* **65** (2005) 1840.
10. N. GUPTA, *JOM* **56** (2004) 342.
11. N. GUPTA, G. LI, H.D. JERRO, E. WOLDESENBET, and S.-S. PANG, Effect of nano-size clay particles on the flexural properties of syntactic foams, in Proceedings of ANTEC 2004, Chicago, IL., United States (Society of Plastics Engineers, 2004). pp. 1320-1324.
12. N. GUPTA, R. MAHARSIA, and H. DWAYNE JERRO, *Materials Science and Engineering A* **395** (2005) 233.
13. M. PUTERMAN, M. NARKIS, and S. KENIG, *Journal of Cellular Plastics* **16** (1980) 223.
14. G.M. GLADYSZ, B. PERRY, G. MCEACHEN, and J. LULA, *J. Mater. Sc.* **41** (2006) 4085.
15. G. CHAVEZ, M. LEWIS, and L. LENKE, *Journal of Materials Science* **41** (2006) 4015.
16. G.W. MCEACHEN, Carbon Syntactic Foam Mechanical Properties Testing. Topical Report: KCP-613-6043. (Kansas City) 1998.
17. V. SHABDE, K. HOO, and G. GLADYSZ, *Journal of Materials Science* **41** (2006) 4061.
18. K. CARLISLE, K.K. CHAWLA, G. GOUADEC, M. KOOPMAN, and G.M. GLADYSZ, Nanocompressive properties of carbon microballoons and mechanical properties of carbon based syntactic foam composites, in Proceedings of ICCM-14, San Diego, CA, July 2003 (Society of Manufacturing Engineers, 2003).

19. S. SPINNER, T.W. REICHARD, and W.E. TEFFT, *Journal of Research of the National Bureau of Standards--A. Physics and Chemistry* **64A** (1960).
20. K.B. CARLISLE, M. LEWIS, K.K. CHAWLA, M. KOOPMAN, and G.M. GLADYSZ, *In preparation for Acta Materialia* (2006).
21. K.B. CARLISLE, M.C. KOOPMAN, K.K. CHAWLA, R.K. KULKARNI, G.M. GLADYSZ, and M. LEWIS, *J. Mater. Sci.* **41** (2006) 3987.
22. ASTM B 527: Standard Test Method for Determination of Tap Density of Metallic Powders and Compounds, in "Annual Book of ASTM Standards" (American Society for Testing and Materials, 2000).
23. G. GOUADEC, K. CARLISLE, K.K. CHAWLA, M.C. KOOPMAN, G.M. GLADYSZ, and M. LEWIS, Nano-compression of carbon micro-balloons with a flat-ended cylindrical indenter, in Proceedings of Indentation Techniques in Ceramic Materials Characterization, Apr 27-30 2004, Nashville, TN., United States (American Ceramic Society, 2004). pp. 143-152.

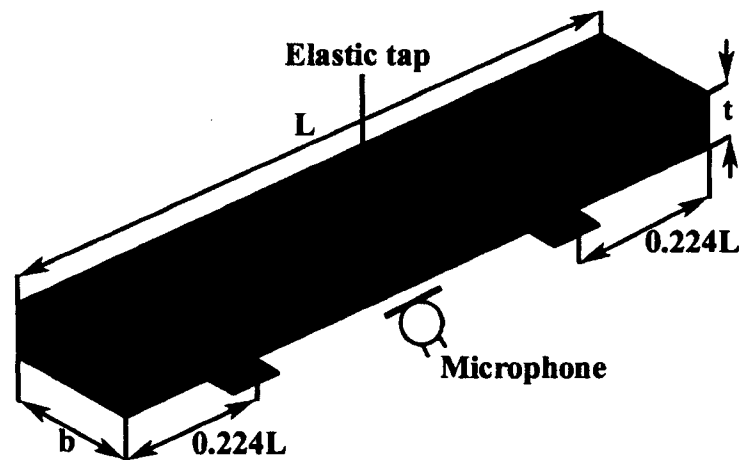
## 7. Tables and Figures

TABLE I: Measured volume fraction of constituents in CMB foams.

Foam Condition	10 percent	20 percent
$V_f$ APO-BMI (%)	$6.52 \pm 0.65$	$5.54 \pm 1.52$
$V_f$ Nested CMB (%)	$21.38 \pm 2.28$	$24.78 \pm 2.39$
$V_f$ Intact CMB (%)	$62.34 \pm 2.36$	$59.95 \pm 2.72$
$V_f$ C walls (%)	$5.38 \pm 0.54$	$7.22 \pm 1.92$



*Figure 1* Example micrograph for volume fraction determination. The counting grid has 192 intersections and shows sample point counts for APO-BMI (blue), nested CMBs (aqua), intact CMBs (yellow), and carbon (violet).



*Figure 2* Schematic of the configuration for impulse excitation determination of Young's modulus. The locations of the supports, the microphone, and the elastic tap are shown, relative to the sample's length ( $L$ ), width ( $b$ ), and thickness ( $t$ ).

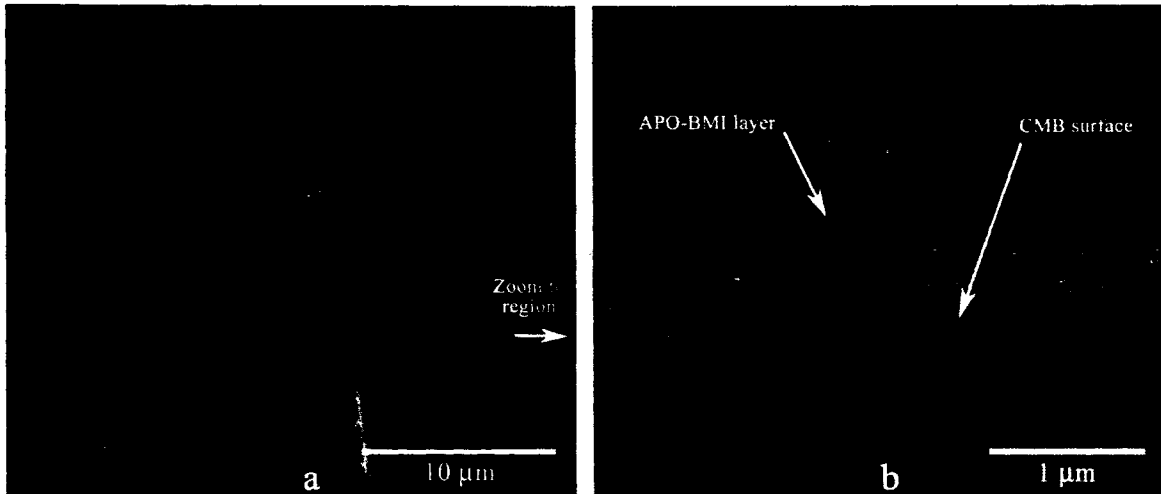


**Figure 3** Micrograph of carbon microballoon syntactic foam surface. SEM. (a) This micrograph shows a CMB and the APO-BMI at a foam fracture surface. (b) Zoom of a region of the CMB's surface that shows a thin layer of APO-BMI that coats the CMBs in the foam. (SEM by O. Wilhelmi at FEI Co.)

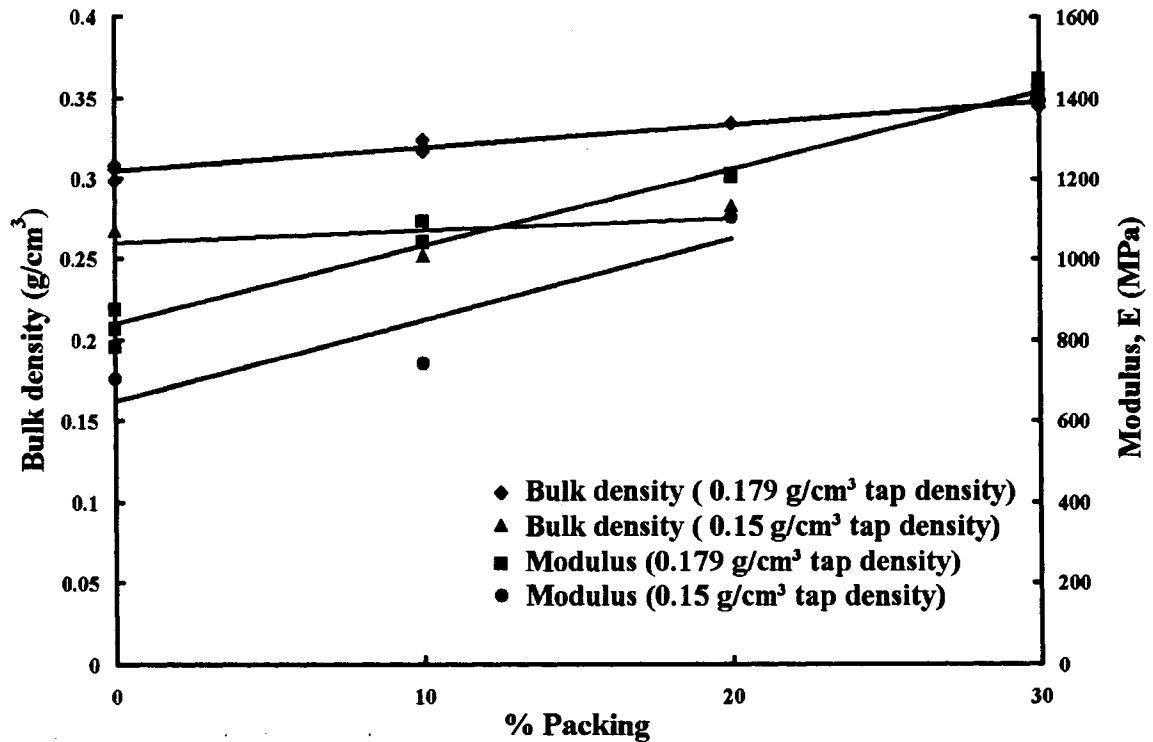


**Figure 4** Modulus and bulk density vs. foam packing. Both are linearly increasing functions of percent packing within the range of values tested.

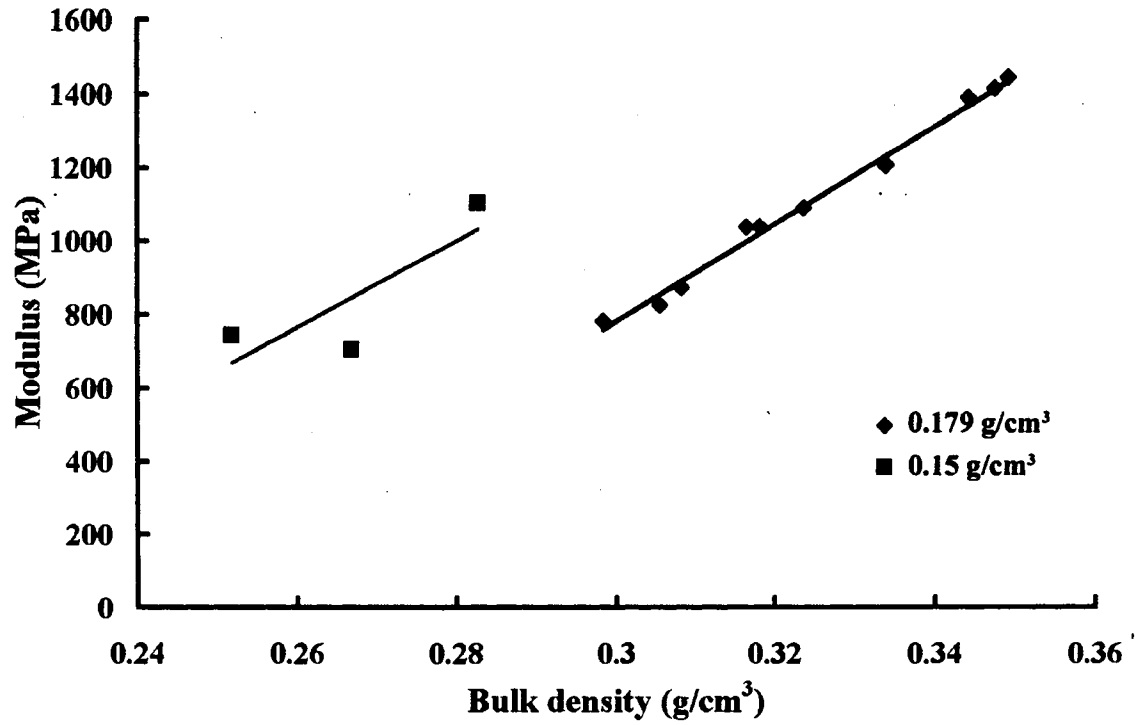


Figure 5 Modulus vs. bulk foam density. Modulus is a linear function of density.

CHARACTERIZATION OF THE BINDER PHASE IN A THREE-PHASE CARBON  
MICROBALLOON SYNTACTIC FOAM

by

K. B. CARLISLE, G.M. GLADYSZ, K.K. CHAWLA, M. KOOPMAN, M. LEWIS

In preparation for *Materials Characterization*

Format adapted for dissertation

## Abstract

In three-phase syntactic foams, the binder phase plays the vital role of holding the compressive load bearing microballoon components in place. The binder is generally a polymer. It is important to characterize the binder as part of any effort to characterize three-phase syntactic foams. To obtain thermal and mechanical properties, we have performed differential scanning calorimetry and nanoindentation on samples of the binder resin used in a three-phase carbon microballoon syntactic foam system. The binder of this foam is a specific variety of bismaleamid known as APO-BMI, which differs from the prototypical bismaleamid in that it has an extra methyl group and two sulfur atoms between the central benzene rings. Through differential scanning calorimetry, we determined that the melting temperature of neat APO-BMI is 120 °C and that the curing exotherm onsets at 230 °C. The presence of carbon microballoons was seen to affect the curing reaction of APO-BMI, reducing the onset of curing by 25 °C and decreasing the heat of reaction for curing. The Young's modulus of cured APO-BMI was determined by nanoindentation to be 6.6 GPa.

## 1. Introduction

Characterization of the polymeric binder phase, APO-BMI, in a three-phase carbon microballoon (CMB) syntactic foam is necessary to better understand the properties of the entire system. This is especially important in three-phase foams, where the volume fraction of the binder phase can be very low [1]. Thus, there is a very small amount of material binding the microballoons (MBs) in place in a molded foam structure, and the mechanical properties of the binder can have a large impact on the behavior of the overall foam. Specifically, the binder has been shown to exert the greatest influence on the tensile and flexural strengths of three-phase foams [2-6]. Additionally, the properties of the binder phase are required for finite element modeling efforts of three-phase syntactic foams.

Figure 1 shows the chemical structure of APO-BMI [2, 7, 8]. Since it is very difficult to obtain solid samples for testing, the characterization effort was limited in scope. Both differential scanning calorimetry (DSC) and nanoindentation were performed to characterize the available APO-BMI samples. The objective of the DSC study was to determine the melting temperature ( $T_m$ ), curing reaction temperature, and the glass transition temperature ( $T_g$ ) of the APO-BMI. Additionally, comparison of the DSC results from neat APO-BMI and APO-BMI in-the-foam was performed to elucidate the possible effects of the CMBs on the curing reaction. Nanoindentation of this material was done to obtain the Young's modulus and hardness from very small samples of cured APO-BMI.

## 2. Experimental Procedure

### 2.1 Differential scanning calorimetry

DSC of the neat APO-BMI and of the APO-BMI in the syntactic foam was performed in a differential scanning calorimeter (TA Instruments Q100), with modulated DSC capability. All *in situ* APO-BMI data were taken from samples of nominally 60 weight percent CMBs and 40 weight percent APO-BMI, mixed such that the uncertainty in weight measurement allowed actual weight percents to range from 59.07 to 60.06 for the CMBs and from 39.95 to 40.87 for the APO-BMI. The heats of curing for all *in situ* samples were normalized for the APO-BMI content of the foam. Additionally, DSC data were taken for the same neat APO-BMI and foam in the cured condition, in an attempt to detect the  $T_g$  of the APO-BMI. Initial investigation of the curing of the APO-BMI samples was performed using standard DSC runs, from 35 to 350 °C at 10 °C/min. The data taken on the APO-BMI in the cured condition, however, were obtained using modulated DSC, enhancing the sensitivity for better detection of the  $T_g$  of APO-BMI. Modulated tests again covered the same temperature range, but reduced the heating rate to 5 °C/min. All DSC experiments used sealed sample containers and a nitrogen gas atmosphere.

### 2.2. Nanoindentation

Nanoindentation, using a nanoindentation system (MTS Nano Instruments XP II), was performed on APO-BMI samples to determine their Young's modulus and hardness. The APO-BMI studied were *in situ* samples on a polished sample of syntactic foam and a small piece of neat, cured APO-BMI. The continuous stiffness measurement (CSM)

technique of the MTS indenter allowed modulus and hardness data as a function of Berkovich indenter tip penetration into the surface to be gathered [9, 10]. As APO-BMI is a very brittle thermosetting polymer, the CSM technique was invaluable because it allowed indentation data to be taken from shallow indentation depths (less than 1  $\mu\text{m}$ ) in the neat APO-BMI samples, beyond which point crack propagation at the corners of the indent would occur. For the neat samples, care was also taken to avoid indentations near regions of high porosity. In the *in situ* condition, precise indentation placement, at the binder pools between CMBs, was critical. Additionally, averages for hardness and modulus had to be taken from plateaus at very shallow indentation depths (less than 500 nm), both to avoid edge effects from the nearby CMB walls and to stay within the limited volume of APO-BMI (no more than a few  $\mu\text{m}^3$ ) at the binder necks between CMBs.

### 3. Results and Discussion

Earlier, unpublished, calorimetry work by Honeywell Federal Manufacturing & Technologies and Los Alamos National Laboratory on this material had revealed that the APO-BMI melts between 118 and 122  $^{\circ}\text{C}$  and initiates curing near 210  $^{\circ}\text{C}$  [2, 7, 8]. We wished to verify these results and compare the behavior of the neat APO-BMI to that of APO-BMI in the foam, i.e., when mixed with CMBs in the same proportions as in the foam. Figures 2 and 3 provide representative DSC curves of the curing reaction from APO-BMI, neat and *in situ* with CMBs, respectively. As can be seen in both figures, the APO-BMI exhibited a distinct melting endotherm, for which the average and standard deviation was  $119.89 \pm 0.06$   $^{\circ}\text{C}$ . Both neat and foam samples also exhibited a curing exotherm, or heat evolution resulting from the homopolymerization cross-linking

reaction. An interesting discovery was the temperatures at the onset and the peak of the curing reaction. In neat APO-BMI, their average and standard deviations were at  $217.43 \pm 15.53$  and  $276.63 \pm 7.44$  °C, respectively. However, Fig. 3 showed a reduction in these temperatures for the APO-BMI in the foam, to 205 and 270 °C. This theory is further supported by the heats of reaction calculated from the area under the cure exotherms. This value's average and standard deviation for the neat APO-BMI was  $214.41 \pm 2.84$  J/g, which is significantly greater than that for the APO-BMI in the foam, viz. 188 J/g. This indicated that the curing reaction was more energetically favorable for the APO-BMI in the foam. Various forms of carbon have been shown to affect curing of other thermoset-based composites [11-14], thus it is hypothesized either that the CMBs are catalyzing the reaction or that the thermal conductivity of the CMB phase is affecting the cure behavior. Considerable further study, at various heating rates, would be required to verify which mechanism caused the behavior.

A secondary interest was determining the  $T_g$  of the APO-BMI. Thus, a second DSC run was performed on each of the neat and in-the-foam samples, after curing. This was intended to detect the concavity changes and inflection points in the heat flow and reversible heat flow graphs that would indicate the presence of the  $T_g$ . In all neat samples, no  $T_g$  was apparent; however, for APO-BMI in-the-foam, the average and standard deviation for the  $T_g$  was detected as  $330.41 \pm 0.86$  °C. The concavity changes, inflection points, and their associated  $T_g$  are labeled on the reversible heat flow graph in Fig. 4. The  $T_g$  was validated by plotting the derivative of the heat capacity with respect to temperature versus temperature. The small peak at the  $T_g$  temperature confirmed the existence of the  $T_g$  at 330 °C in the APO-BMI in the foam, see Fig. 4. Presumably the

lack of a  $T_g$  in neat APO-BMI occurred because of its greater crystallinity vs. the *in situ* samples, but the lack of a totally crystalline reference standard for APO-BMI prevented determination of the percent crystallinity. Since the  $T_g$  observed is well above the service parameters for the foam, further investigation was not necessary.

Nanoindentation tests were performed on APO-BMI, both neat and *in situ* in the syntactic foam, and this test represents, to our knowledge, the only mechanical property data available for this material. Using the CSM technique, indentations were performed on APO-BMI in the foam, as shown in Fig. 5. *In situ* measurements yielded average and standard deviation values for Young's modulus and hardness of  $5.88 \pm 1.55$  and  $0.49 \pm 0.18$  GPa, respectively. These values, from approximately a dozen successful indentations, compare quite favorably with the average and standard deviations,  $6.60 \pm 0.339$  and  $0.460 \pm 0.029$  GPa, for Young's modulus and hardness respectively, taken from 163 successful indents into a neat APO-BMI sample. Statistical treatment of the values from the neat APO-BMI found the 99 percent confidence intervals for the measurements to be  $6.60 \pm 0.05$  and  $0.460 \pm 0.004$  GPa, for Young's modulus and hardness respectively. Figure 6 provides an example micrograph of 10 indents on the neat sample, revealing the necessity of taking data from shallow depth due to the brittle nature of the sample—vis-à-vis the cracks formed at the corners of the 2  $\mu\text{m}$  deep indents. Thus, we have good agreement regarding the measured modulus and hardness values for APO-BMI.

#### 4. Conclusions

Differential scanning calorimetry was performed on neat APO-BMI and in APO-BMI in the syntactic foam, investigating the melting temperature, curing reaction, and glass transition temperature of the APO-BMI. The melting temperature of the APO-BMI was found to be 120 °C regardless of the presence of CMBs, but the onset and peak temperatures of the curing reaction were found to be lower for APO-BMI in-the-foam. Additionally, the heat of reaction for curing of APO-BMI was found to be lower in the presence of CMBs, suggesting that the CMBs may affect the curing behavior. Young's modulus and hardness of APO-BMI were obtained at room temperature, using a nanoindenter, and were found to be 6.6 and 0.46 GPa, respectively.

#### 5. Acknowledgments

This work was financially supported by Los Alamos National Laboratory/DOE subcontract #44277-SOL—02 4X. The authors are grateful to Dr. D. Dean for the use of DSC equipment and helpful discussions. KBC is grateful to the Department of Defense for a National Defense Science and Engineering Graduate Fellowship. LA-UR-06-6129.

#### 6. References

1. H.L. PRICE and J.B. NELSON, *J. Composite Materials* **10** (1976) 314.
2. G.M. GLADYSZ, B. PERRY, G. MCEACHEN, and J. LULA, *J. Mater. Sc.* **41** (2006) 4085.
3. M. KOOPMAN, K.K. CHAWLA, G. GLADYSZ, and K.B. CARLISLE, *J. Mater. Sci.* **41** (2006) 4009.
4. M. NARKIS, S. KENIG, and M. PUTERMAN, *Polymer Composites* **5** (1984) 159.

5. M. NARKIS, M. PUTERMAN, and S. KENIG, *Journal of Cellular Plastics* **16** (1980) 326.
6. M. PUTERMAN, M. NARKIS, and S. KENIG, *Journal of Cellular Plastics* **16** (1980) 223.
7. G.W. MCEACHEN, Carbon Syntactic Foam Mechanical Properties Testing. Topical Report: KCP-613-6043. (Kansas City) 1998.
8. L.L. WHINNERY, S.H. GOODS, M.L. TOOTLE, and C.L. NEUSCHWANGER, TEPIC-A New High Temperature Structural Foam. Topical Report: SAND98-8246. (Albuquerque) 1998.
9. X. LI and B. BHUSHAN, *Materials Characterization* **48** (2002) 11.
10. G.M. PHARR, *Materials Science and Engineering A* **253** (1998) 151.
11. D. PUGLIA, L. VALENTINI, I. ARMENTANO, and J.M. KENNY, *Diamond and Related Materials* **12** (2003) 827.
12. H. XIE, B. LIU, Q. SUN, Z. YUAN, J. SHEN, and R. CHENG, *Journal of Applied Polymer Science* **96** (2005) 329.
13. H. XIE, B. LIU, Z. YUAN, J. SHEN, and R. CHENG, *Journal of Polymer Science, Part B: Polymer Physics* **42** (2004) 3701.
14. J. KIM, T.J. MOON, and J.R. HOWELL, *Journal of Composite Materials* **36** (2002) 2479.

## 7. Figures

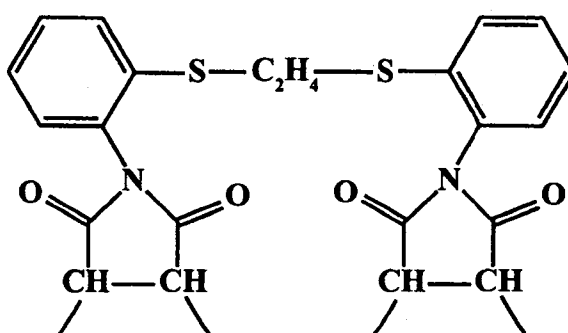


*Figure 1* Chemical structure of cured APO-BMI. The sulfur atoms, one CH<sub>2</sub> group, and the location of the nitrogen bonds are the differences between APO-BMI and the prototypical bismaleimid (BMI).

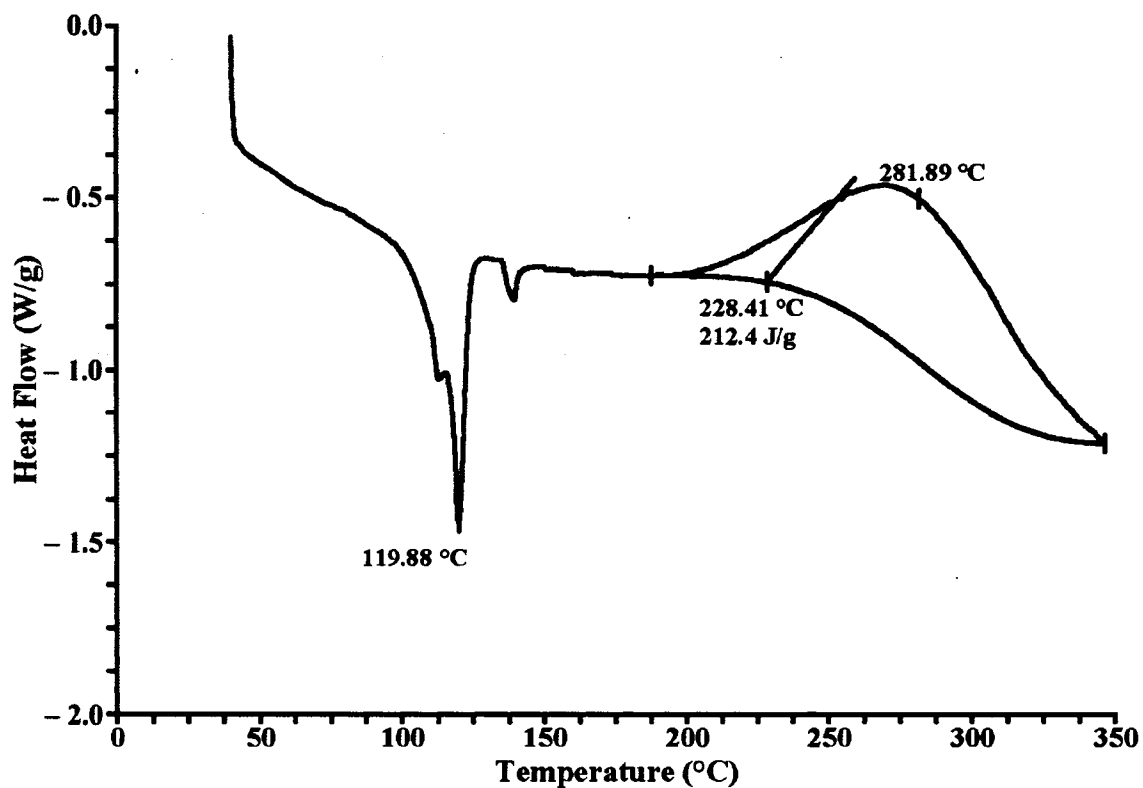


*Figure 2* DSC curve of neat APO-BMI. The melting endotherm is at 119.88 °C, and the curing exotherm onsets at 228.41 °C. The heat of curing, determined as the area under the curing exotherm, is 212.4 J/g.

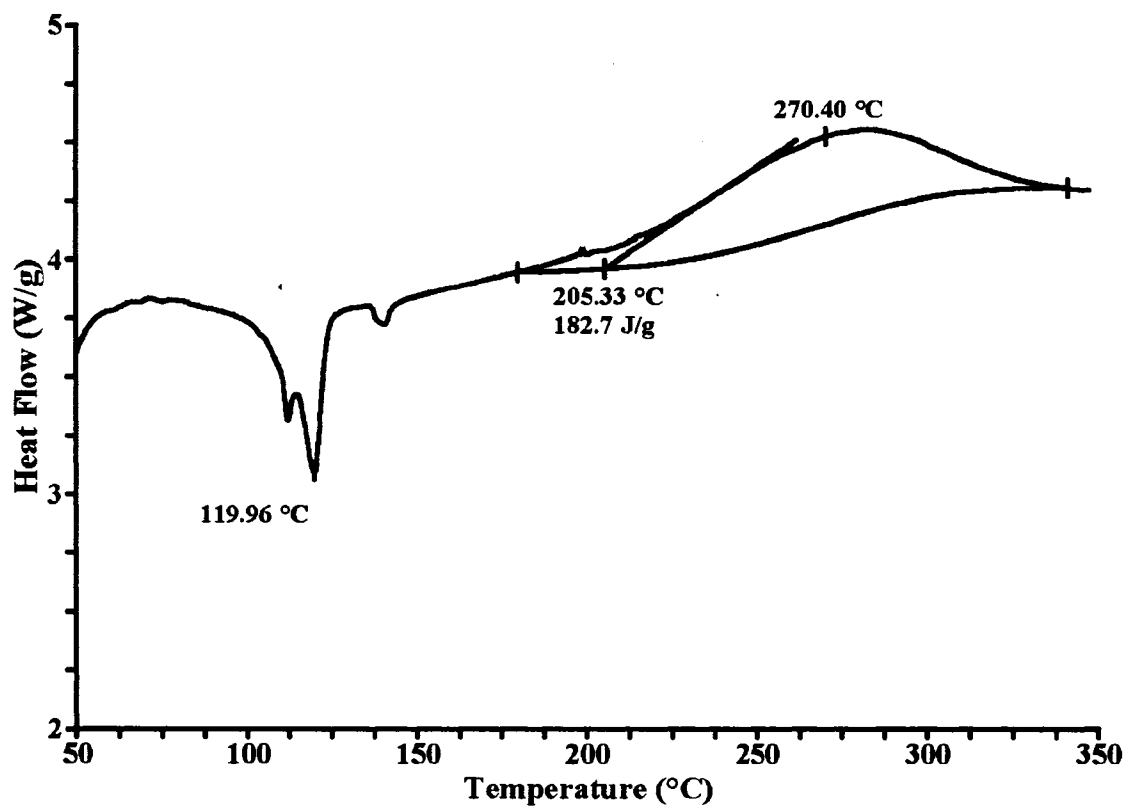


*Figure 3* DSC curve for blend of 60 weight percent CMBs and 40 weight percent APO-BMI. The melting endotherm of APO-BMI was unchanged by the presence of the CMBs, but the curing exotherm shifted to 205.33 °C. The heat of curing, 182.7 J/g, was also seen to decrease with the addition of CMBs.

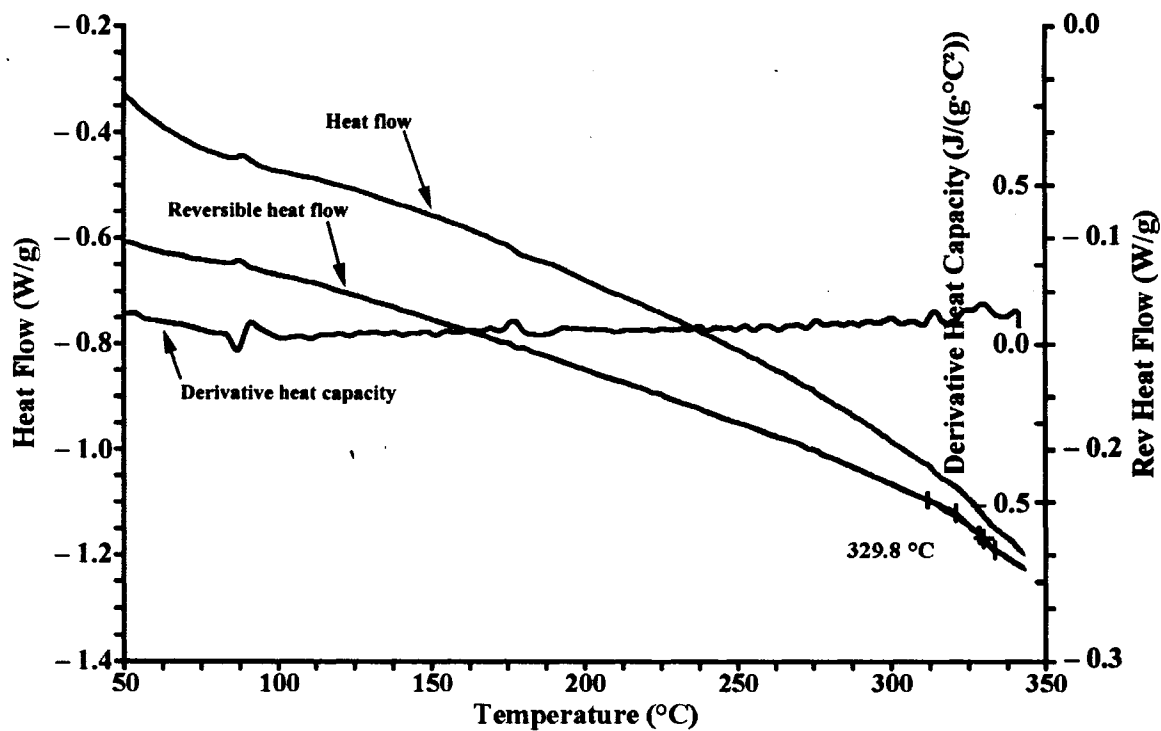


*Figure 4* DSC curve of cured syntactic foam. The concavity changes and inflection points (superimposed black lines and crosses) in the heat flow and the reversible heat flow graphs suggest that the  $T_g$  of APO-BMI is at 329.8 °C. A small peak in the derivative heat capacity curve confirmed the presence of the  $T_g$ .

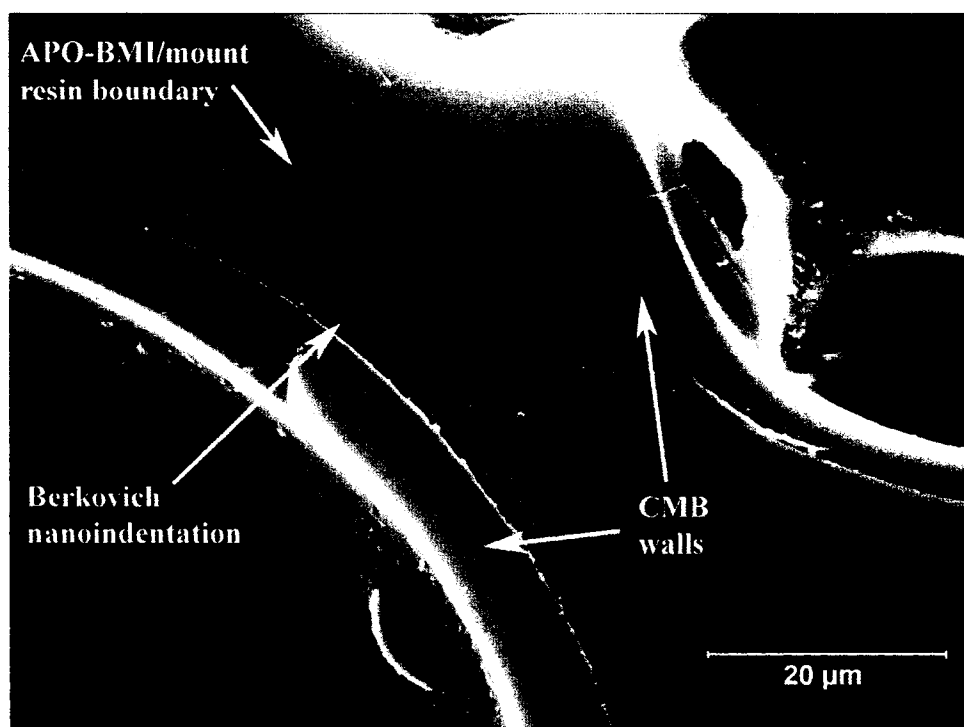


*Figure 5* Micrograph of *in situ* nanoindentation of APO-BMI. Nanoindentation is barely visible between CMBs (black dotted lines added for emphasis). The boundaries between the APO-BMI and the mount resin were also enhanced with white dotted lines, for ease of viewing. Data taken from such indents were restricted to shallow depths to avoid edge effects. SEM.

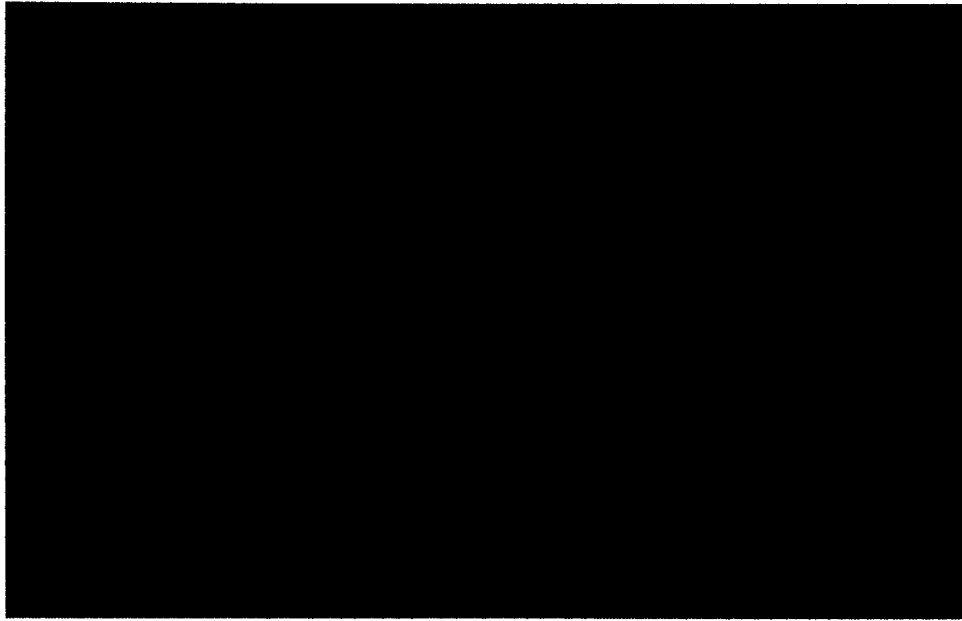


*Figure 6* Optical micrograph of nanoindentations in APO-BMI. Cracks around indents emphasize the brittle nature of cured APO-BMI and the necessity of the CSM technique, which allows extraction of mechanical properties from shallow depths in this material, before cracking has occurred.

MICROSTRUCTURE AND COMPRESSIVE PROPERTIES OF CARBON  
MICROBALLOONS

by

K. B. CARLISLE, M. KOOPMAN, K.K. CHAWLA, R. KULKARNI, G.M. GLADYSZ, M.  
LEWIS

*Journal of Materials Science* 41 (2006) 3987.

Copyright

2006

by

Springer Science + Business Media, Inc.

Used by permission

Format adapted and errata corrected for dissertation

## Abstract

Carbon microballoons (CMBs) with tap densities of 0.143, 0.161, and 0.177 g/cm<sup>3</sup>, as measured per ASTM B 527-93, were characterized in terms of individual balloon diameter, wall thickness, and mechanical behavior in compression through a novel uniaxial compression test technique. This compression test, performed on an MTS Nanoindenter XP II, utilized a flat-ended cylindrical tip rather than the common Berkovich indenter. Quantitative microscopy techniques were used to obtain diameter and wall thickness measurements on the polished cross-sections of individual CMBs that had been cold mounted in epoxy resin. Though there was significant overlap in the three populations, a trend toward increasing average wall thickness—from 1.32 to 2.16  $\mu\text{m}$ —with increasing tap density was observed. Compressive property data including failure load, failure strain, fracture energy, and stiffness were obtained for individual microballoons. Comparison of these data, both inter- and intra-tap density, has yielded some viable trends. CMB failure strain exhibited a dependence upon the inverse square root of the CMB diameter, and CMB failure load depended linearly upon CMB stiffness. Averages for each tap density's failure load, pseudo-stiffness, and fracture energy were also calculated and observed to increase with tap density.

## 1. Introduction

Syntactic foams are a type of composite that is currently garnering considerable interest. In the increasing drive toward higher fuel efficiency, these foams are of especial importance. They provide a lightweight, high specific property component for composite beams and other structural applications in the transportation industry, and offer similar advantages to the aerospace and defense markets. In these foams, the voids are achieved by incorporating microballoons in the matrix thus utilizing the traditional blowing process only to produce the microballoons. Microballoons of ceramic, polymeric, or even metallic composition provide the voids through their geometry—namely a small, hollow, spherical shell. Syntactic foams currently exist in two basic varieties: two-phase and three-phase. The two-phase foams consist of microballoons surrounded by a continuous matrix material, whereas a three-phase foam has a polymeric matrix phase that does not completely occupy the voids between the microballoons. Multiphase foams merely build upon these two basic syntactic foams. Figure 1 provides an example of a three-phase carbon microballoon (CMB) syntactic foam [1-3].

With research on the characterization and modeling of these foams intensifying, mechanical property data for the constituents becomes increasingly important. While data are often readily available for the binder phase, the same is not the case for the microballoons. Much of this inequity has stemmed from the lack of mechanical testing abilities for such small specimens; most microballoons used in syntactic foams are less than 500  $\mu\text{m}$  in diameter, with many foams utilizing microballoons in the size range of 1-150  $\mu\text{m}$ . Recent advances in materials testing equipment, combined with innovative

adaptations, are allowing mechanical property information to be extracted from single microballoons.

There are several different material types of microballoons, as well as subcategories within each type, that may be used to construct syntactic foam. Glass and phenolic are two common materials in which microballoons are commercially available. Glass microballoons (GMBs) are often categorized according to size, wall thickness, and isostatic crush strength, thus providing some idea of their expected properties. However, this is not necessarily the case for other types of microballoons, including the carbon microballoons studied here. Instead, these CMBs are demarcated only by their tap density, an ASTM standard measurement (B 527) of the volume occupied by a known mass of powder after a suitable settling procedure. This test was originally intended as a measure of the bulk properties of metallic or ceramic powders, but it is now applied to microballoons. Tap density testing provides a measure of the average wall thickness of a particular test lot, assuming that each lot has similar settling behavior, but yields no indication of individual microballoon properties [4-7].

## 2. Experimental Procedure

### 2.1 *Quantitative microscopy*

Determination of microballoon size and wall thickness complements the data from compressive testing. The original problem of examining the CMBs was that of obtaining proper cross-sectional images. This was solved by developing a unique polishing procedure for use with the highly porous CMB foam [5]. Further adaptation of this technique has led to the mounting of CMBs in epoxy resin, and subsequent polishing.

Note that most CMBs, when mixed with epoxy for mounting, float. This difficulty was alleviated by double mounting the specimens. First, CMBs were mixed into resin, which hardened with most CMBs rising to the top surface of the mount. These mounts were then sectioned using a diamond wafering saw and re-mounted in epoxy at an orientation perpendicular to the original mounting orientation. This allowed polishing through a cross-section of the CMB-rich surface layer of the original mount. Random optical images (see Fig. 2) of this surface were then taken at 500 X magnification, and the minimum and maximum diameter and wall thickness of each single walled microballoon were measured. It must be recognized that these measurements are mean lineal intercepts ( $\lambda$ ) and not direct measures of wall thickness or diameter because the location of the sectioning plane through each microballoon is unknown. If the balloon were sectioned along its great circle, then the measurements would be the actual diameter ( $\phi$ ) and thickness ( $t$ ); however, if the sectioning plane lay above or below a great circle, as illustrated in Fig. 3, the measured diameters will be less than the actual diameter and the measured intercept through the wall will exceed the actual radial measure. Since the location of the sectioning plane of each CMB was unknown, statistical methods were applied to the mean lineal intercept measurements, providing the calculated diameter or wall thickness. The formula relating the mean lineal intercept ( $\lambda_{diameter}$ ) through a spherical object to the diameter ( $\phi$ ) is [8]

$$\phi = \left(\frac{3}{2}\right)\lambda_{diameter} \quad (1)$$

Starting from the definition of the mean lineal intercept, which states that the intercept is four times the volume divided by the surface area per unit volume, and the geometric

relationship between the internal diameter, external diameter, and thickness of a spherical shell, the wall thickness can be related to the actual diameter and measured mean lineal intercept:

$$\bar{\lambda}_{wall} = \frac{4t(t^2 - 1.5t\phi + 0.75\phi^2)}{3(t^2 - t\phi + 0.5\phi^2)} \quad (2)$$

Equation 2 was solved for each measured CMB, using that particular CMB's corrected diameter and mean lineal intercept. These data have been used to calculate average thicknesses for each tap density, in addition to obtaining individual thickness vs. diameter graphs.

## 2.2 Compression testing of individual microballoons

Three lots of carbon microballoons were selected for this study. They are distinguished by tap density; approximately 140 CMBs from each 0.143, 0.161, and 0.177 g/cm<sup>3</sup> tap density lot were subjected to uniaxial compression testing, on a micrometer-level scale. Although this procedure has been delineated in detail elsewhere [4], a brief description will be presented here. A Nanoindenter XP II by MTS Nano was adapted to take advantage of its 0.02 nm displacement resolution and 50 nN load resolution to perform the compression test. In this endeavor, a polished Al substrate is inserted into the indenter's specimen stage, and a flat-ended sapphire tip is substituted for the typical Berkovich indenter. These two surfaces become the lower and upper platens, respectively, for the compression of individual microballoons that were carefully placed on the Al surface prior to testing. A schematic representation of this apparatus is shown in Fig. 4. The load cell and x-y planar movement of the instrument were calibrated prior to testing, ensuring both the accuracy of measurement and the uniaxiality of the test.

These compressive tests yielded very accurate load and platen displacement data for the compression of individual CMBs from each tap density, as well as a measurement on the  $x$ - $y$  plane of the CMB's diameter ( $\phi_h$ ) via the attached optical microscope.

Failure loads ( $P_f$ ) for each CMB were obtained by this test. Careful consideration of the test geometry also indicates that the displacement data yielded an accurate measure of the diameter ( $\phi_v$ ) of each CMB—it was the total distance traveled by the sapphire indenter from initial contact with the microballoon until contact with the Al substrate. Note that the subscript  $v$  indicates that  $\phi_v$  is what we term the vertical diameter, which, due to the imperfectly spherical nature of the CMBs, may not exactly equal the horizontal diameter measurement. The failure point also provided the displacement at failure ( $\delta_f$ ), which was used in conjunction with the diameter to define the failure strain ( $\epsilon_c$ ) of each CMB as follows:

$$\epsilon_c = \left( \frac{\delta_f}{\phi_v} \right) \quad (3)$$

The linear loading segment is characterized by a pseudo-stiffness ( $k$ ) of the CMB. This is essentially a spring constant term, and is presumably a function of: the modulus of the carbon in the CMB's walls, the CMB's diameter, the CMB's wall thickness, and the CMB's concentricity. Another useful parameter obtainable from the load-displacement curve is the work of fracture ( $W_f$ ) for the microballoon:

$$W_f = \frac{1}{2} P_f \delta_f \quad (4)$$

This term is obtained as illustrated in Fig. 5 for single-wall CMBs; but is actually the sum of several such triangular or trapezoidal areas for CMBs of more complicated

morphology. The expression for the work of fracture in terms of the properties obtainable from compression testing ( $P_f$  and  $\phi_v$ ) is,

$$W_f = \frac{AP_f^2 \phi_v \sqrt{1 - \nu^2}}{4Et^2} \quad (5)$$

where the Young's modulus ( $E$ ) of the CMB wall material was selected as 12 GPa, (a reasonable value based on nanoindentation work) Poisson's ratio ( $\nu$ ) was chosen as 0.22 (valid for this type of carbon), and  $A$  is a tabulated coefficient that varies from 0.433 to 0.286, depending on the MB to platen contact area and the MB's diameter [9]. The wall thickness used was the average calculated value for each tap density.

### 3. Results

#### 3.1 CMB morphology

The initial assumption was that a microballoon was a spherical shell of essentially constant wall thickness; however, the actual structure of these CMBs is much more irregular. Figure 6, a scanning electron microscope (SEM) image, shows that while many of the CMBs are indeed roughly spherical, there are also many complicated, non-spherical shapes. Note the conjoined (circled region) and broken (arrow) CMBs in the micrograph. These can certainly not be approximated as a spherical shell. Cross-sectional images revealed many other issues, the two most significant of which are wall thickness variations and the presence of multi-compartmented interiors, i.e., nested CMBs, see Fig. 7.

Based on the microstructures of the CMBs shown above, it is obvious that there should be large differences in mechanical response based on the CMB's morphology. Therefore, the CMBs have been classified as either single walled (SW) or nested (N).

These two types of CMB do indeed possess distinctive loading behavior, as can be seen in Fig. 8 [5]. A third category is also presented. The behavior of these flawed-single walled (FSW) CMBs falls between that of the other two types; there is a single loading region that has a non-linear nature. The FSW CMB category was observed consistently and is thought to be the result of CMBs that have either surface irregularities or defects within their walls.

### *3.2 Wall thickness and diameter*

Statistically valid quantitative microscopy formulae (Equations 1 and 2) were applied to mean lineal intercept data on wall thickness and diameter from individual CMBs of each tap density to yield calculated average thickness and diameter. The cross-sectional wall thickness vs. diameter for similar population sizes from each tap density is plotted in Fig. 9. Additionally, overall average wall thickness and its standard deviation were calculated within each tap density lot. These are shown in Fig. 10, demonstrating the trend toward increasing average wall thickness with increasing tap density.

### *3.3 Compression of single CMBs*

The data collected from the compression curves of individual CMBs were tabulated for each tap density. Averages and standard deviations were calculated for failure load, pseudo-stiffness, and work of fracture for each of the three categories of CMB. Table I provides a comparison of these properties. Figure 11 provides clarification for the sub-categories, showing the initial and ultimate properties in the schematic. Some explanation is required for the case of the ultimate fracture energy. As with the single

walled CMBs, this is calculated as the area under the load-displacement curve, except that the curve for a nested CMB proceeds in a discontinuous fashion, with at least two regions where the indenter tip is merely traveling downward until it meets a subsequent internal compartment. Assuming that the initial compartment is structurally connected to internal compartments for the majority of nested CMBs and all compartments begin loading concurrently, the work of fracture ( $W_f$ ) is calculated as the sum of an initial triangular area and the subsequent trapezoidal regions.

Since trends beyond average properties were expected, several of the compressive properties have been plotted against CMB size and one another, with the relevant graphs presented in the figures that follow. The diameter vs. work of fracture curve exhibited low  $R^2$  values in the regression analysis, but when plotted co-axially with estimated fracture energies calculated from experimental load and CMB diameter using Equation 5, reasonable agreement between the calculated and fitted curves was observed [9]. Then, it was apparent that the trend in Fig. 12 was of some significance despite the minimal dependence on CMB diameter. Equation 5 was also used to calculate predicted effective wall thickness, using measured work of fracture (Fig. 13). One of the two other trends that became apparent was that of compressive strain vs. diameter, shown in Fig. 14. This trend is evident across all CMB tap densities tested. Figure 15 shows failure load vs. pseudo-stiffness, with a linear fit for each tap density yielding improved correlation.

#### 4. Discussion

Preliminary testing of this foam material has shown that, at constant volume fraction, increasing the tap density of the constituent CMBs did improve the overall

compressive strength and modulus of the composite foam [10]. It was expected that this trend would continue in the CMBs themselves, with higher tap densities displaying greater load bearing ability, as well as increased stiffness. Additionally, CMB size was expected to affect failure loads. However, due to extreme irregularity in the microballoons and the inability to determine actual wall thickness of the individual MB tested, failure stresses for the CMB could not be determined; thus, with the trend of CMB diameter vs. failure load proving tenuous, average failure loads must suffice as a measure of CMB strength. To a small degree, the evidence in Table I regarding single-walled microballoons does support the hypothesis of better CMB properties with increasing tap density. However, although the average load at failure, with values of 11.4, 12.9, and 14.6 mN for the 0.143, 0.161, and 0.177 g/cm<sup>3</sup> CMBs, respectively, does display a positive correlation with tap density, the overlap in the data prevents the relationship from being statistically significant on a 95 % confidence level. Pseudo-stiffness also exhibited increasing average values with increasing tap density. In this case, the 0.143 and 0.161 g/cm<sup>3</sup> tap densities are both statistically different from the 0.177 g/cm<sup>3</sup> CMBs, although they themselves will not pass a t-test as different populations. Unfortunately, the average work of fracture values, which also show general increases with increasing tap density, cannot be shown to be of statistically significant difference at the 95 % confidence level. Thus far, the average property data have only demonstrated that there are small differences in properties with tap density, most of which cannot be statistically verified. When the flawed-single-walled and nested CMB data in Table I are analyzed, it quickly becomes apparent that these types of CMBs follow the same trends as do the single-walled CMBs, with the noted exception that nested CMBs have significantly lower

average failure loads and pseudo-stiffnesses. Doubtless this inferiority was due to the much higher incidence of thin regions and other flaws in their walls, as can be easily observed in Figs. 2 and 7. Further investigation into the average properties of the flawed-single-walled CMBs and nested CMBs showed that the tap densities could not be proved to be statistically separate in any average property category except pseudo-stiffness, which showed the same differentiation between the lowest two tap densities and the highest tap density that was exhibited by the single walled CMBs.

Figure 12 shows one of the least viable trends, work of fracture vs. diameter for single-walled CMBs. In this figure, the bold lines represent the experimental data and the thin lines show the calculated work of fracture, from Equation 5 using measured failure load, diameter, and average wall thickness. Even though the experimental curves have poor fit coefficients, this correlation well represented the average behavior of a CMB of a particular diameter and, as can be seen by the parity in the experimental and calculated curves, is accurately predicted by the theoretical model for a spherical shell under a concentrated uniaxial compressive load. In order to obtain the predicted values, we assumed point contact in the use of the tabulated numerical coefficient (A), and it would yield better agreement with the experimental data if the contact area of the concentrated load were allowed to become a small area of radius less than 5  $\mu\text{m}$ . However, since the actual contact area is unknown and would vary with both CMB wall thickness and diameter, only the simplest case has been presented in Fig. 12. Despite this simplification, the predicted fracture energy agrees so well with the experimental that the two trend curves actually overlap for the 0.161  $\text{g}/\text{cm}^3$  tap density. Given that in the model we used actual load and diameter in addition to the average wall thickness of the CMBs

in a particular tap density, this agreement between the theoretical and experimental data provides evidence related to the cause of the variation in experimentally observed fracture energies. The experimental trend line represents the average behavior of all of the CMBs tested in compression; since this trend followed the theoretical behavior of a CMB having the average wall thickness of that tap density, it is thought that wall thickness variations above or below the average used in the model are the cause of the wide scatter in the experimental data. Thus, the theoretical model could be used to predict an accurate and valid average work of fracture for a particular tap density CMB, having measured average load, diameter, and wall thickness. Conversely, the effective thickness of a CMB with measured load, diameter, and work of fracture could be predicted by the model, as in Fig. 13.

Figure 14 shows compressive strain at failure of the single-walled CMBs is proportional to the inverse square root of CMB diameter, a trend that has been observed in the three tap density CMBs tested in this study, and in other CMBs previously tested [5]. Given the trend lines, it is concluded that it is valid for all single-walled CMBs and is essentially independent of tap density. Comparison with research on glass microballoons reveals that this trend may be unique to CMBs, since it has not been observed in other systems [4, 11]. The fact that there is no observed trend in wall thickness with CMB diameter (Fig. 9) means that small and large CMBs have similar wall thicknesses; and hence, the small CMBs contain less volume of carbon in their walls. This reduction in available carbon wall material in smaller diameter CMBs is speculated to limit the maximum flaw size in the CMB, as shown in Fig. 16. The classic argument for a brittle material following Weibull statistics means that there is a reduced probability of finding a

critical flaw size in a smaller CMB due to its lesser volume. This, when applied to the compressive strain results, explains the failure of smaller diameter CMBs at higher strains (and hence greater strengths). Additionally, the location, relative to the compression platens, of a flaw like that depicted in Fig. 16 is expected to affect the compressive strengths of the CMBs. However, since flaw location is unknown experimentally, the exact effect on the compressive data cannot be determined.

Figure 10 shows the general increase in average wall thickness with tap density. Here, the  $0.143 \text{ g/cm}^3$  CMBs and the  $0.161 \text{ g/cm}^3$  CMBs cannot be considered to be statistically different populations at the 95% confidence level, but the  $0.177 \text{ g/cm}^3$  tap density average thickness tested as significantly different at the same significance level. Recall that average pseudo-stiffness for single-walled CMBs also showed little difference between the lower two tap densities but clearly separated the highest tap density. Now, an overall trend emerges connecting wall thickness and pseudo-stiffness. If a microballoon during compression were considered to be essentially a spring, its  $k$  value would depend on the inherent stiffness of the material and the spring geometry. For a metal coil spring, this would be the coil size, wire diameter, and wire cross-section. For a microballoon, the important geometrical parameters are diameter ( $\phi$ ) and wall thickness ( $t$ ). The higher average thickness results in greater stiffness for the  $0.177 \text{ g/cm}^3$  tap density. Further evidence of the effect of thickness on mechanical properties is observed in Fig. 15. It shows that, for a given tap density, CMBs of higher stiffness also possessed greater failure loads. Additionally, inter-tap density comparison showed that the highest tap density had a clearly greater stiffness at any given load, as expected given its higher wall thickness. This emphasis on wall thickness controlling failure properties corresponds well

to previous studies. Bratt et al. [11] showed that the uniaxial compressive failure load of a glass microballoon was independent of its diameter and related only to the average strength and wall thickness squared of the MB, a similar result to that seen in Fig. 13 relating CMB failure load to predicted wall thickness. Their exclusive focus on GMBs, where the wall thickness and single-walled nature of each GMB were determined by means of an interference microscope prior to testing, prohibits further comparison to the CMB work presented here, due to the opaque nature of the CMBs.

## 5. Conclusions

Through the novel use of a modified nanoindenter, in this work we have tested carbon microballoons of three different ASTM B527 tap densities in uniaxial compression. Optical and scanning electron microscopy of these CMBs has shown the existence of several morphologies, including single-walled and nested CMBs. Additionally, microscopic techniques have proven that the highest tap density possessed thicker walls than the other two tap density CMBs.

A statistical approach to the data presented several trends. Compressive strain was proportional to the inverse square root of diameter for all tap densities; failure load was seen to correlate linearly with stiffness; and fracture energy was observed to have some small dependence on diameter that was readily predictable via theoretical formulas. Average failure load, fracture energy, and pseudo-stiffness from the CMBs showed increases with increasing tap density, although these differences were not always statistically significant. Additionally, single-walled CMBs exhibited superior average failure loads, fracture energies, and pseudo-stiffnesses than nested CMBs. Although the

correlation between wall thickness and tap density did elucidate most of the trend toward increasing mechanical properties, research into other possible explanations is still ongoing.

## 6. Acknowledgments

This work was financially supported by Los Alamos National Laboratory/DOE subcontract #44277-SOL—02 4X. LA-UR 04-8377. K. B. Carlisle is grateful to the Department of Defense for a National Defense Science and Engineering Graduate Fellowship.

## 7. References

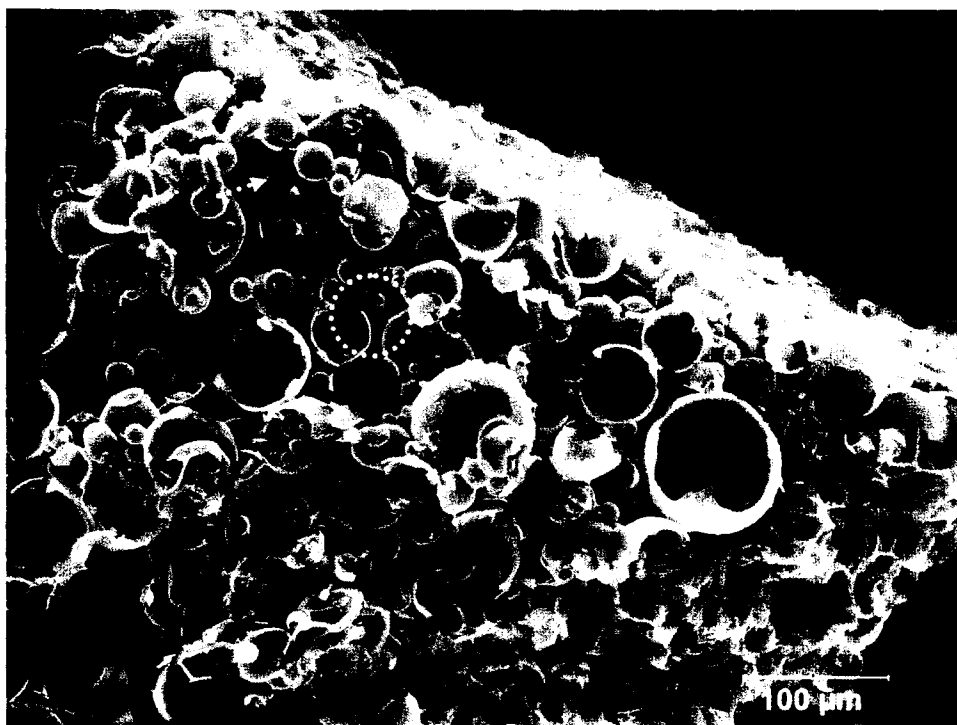
1. K. OKUNO and R.R. WOODHAMS, *Cellular Plastics* **10** (1973) 237.
2. H.S. KIM and H.H. OH, *Journal of Applied Polymer Science* **76** (2000) 1324.
3. G. GLADYSZ and K.K. CHAWLA, Composite Foams, in "Encyclopedia of Polymer Science & Technology" (John Wiley, New York, 2004) pp. 267-281.
4. M. KOOPMAN, G. GOUADEC, K. CARLISLE, K.K. CHAWLA, and G. GLADYSZ, *Scripta Materialia* **50** (2004) 593.
5. K. CARLISLE, K.K. CHAWLA, G. GOUADEC, M. KOOPMAN, and G.M. GLADYSZ, Nanocompressive properties of carbon microballoons and mechanical properties of carbon based syntactic foam composites, in Proceedings of ICCM-14, San Diego, CA, July 2003 (Society of Manufacturing Engineers, 2003).
6. ASTM D 3102-78: Standard Practice for the Determination of Isostatic Collapse Strength of Hollow Glass Microspheres, in "Annual Book of ASTM Standards" (American Society for Testing and Materials, 1984).
7. K. CARLISLE, K.K. CHAWLA, G. GLADYSZ, and M. KOOPMAN, *J. Mater. Sci.* **41** (2006) 3961.

8. E.E. UNDERWOOD, Surface Area and Length in Volume, in "Quantitative Microscopy", R.T. Dehoff and F.N. Rhines, eds. (McGraw-Hill, New York, 1968) pp. 96-97.
9. R.J. ROARK, in "Roark's Formulas for Stress and Strain", ed. W.C. Young (McGraw-Hill, New York, 1989) pp. 542-547.
10. G.M. GLADYSZ, B. PERRY, G. MCEACHEN, and J. LULA, *J. Mater. Sci.* **41** (2006) 4085.
11. P.W. BRATT, J.P. CUNNION, and B.D. SPIVAK, Mechanical Testing of Glass Hollow Microspheres, in "Advances in Materials Characterization", D.R. Rossington, R.A. Condrate, and R.L. Snyder, eds. (Plenum Press, New York, 1983) pp. 441-447.

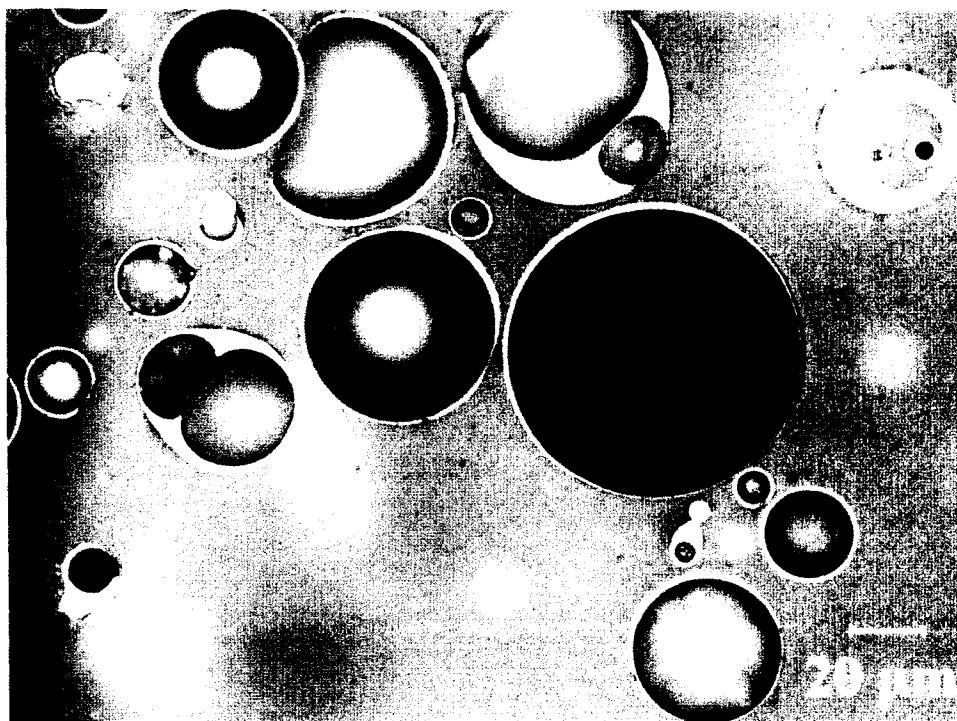
## 8. Illustrations

TABLE I: Average Properties of CMBs by Category.

CMB Category	SW			FSW			N		
Tap Density (g/cm <sup>3</sup> )	0.143	0.161	0.177	0.143	0.161	0.177	0.143	0.161	0.177
$P_{f \text{ ultimate}}$ (mN)	11.4	12.9	14.6	11.6	11.3	10.9	8.0	10.7	12.8
$P_{f \text{ initial}}$ (mN)		NA			NA		2.7	3.1	3.9
$W_{f \text{ total}}$ (nJ)	22.2	29.6	27.5	37.3	29.9	35.2	23.4	19.9	24.1
$W_{f \text{ initial}}$ (nJ)		NA			NA		6.3	5.4	8.2
$k_{\text{ average}}$ (kN/m)	3.5	3.6	4.7	2.1	2.6	2.0	1.9	3.1	3.5
$k_{\text{ initial}}$ (kN/m)		NA			NA		0.8	1.2	1.1



*Figure 1* Micrograph of 3-phase carbon microballoon (CMB) syntactic foam. SEM. Circle indicates intra-microballoon void region, and arrow points to APO-BMI between CMB.



*Figure 2* Polished cross-section of CMB mounted in epoxy. Image used for wall thickness measurements.

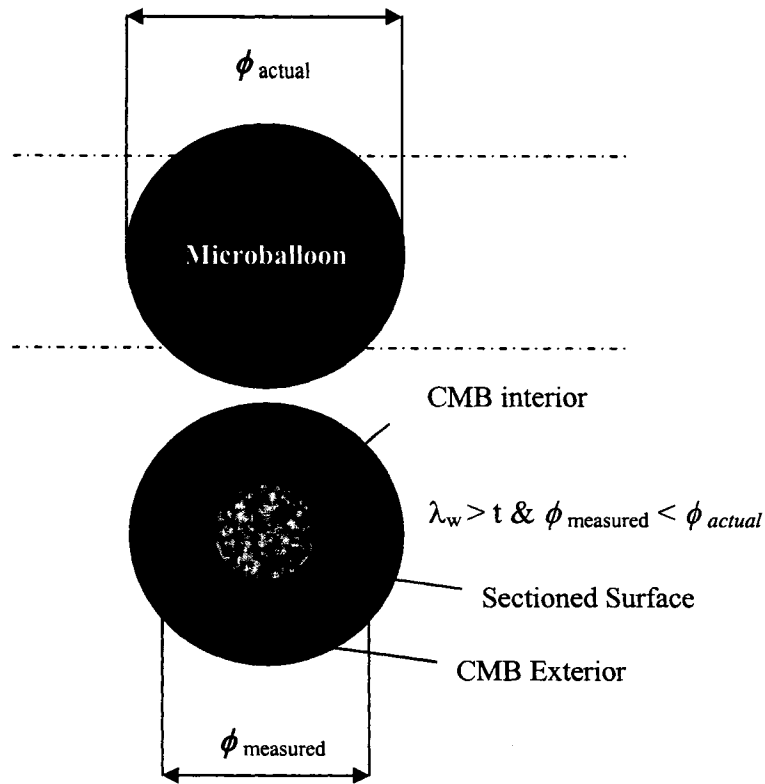


*Figure 3* Schematic illustrating sectioning a CMB either below or above its great circle (dashed lines). Note that measurements made on the section will be inaccurate due to the curvature of the CMB.

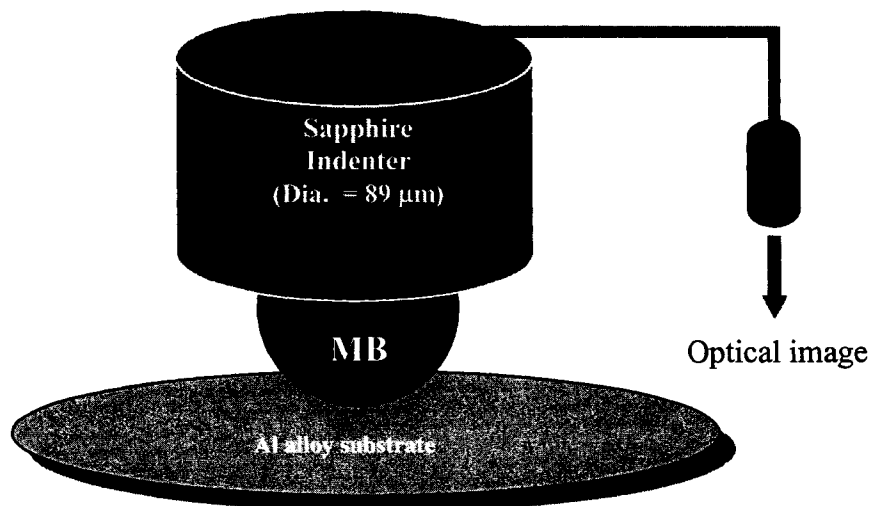


*Figure 4* Schematic of nanoindenter modified for use in compression testing of CMB. Cylinder at right represents attached optical microscope.

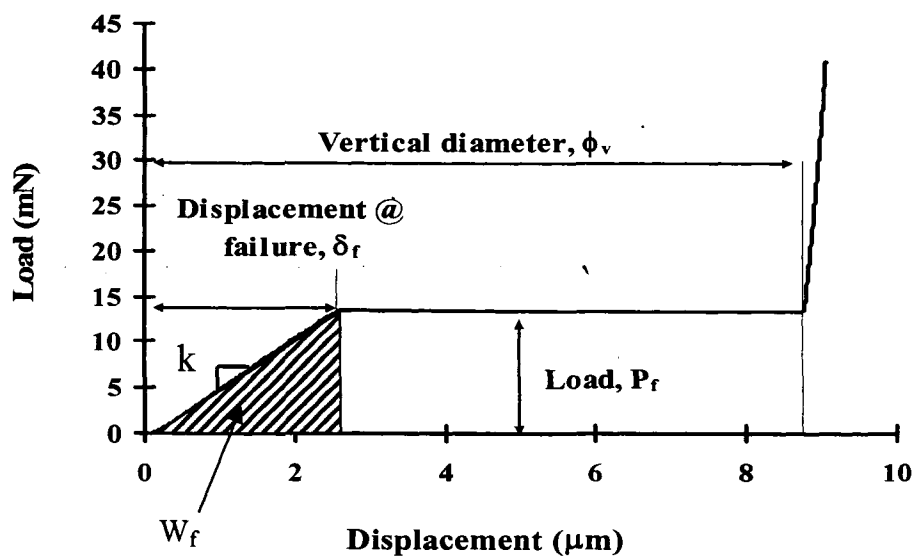


*Figure 5* Sample compression curve for a single wall CMB, showing parameters extracted from graph.

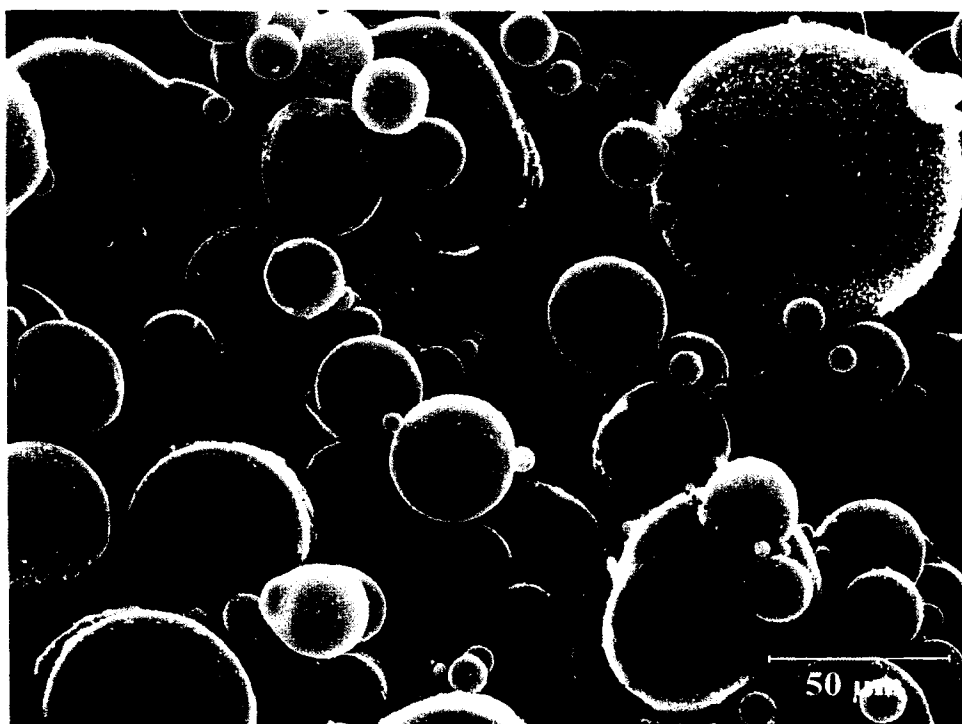


*Figure 6* Micrograph showing variation in CMB size and morphology. Broken (arrow) and conjoined (circle) CMBs visible. SEM.

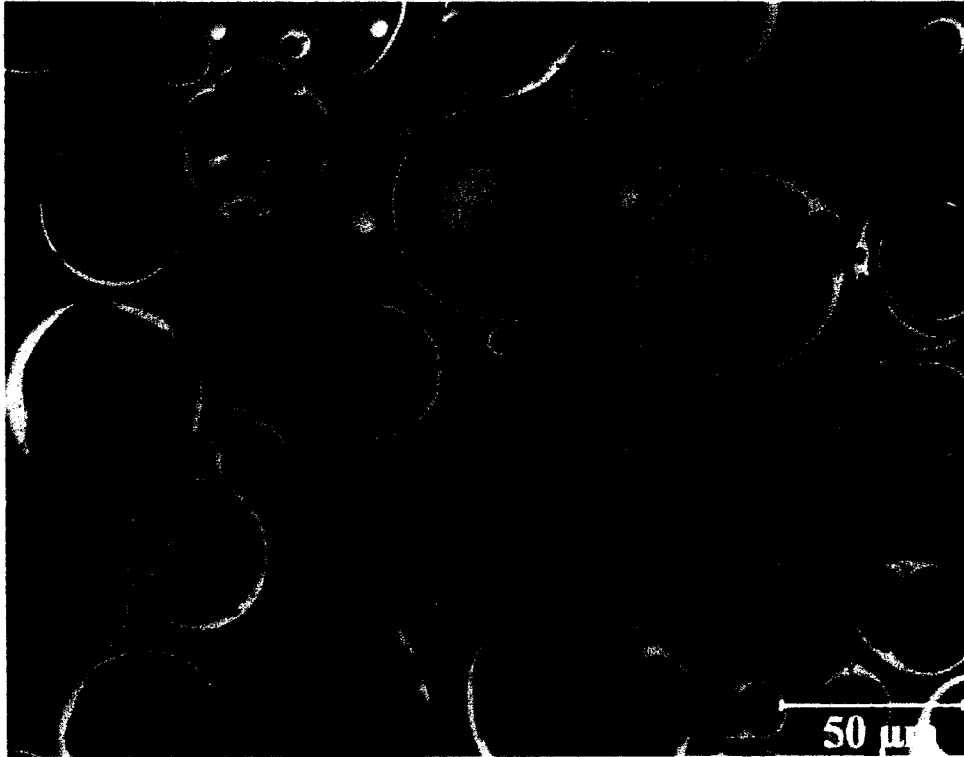


*Figure 7* Polished cross-section of CMB foam. Note the interior compartments, wall thickness imperfections, etc.

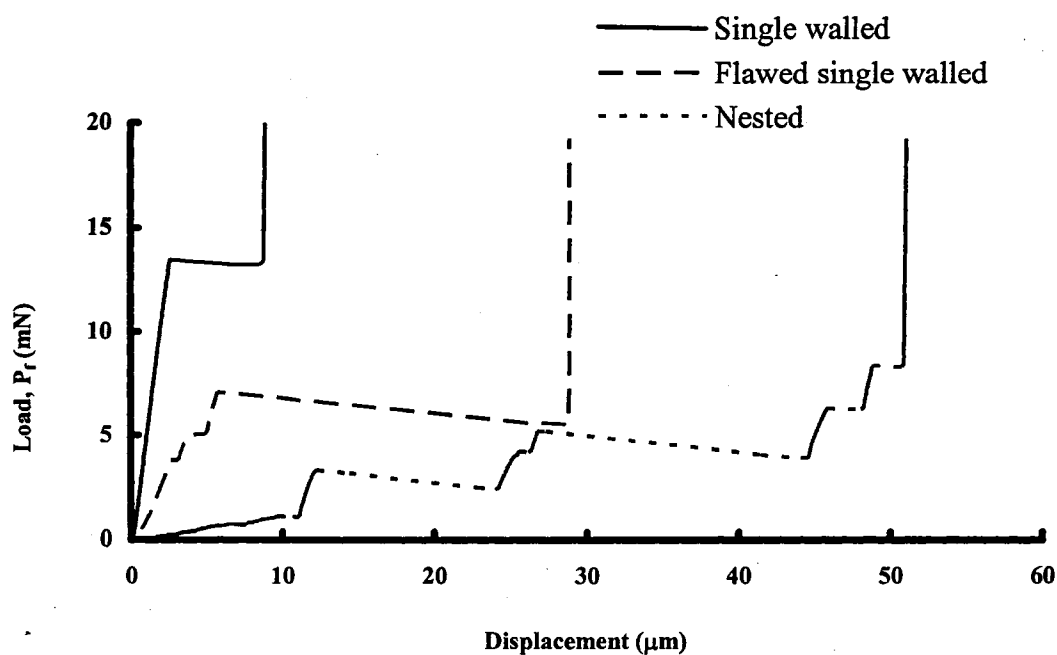


Figure 8. Examples of different CMB compressive behavior based on CMB morphology [5].

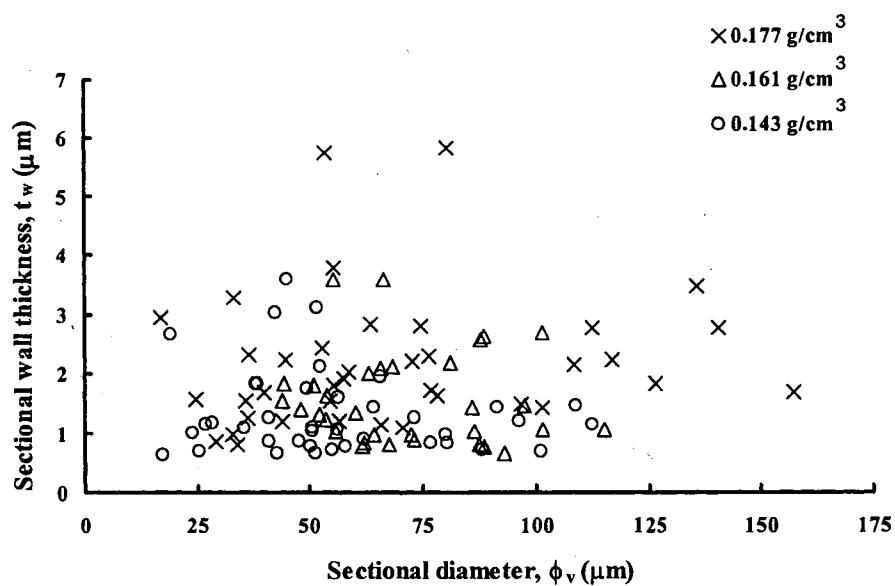


Figure 9 CMB diameter vs. wall thickness. (sectional values) No observable correlation.

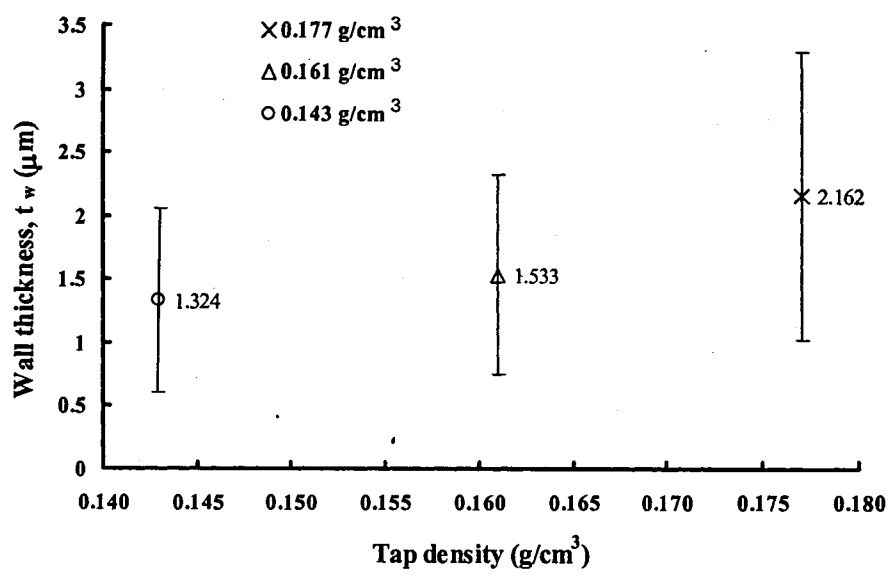


Figure 10 Calculated average CMB wall thickness vs. tap density. Trend toward increasing average wall thickness with higher tap density is apparent.

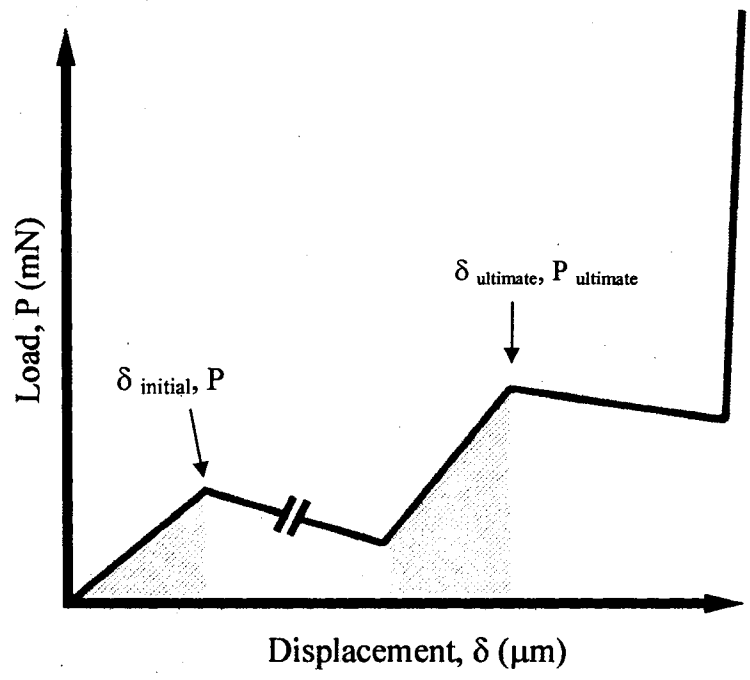
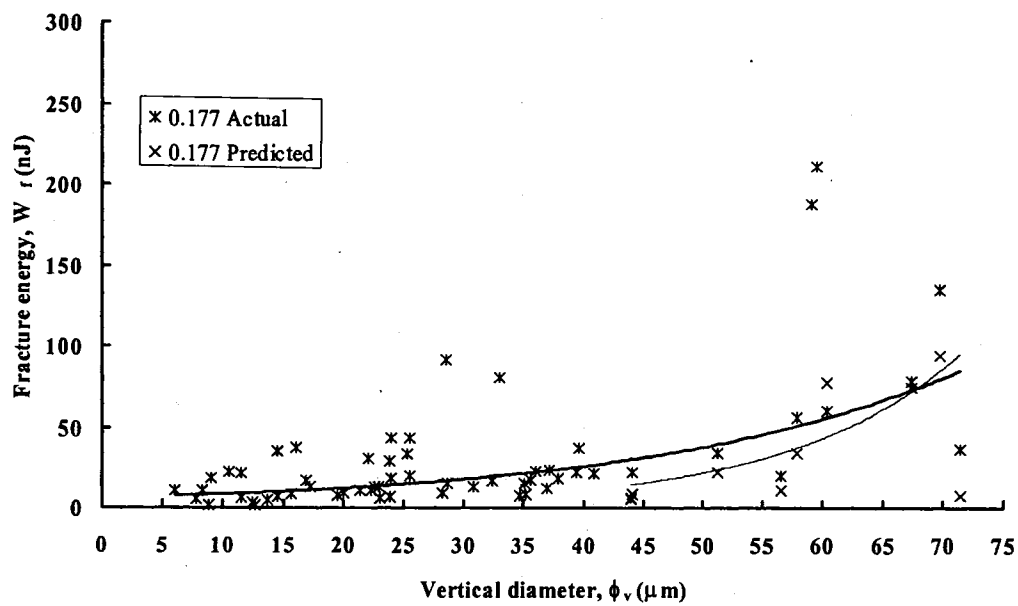
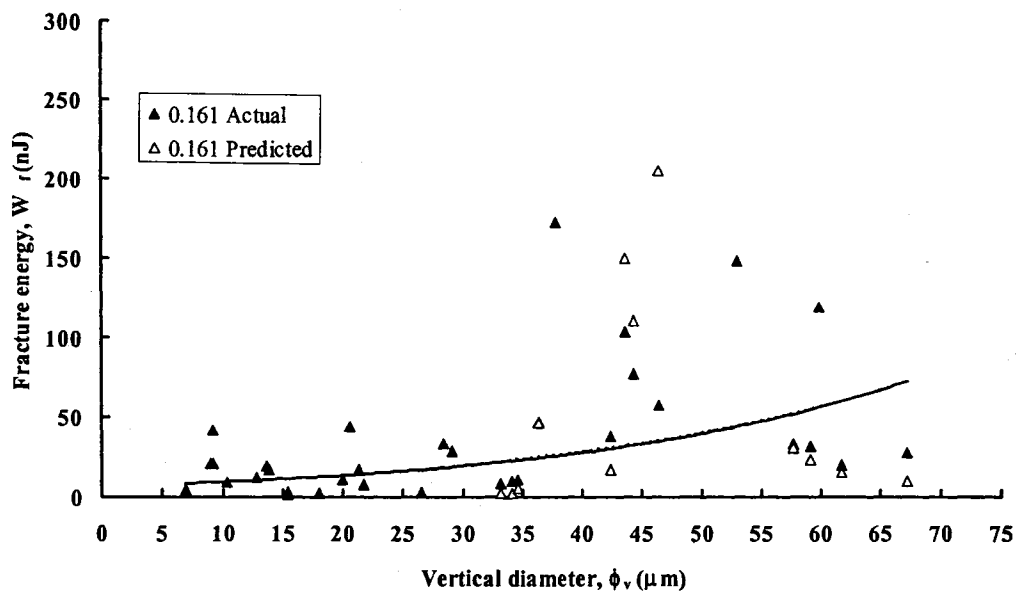


Figure 11 Schematic representation of nested compression curve, with initial and ultimate properties labeled. The gray shading represents the work of fracture for a nested CMB.

(a)



(b)



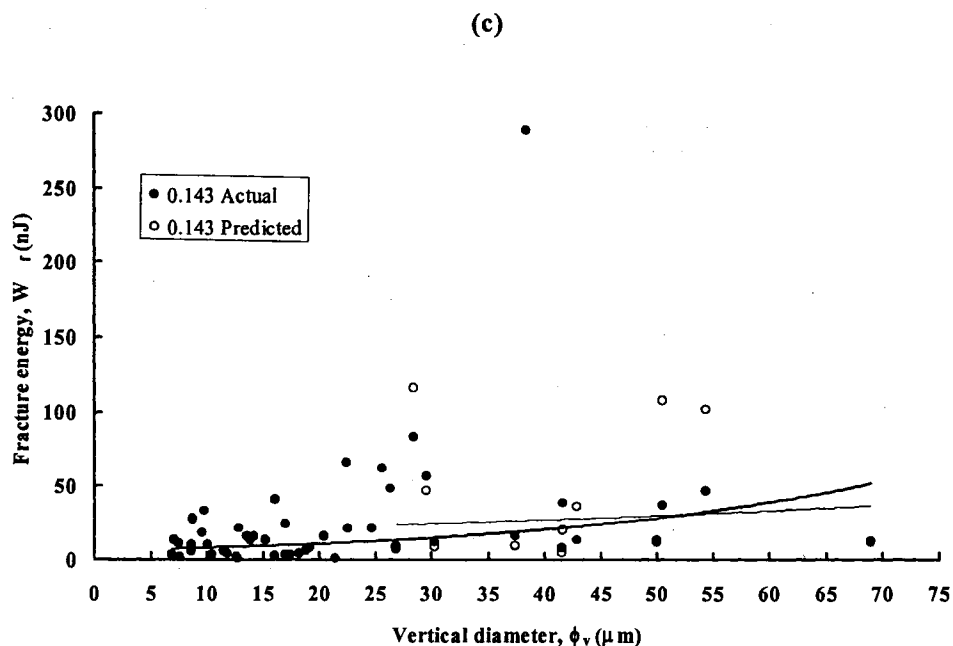


*Figure 12* Fracture energy vs. diameter for single wall CMBs, with bold lines for experimental and thin lines for calculated trends. Units in the inset are  $\text{g/cm}^3$ . Experimental curves are shown only in the region where  $R/t > 10$  and Equation 5 applies. (a)  $0.177 \text{ g/cm}^3$  tap density CMBs. (b)  $0.161 \text{ g/cm}^3$  CMBs. Experimental and theoretical curves overlap in the figure. (c)  $0.143 \text{ g/cm}^3$  CMBs.

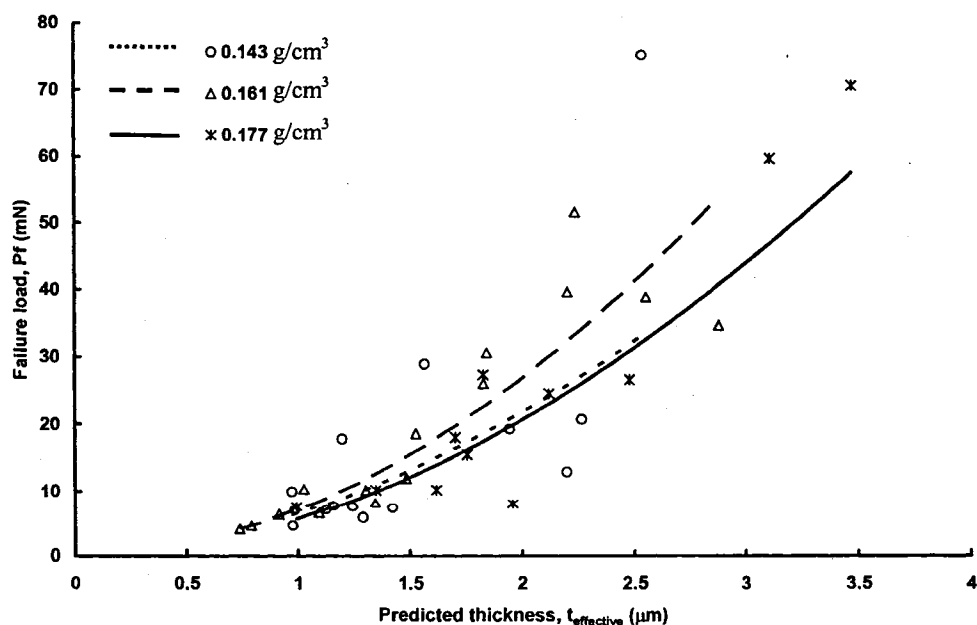


*Figure 13* Failure load vs. predicted thickness for single walled CMBs, revealing a parabolic dependence of failure load on thickness.

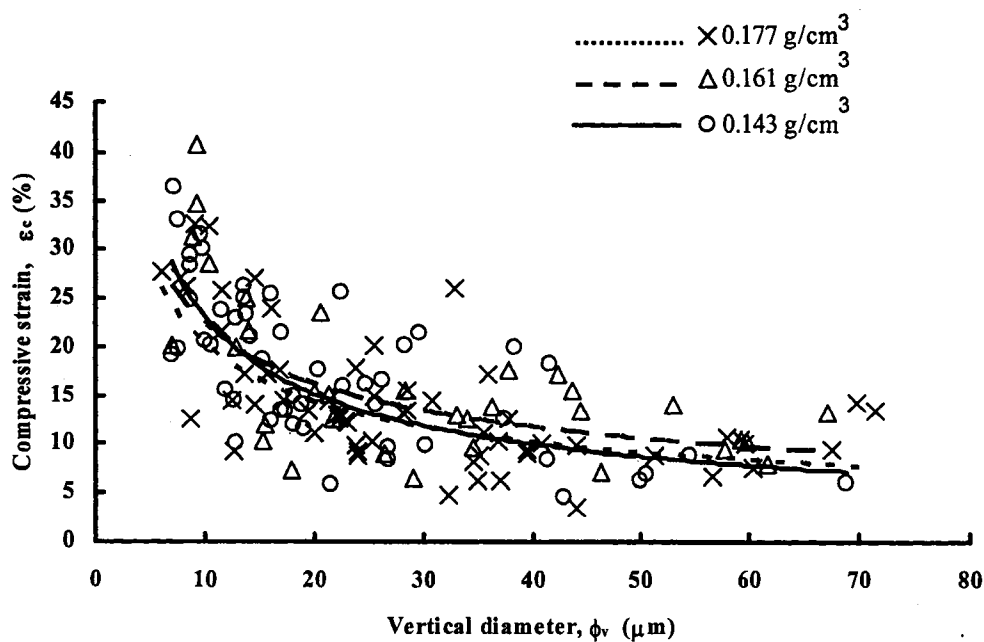


Figure 14 Compressive strain trend for single wall CMBs. Trend appears similar for all tap densities.

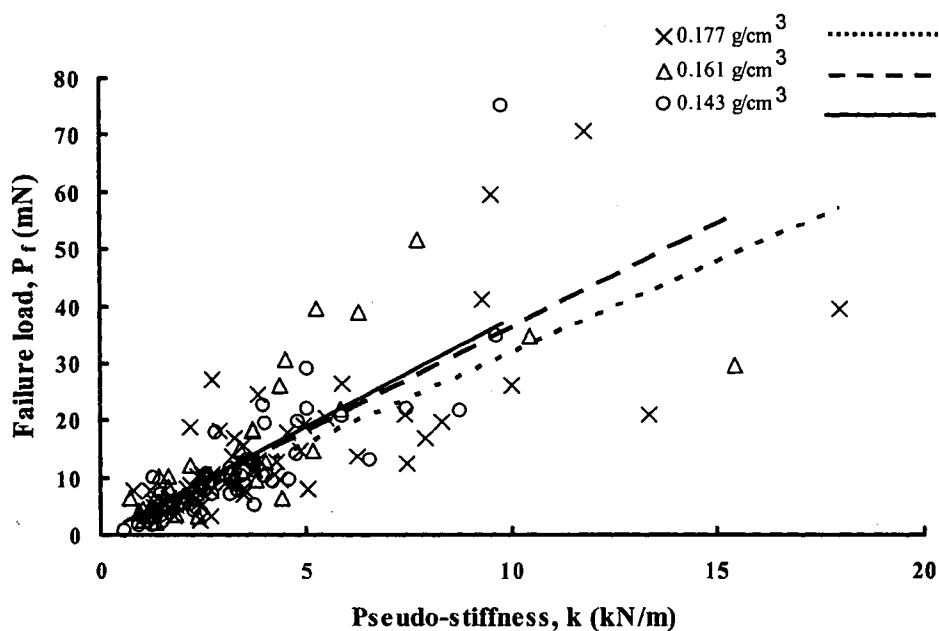
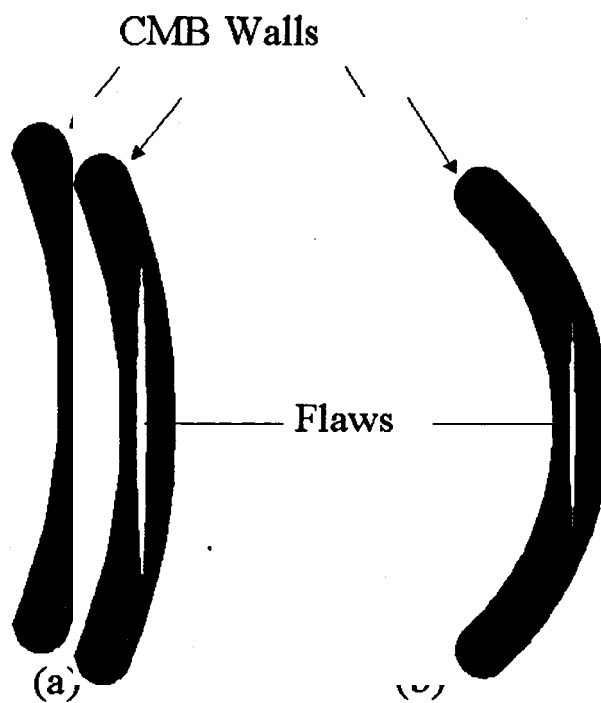


Figure 15 Load vs. pseudo-stiffness trend for all tap density single wall CMB.



*Figure 16* Schematic of speculated flaw size limitations in smaller diameter CMBs. CMBs in (a) and (b) are of identical thickness, with shell (a) having twice the diameter of (b). The smaller maximum flaw size for the smaller CMB is clearly shown.

UNIAXIAL COMPRESSIVE PROPERTIES OF BISMALEAMID-COATED CARBON  
MICROBALLOONS

by

K. B. CARLISLE, K.K. CHAWLA, M. KOOPMAN, G.M. GLADYSZ, M. LEWIS

Submitted to *Journal of Cellular Plastics*

Format adapted for dissertation

## Abstract

A uniaxial compression technique employing a nanoindenter equipped with a flat-ended cylindrical tip was used to evaluate the performance of carbon microballoons (CMBs) precipitation-coated with a bismaleamid (APO-BMI) polymer. This coating would eliminate the size and density induced segregation of APO-BMI and CMBs during mold filling and the potentially damaging mixing step wherein CMBs and powdered binder pre-polymer are blended prior to foam molding. To augment the molding of syntactic foams directly from coated CMBs and to aid in the development of a constitutive model for a three-phase syntactic foam, mechanical property evaluation of the coated CMBs was needed. Cured, APO-BMI coated and uncoated CMBs (0.192 g/cm<sup>3</sup> tap density) were compressed uniaxially using a modified nanoindenter to obtain the compressive properties of the CMBs in both conditions. These properties included strain-to-failure, failure load, displacement-at-failure, and work of fracture. The 0.192 g/cm<sup>3</sup> tap density CMBs' behavior followed the prior inter-tap density trends between compressive strain and diameter and failure load vs. stiffness. The coating was determined to have no statistically significant effect on the mechanical properties of the CMBs. From the combination of this information, the effect of an APO-BMI coating on CMBs of any tap density was inferred.

## 1. Introduction

Manufacturing difficulties in syntactic foam production can result in poor-quality foams in a variety of ways. For three-phase syntactic foams, most of these difficulties stem from the attempt to uniformly distribute the binder throughout the foam. This is usually performed via a mechanical mixing of the powdered binder with the microballoons (MBs). The agitation of this mixing can lead to an excessive number of broken MBs if it is too violent or if the MBs are brittle [1-4]. At low binder volume fractions, a second problem is the uneven distribution of the binder in the foam, which is often compounded by the tendency of the binder powder and the MBs to segregate during mold filling. These difficulties can be eliminated by removing the mixing step in the production process; one possible solution is to coat the MBs with the uncured binder. Then, a syntactic foam may be produced simply by filling the mold with coated MBs and curing the binder coating [1, 2].

This pre-polymer coating procedure has been attempted with a three-phase carbon microballoon (CMB) syntactic foam, using one ASTM B527 tap density batch of CMBs as a test bed for the new processing technique. CMBs ( $0.192 \text{ g/cm}^3$  tap density) were coated in uncured APO-BMI binder, and three-phase syntactic foams were molded from these coated CMBs. Since a three-phase syntactic foam can be conceptualized as a collection of single MBs coated in cured binder and held together by binder ligaments at the MB contact points, determination of the mechanical properties of coated CMBs provides valuable future constitutive modeling data on individual unit cells of these foams, while evaluating the performance of the coating. To evaluate the effect of the coating on the mechanical properties of the coated and uncoated CMBs, a previously

published technique was adopted, whereby the uniaxial compressive properties of single CMBs were investigated by using a modified nanoindenter [5-8]. The available properties from this technique include stiffness, load, displacement, strain, and work of fracture. After curing of the coating, APO-BMI-coated CMBs were compressed in the nanoindenter, and their compressive properties were determined. Uncoated CMBs were also evaluated, providing a control sample for comparison to both the coated samples and to the other tap densities previously tested [6]. The results of this comparison provide insight into the behavior of CMBs during compression of a three-phase syntactic foam and could be used to justify some decisions in the design of constitutive models for these materials.

## 2. Experimental Procedure

Three batches of CMBs ( $0.192 \text{ g/cm}^3$  tap density, per ASTM B 527 [9]) were tested in uniaxial compression, using a technique previously described [6]. As before, several engineering parameters were extracted from the compression curve, as shown in Fig. 1. The diameter ( $\phi_v$ ) of each CMB was found as the difference between the platen displacement at substrate contact, after the CMB was crushed, and the platen displacement at the start of loading. The linear slope of the loading segment, from initial platen-MB contact until the CMB shattered, is termed the pseudo-stiffness ( $k$ ). The load at failure ( $P_f$ ) is the maximum of the linear loading segment. The platen displacement from initial contact until CMB failure is the displacement at failure ( $\delta_f$ ), which was divided by  $\phi_v$  to yield compressive strain at failure ( $\epsilon_c$ ). The three test conditions were: an uncoated condition (UC), an APO-BMI coated, single-step (200 °C) cured population

(CC200), and an APO-BMI coated, step-wise cured condition (CC210) that had curing hold segments at 150 and 210 °C. These curing steps and temperatures were based on the curing cycle for the APO-BMI in the production of the foams, and on APO-BMI characterization work, detailed elsewhere [10, 11]. Samples from each of the cured conditions, CC200 and CC210, were heated in an oven on the Al stub that would be used as the lower platen in the compression test. The cure temperature was monitored by an independent thermocouple. The uniaxial compressive behavior for at least 140 CMBs from each of these conditions was obtained using the same modified nanoindenter procedure as previously described [8], and average properties were computed.

To determine the effect of the APO-BMI on the compressive properties of the syntactic foams, confined uniaxial compression was performed on bulk uncoated CMBs and on right circular cylinders of three-phase CMB syntactic foam. The bulk CMBs were settled in a confined compression fixture as per the settling procedure described in the tap density standard (ASTM B 527). The dimensions of the foam samples were 24.94 mm diameter and 25.4 mm height for all samples. Tests were conducted on similar volumes of material in both cases. Tests were arbitrarily terminated after reaching at least 15 percent strain.

### 3. Results and Discussion

In order to generalize the behavior of the 0.192 g/cm<sup>3</sup> tap density CMBs to other densities, it was first necessary to compare the behavior of the UC 0.192 g/cm<sup>3</sup> tap density CMBs to trends previously observed in other tap densities [5-7]. As can be seen in Fig. 2, the average failure load and pseudo-stiffnesses, 22.73 mN and 7.14 kN/m, of

this tap density were higher than those of the three lower tap densities, validating the trend toward increasing average properties with increasing tap density. As before, this is likely due to the trend toward increasing average wall thickness with tap density. Figures 2 and 3 show the main intra-tap density trends observed previously [5, 6], with the UC 0.192 g/cm<sup>3</sup> tap density data plotted alongside. As expected, compressive strain at failure was again nearly proportional to the inverse square root of CMB diameter, regardless of tap density, see Fig. 3. CMB failure load was linearly related to pseudo-stiffness for all tap densities, as shown in Fig. 4. As expected in this plot, the highest tap density had the lowest trendline slope, indicating an increase in stiffness as tap density increased, at a fixed failure load. We can conclude that the 0.192 g/cm<sup>3</sup> tap density CMBs were representative samples of CMBs, and therefore any conclusions reached about the effect of an APO-BMI coating on their surfaces may be extended to other tap densities.

Once the UC 0.192 g/cm<sup>3</sup> tap density CMBs was determined to be representative of the general CMB behavior, the evaluation of the two lots coated in cured APO-BMI commenced. SEM micrographs of the cured, coated CMBs showed adequate coating coverage and contiguity, see Fig. 5. As evidenced by the bonding of the two CMBs together in Fig. 5a, the APO-BMI layer was relatively uniform, although Fig. 5b shows evidence of APO-BMI pooling during curing—see the large circular formation of APO-BMI that was beneath a CMB on the Al stub after curing. SEM was also used to attempt to evaluate the coating thickness, but unfortunately the resolution limits of the Philips SEM prevented detection of what was apparently a sub-micrometer coating thickness of APO-BMI on the CMB wall fragments, as seen in Fig. 6. After evaluating the coating morphology, the compressive behavior of these CMB lots was studied. The averages and

standard deviations of the compressive properties for each of the three conditions are shown in Table 1. A comparison of the data shows there was no measurable statistical difference (via analysis of variance) in the coated vs. the uncoated average properties. The plot of compressive strain at failure vs. CMB diameter in Fig. 7 shows again the inverse square root trend, with the trendline for the UC CMBs totally indistinguishable from those for the CC200 and the CC210 test lots. Finally, Fig. 8 shows a plot of failure load vs. pseudo-stiffness for these populations. The trendlines barely separated from one another in this case; the statistical difference between them was negligible. Thus, within the limitations of the test technique, the APO-BMI coating had no effect on the compressive properties of the  $0.192 \text{ g/cm}^3$  tap density CMBs.

The lack of a quantifiable effect on the compressive properties of these CMBs has larger implications in three-phase syntactic foams. Chiefly, there is now evidence that a sub-micrometer thick coating of APO-BMI on the surfaces of the CMBs has a negligible effect, as previous research has inferred [12]. To use the results of this work in constructing a constitutive model for these three-phase syntactic foams, the effect of the APO-BMI in the foam was elucidated by conducting confined uniaxial compression of both uncoated bulk CMBs and three-phase CMB syntactic foams, see Fig 9a and 9b, respectively. Figure 9 demonstrates that there is a significant difference in the response of bulk CMBs and the foam in confined compression. Since compression of single, APO-BMI-coated CMBs has established that the thin layer of APO-BMI coating the surface of individual CMBs did not have a measurable effect on their compressive behavior, it can be deduced that the confined compression behavior of bulk CMBs, Fig. 9a, would be unaffected by coating as well. We can further infer that the same thin layer of APO-BMI

on the CMB surfaces distributed throughout the foam will have a negligible effect on the compressive contribution of the CMBs. This leaves only one possible source for the difference in Fig. 9a and 9b, which is the APO-BMI ligaments. The APO-BMI necks at CMB to CMB contacts, which bind the CMBs together in the foam, are shown in Fig. 5a between two individual CMBs. Thus, when constructing a constitutive model for this material, one need only model uncoated CMBs bound together at CMB/CMB contacts by APO-BMI ligaments.

#### 4. Conclusions

CMBs ( $0.192 \text{ g/cm}^3$  tap density) were evaluated in three conditions: uncoated, coated with single-step cured APO-BMI, and coated with multi-step cured APO-BMI. The uncoated CMBs were found to follow the trend of increasing average properties with tap density, as expected from prior research [5, 6]. Thus, they were concluded to be a representative tap density of CMBs. Furthermore, both cured APO-BMI coatings had no effect on the compressive properties of the CMBs. Thus, we can conclude that a sub-micrometer thickness, cured APO-BMI coating will not significantly impact the compressive behavior of CMBs of *any* tap density. This final conclusion has broad implications in syntactic foams, where our findings on individual microballoon behavior supports the conclusions drawn from studies of syntactic foams [2, 4, 10, 12]; microballoons are responsible for the greatest percentage of the compressive strength of a three-phase syntactic foam, binder ligaments provide a lesser contribution, and the thin coating of binder on the surface of the microballoons has negligible influence on the compressive properties of the foam.

## 5. Acknowledgments

This work was financially supported by Los Alamos National Laboratory/DOE subcontract #44277-SOL—02 4X. KBC is grateful to the Department of Defense for a National Defense Science and Engineering Graduate Fellowship. LA-UR-06-6129.

## 6. References

1. M. NARKIS, M. GERCHCOVICH, M. PUTERMAN, and S. KENIG, *Journal of Cellular Plastics* **18** (1982) 230.
2. M. NARKIS, S. KENIG, and M. PUTERMAN, *Polymer Composites* **5** (1984) 159.
3. M. NARKIS, M. PUTERMAN, H. BONEH, and S. KENIG, *Polymer Engineering and Science* **22** (1982) 417.
4. M. NARKIS, M. PUTERMAN, and S. KENIG, *Journal of Cellular Plastics* **16** (1980) 326.
5. K. CARLISLE, K.K. CHAWLA, G. GOUADEC, M. KOOPMAN, and G.M. GLADYSZ, Nanocompressive properties of carbon microballoons and mechanical properties of carbon based syntactic foam composites, in Proceedings of ICCM-14, San Diego, CA, July 2003 (Society of Manufacturing Engineers, 2003).
6. K.B. CARLISLE, M.C. KOOPMAN, K.K. CHAWLA, R.K. KULKARNI, G.M. GLADYSZ, and M. LEWIS, *J. Mater. Sci.* **41** (2006) 3987.
7. G. GOUADEC, K. CARLISLE, K.K. CHAWLA, M.C. KOOPMAN, G.M. GLADYSZ, and M. LEWIS, Nano-compression of carbon micro-balloons with a flat-ended cylindrical indenter, in Proceedings of Indentation Techniques in Ceramic Materials Characterization, Apr 27-30 2004, Nashville, TN., United States (American Ceramic Society, 2004). pp. 143-152.
8. M. KOOPMAN, G. GOUADEC, K. CARLISLE, K.K. CHAWLA, and G. GLADYSZ, *Scripta Materialia* **50** (2004) 593.

9. ASTM B 527: Standard Test Method for Determination of Tap Density of Metallic Powders and Compounds, in "Annual Book of ASTM Standards" (American Society for Testing and Materials, 2000).
10. G.M. GLADYSZ, B. PERRY, G. MCEACHEN, and J. LULA, *J. Mater. Sc.* **41** (2006) 4085.
11. G.W. MCEACHEN, Carbon Syntactic Foam Mechanical Properties Testing. Topical Report: KCP-613-6043. (Kansas City) 1998.
12. M. KOOPMAN, K.K. CHAWLA, G. GLADYSZ, and K.B. CARLISLE, *J. Mater. Sci.* **41** (2006) 4009.

## 7. Tables and Figures

TABLE I Average and standard deviation for the compressive properties of 0.192 g/cm<sup>3</sup> tap density CMBs.

Condition	Failure load, $P_f$ (mN)	Failure strain, $\varepsilon_c$ (%)	Work of Fracture, $W_f$ (nJ)	Pseudo-stiffness, $k$ (kN/m)
UC	22.73 ± 20.97	14.38 ± 10.76	42.41 ± 49.01	7.14 ± 6.72
CC200	20.83 ± 19.70	13.44 ± 6.48	41.74 ± 60.79	6.36 ± 4.03
CC210	22.32 ± 18.63	14.45 ± 7.55	39.82 ± 42.10	7.16 ± 5.49

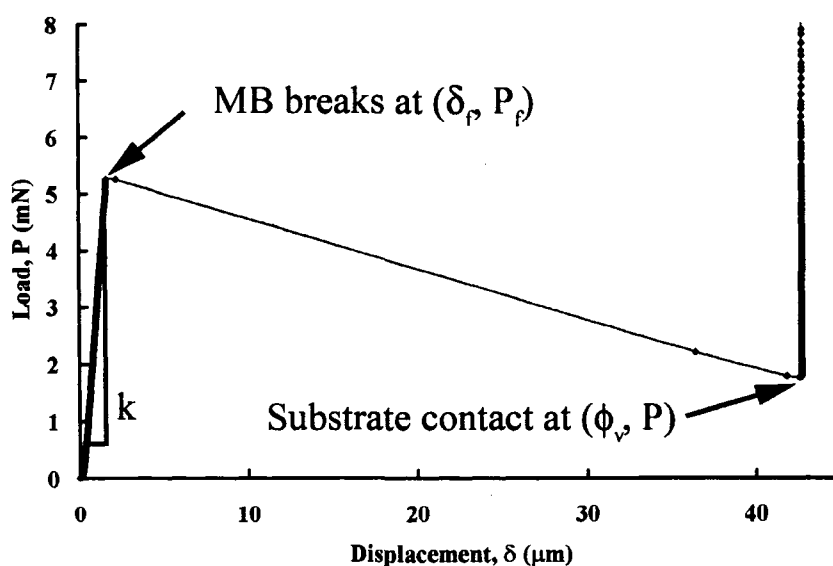


Figure 1 Compression curve for a single CMB. The stiffness of the MB, MB breakage, and substrate contact are labeled on the curve.

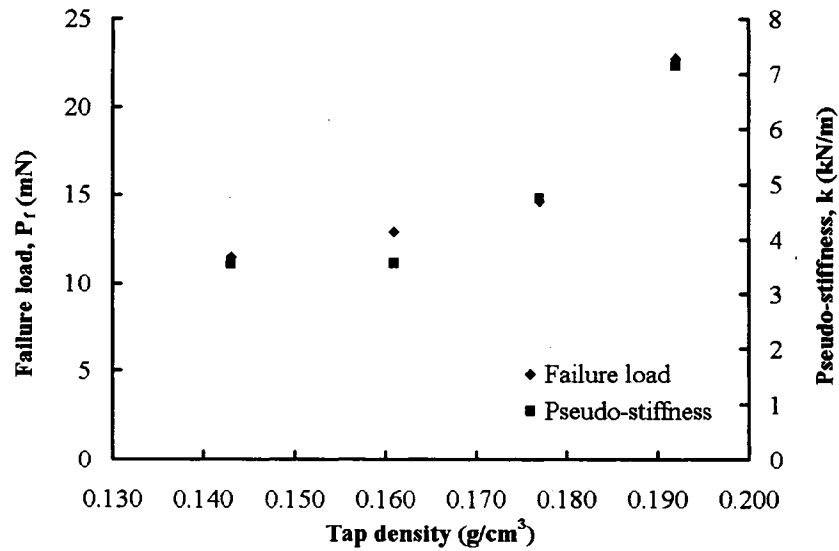


Figure 2 Average property comparison for all four tap densities of CMBs. There is a trend toward increasing average failure load and stiffness with increasing tap density.

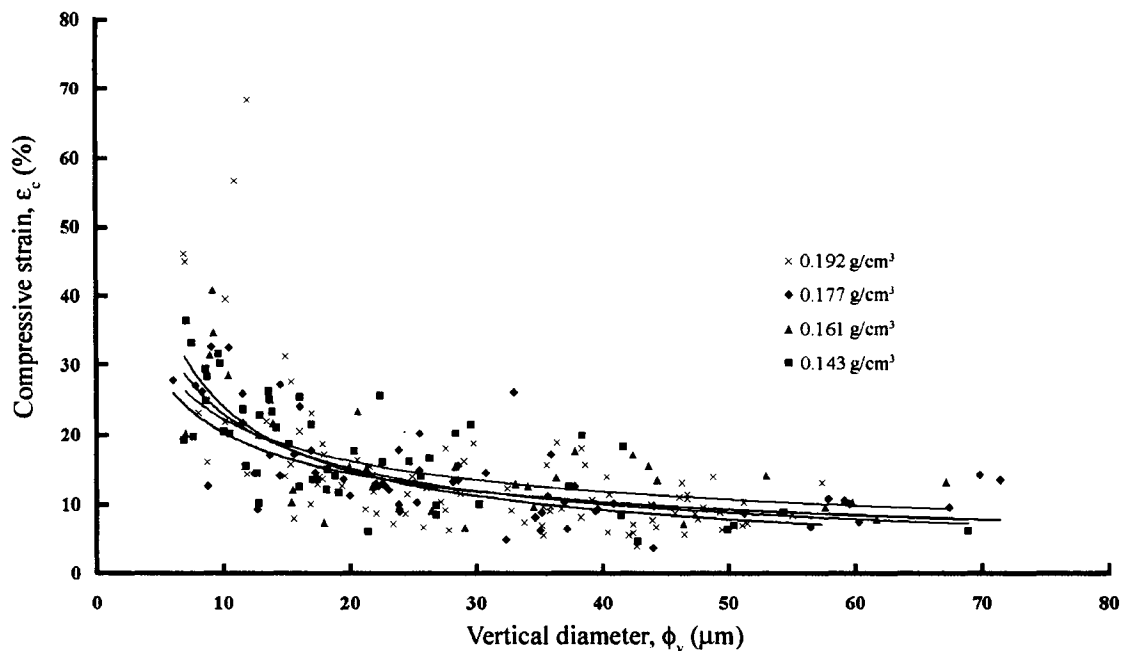
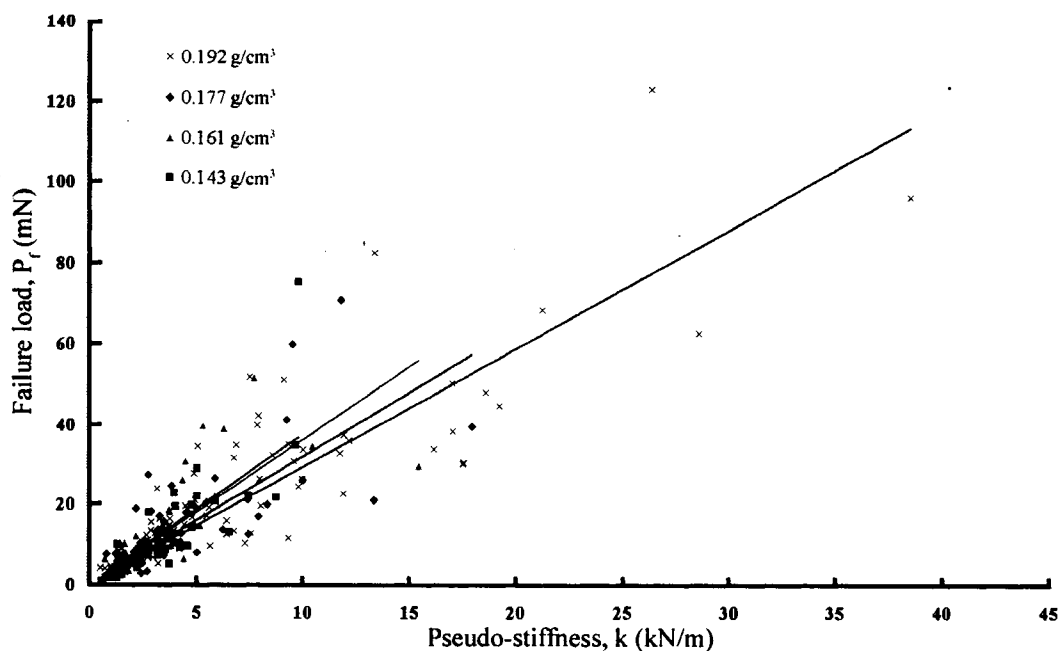
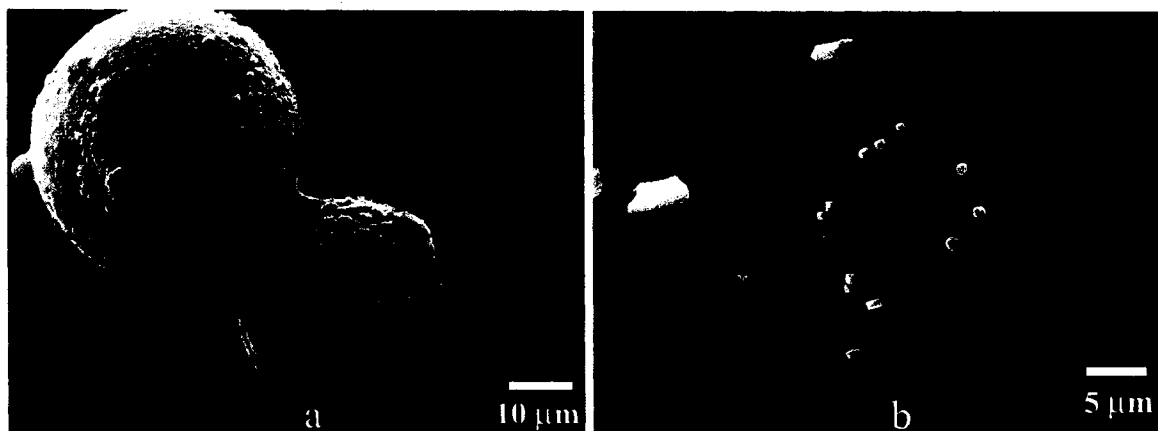


Figure 3 Compressive strain at failure vs. CMB diameter for all tap densities. The 0.192  $\text{g/cm}^3$  tap density CMBs behave as did the other three tap densities.



*Figure 4* Failure load vs. pseudo-stiffness for all tap densities. The  $0.192 \text{ g/cm}^3$  tap density CMBs have the highest stiffness at a given failure load, as expected.



*Figure 5* Micrograph of APO-BMI coated CMBs, post-cure. SEM. (a) The APO-BMI coating appears relatively continuous and bonds the CMBs in the micrograph together. (b) A post-compression test image of APO-BMI pooled beneath CMB, with shattered CMB fragments, shows evidence of gravity's effect on APO-BMI during curing.

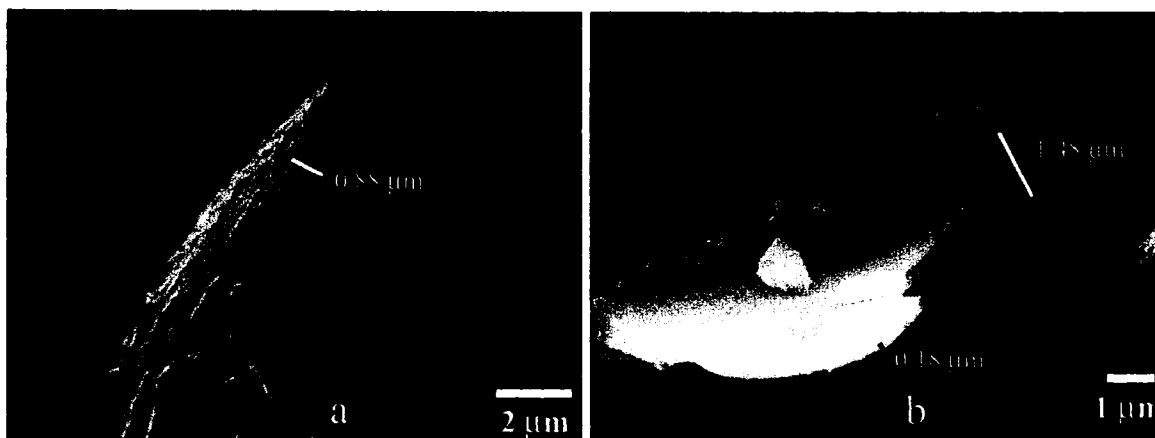


*Figure 6* Micrograph of APO-BMI-coated CMB fragments. SEM. The APO-BMI coating thickness was not visible in the cross-sections of the CMB wall observed. Some measurements of CMB wall thickness are provided.

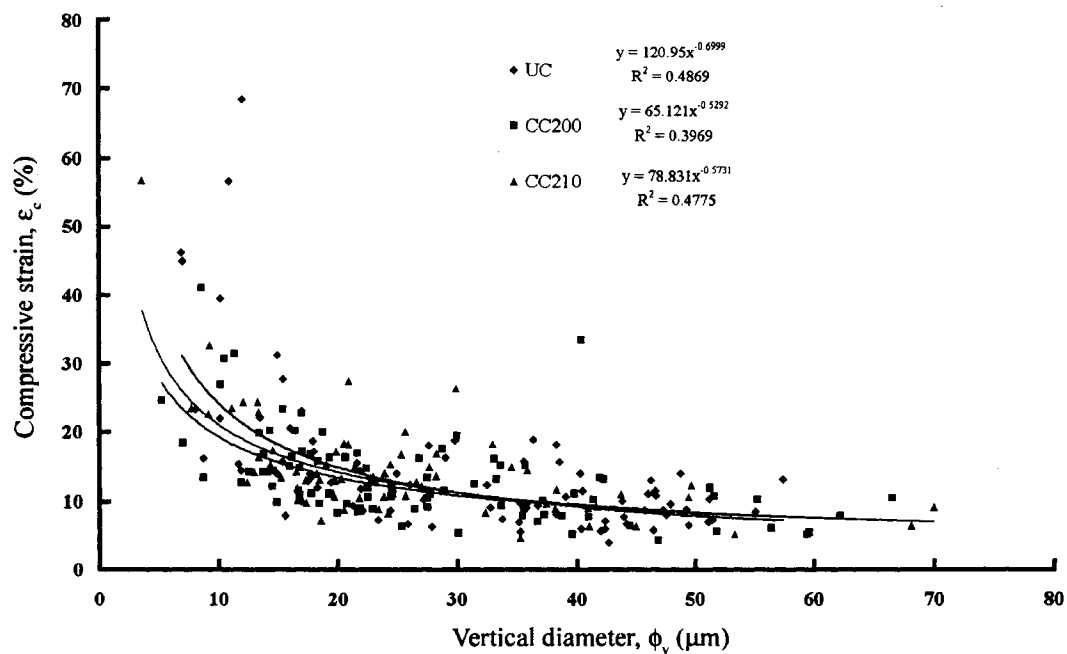


*Figure 7* Compressive strain at failure vs. CMB diameter for uncoated and APO-BMI coated, cured  $0.192 \text{ g/cm}^3$  tap density CMBs. The trend appears to be unaffected by the presence of the coating.

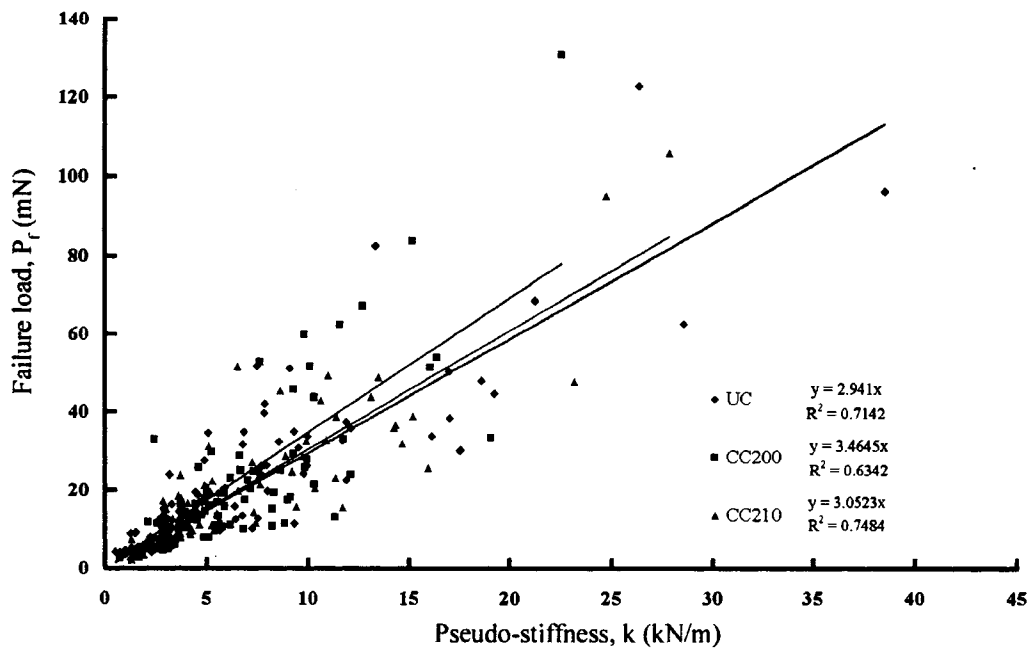


Figure 8 Failure load vs. pseudo-stiffness for uncoated and APO-BMI coated, cured  $0.192 \text{ g/cm}^3$  tap density CMBs. The trend appears to be largely unaffected by the presence of the coating.

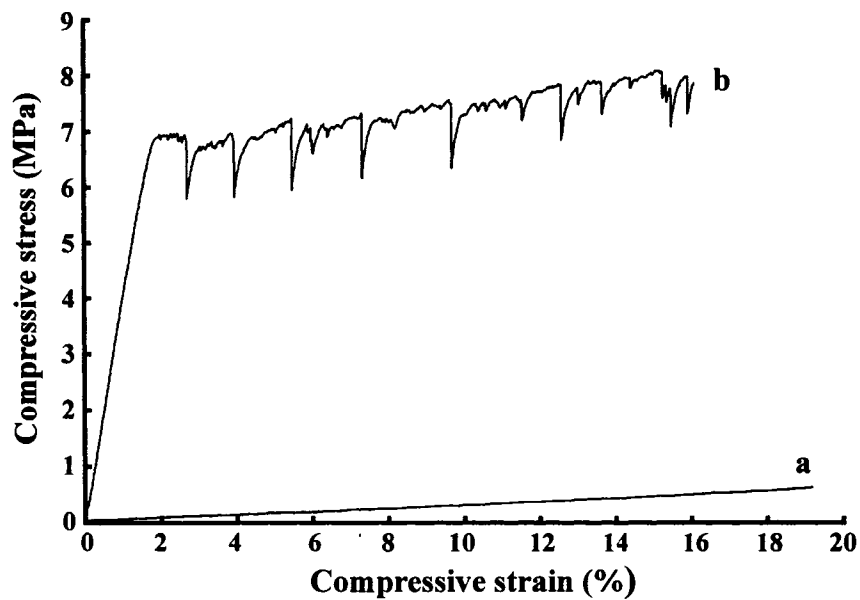


Figure 9 Representative confined compression curves for bulk uncoated CMBs and three-phase CMB foams. (a) Bulk CMBs settled in fixture by 3000 taps, per ASTM B 527. (b) Three-phase CMB syntactic foam, composed of CMBs similar to those in (a). There is significant difference in the behavior of bulk CMBs and a CMB foam, due to the effect of the APO-BMI ligaments in the foam structure.

FINITE ELEMENT MODELING OF THE UNIAXIAL COMPRESSION BEHAVIOR  
OF CARBON MICROBALLOONS I: IDEALIZED MODEL

by

K. B. CARLISLE, M. LEWIS, K.K. CHAWLA, M. KOOPMAN, G.M. GLADYSZ

Submitted to *Acta Materialia*

Format adapted for dissertation

## Abstract

Recent interest in syntactic foams has led to a multitude of new research efforts into these materials and their constituents. Our contribution includes a uniaxial compression test technique to obtain mechanical properties of single microballoons. We have used finite element modeling, with ANSYS 8.0, to simulate the uniaxial compression of individual carbon microballoons (CMBs), obtaining deformed shapes and stress states at experimentally determined microballoon failure conditions. Previously published data on CMBs, namely failure load, displacement at failure, wall thickness, and Young's modulus, were used for linear elastic analysis. Boundary conditions were chosen such that axisymmetry was achieved, and compression was conducted under displacement control. When the average conditions for three carbon microballoon populations were modeled, maximum first principal stresses at failure were predicted to range from 637 to 835 MPa. Compression of microballoons having various radius-to-thickness ratios ( $R/t$ ) was also simulated, and a transition of failure mode, from fracture in flexure to buckling, was observed at critical  $R/t$  values.

## 1. Introduction

Understanding the failure behavior of materials is crucial to being able to properly utilize them in design. In composite materials, the mechanical behavior of the individual constituents is critical, as they affect the performance and overall failure behavior. In general, the failure modes and stresses of the individual constituents in typical composites are known, and the characteristics of the matrix/reinforcement interface assume importance, because they are often not known [1]. Syntactic foams, especially three-phase syntactics, are composites wherein the characteristics of the individual phases are often not known [2]. These materials, which consist of microballoons (MBs), a binder that is typically a polymer, and intentional interstitial voids, are often composed of up to 90 % porosity, and thus their mechanical properties can be attributed primarily to their microballoon constituent [3-5]. The properties of the MBs in three-phase syntactic foams therefore require full characterization. Because they are extremely small (5-150  $\mu\text{m}$ ), mechanical testing is not a straight forward procedure. Consequently, there is little information available on the mechanical characteristics of MBs, other than bulk isostatic pressure testing performed by the manufacturers [6]. Most of the available research work deals with the compressive properties of the MBs, since this is their most common service loading condition.

While leaving the detailed ledger summarizing MB testing to other work [6], it must be noted that even though the compressive failure properties have been quantified, the basic question of how failure of a microballoon occurs is often unanswered or speculated upon at best. For example, consider the work of Bratt et al. [7], wherein they compressed single glass microballoons (GMBs) in uniaxial compression. The presumed

mechanism of failure was excessive flexural stress at the MB's equator during compression, from which the failure stress could be extracted using formulae similar to those for a flexure test. However, experimental evidence of the mechanism was absent. Previous research on GMBs, in which we developed a uniaxial compression technique using a nanoindenter, has similar limitations regarding experimental evidence of GMB failure mechanisms [8]. Work by Chung et al. [9] involved the compression testing of hollow spheres, albeit *macroballoons*. They uniaxially compressed alumina spheres of 1-2 mm diameter. Failure load was recorded, and visual observations were made of failure locations. Larger *macroballoons* were observed to fail by splitting into hemispheres along the diameter on which the load was applied, with some *macroballoons* shattering into many irregular pieces; failures of smaller *macroballoons* were deemed largely unobservable. This is quite different from the mechanism for GMB failure proposed by Bratt et al. [7], and warrants further investigation.

When dealing with MBs, the lack of an accepted theoretical solution that predicts the stresses and displacements in a thin spherical shell under compression limits analysis. Thus, finite element modeling (FEM) may yield insight into the behavior of thin, hollow spherical shells at failure. Lim et al. [10] reported the results of both experimental compression and FEM of 2 mm diameter 405 stainless steel *macroballoons*. While most of this research was directed toward characterizing the behavior of sintered hollow sphere foams, experimental normalized load-displacement curves for the compression of single spheres were presented. Additionally, they presented FEM results, using a two-dimensional, axisymmetric, linear elastic, linear kinematic work hardening model, which replicated their experimental data, while showing the sequence of deformed shapes as

plastic deformation occurred during the complete crushing of the shells. Especially interesting was the predicted progression of contact from point (initially) to circular area (intermediate) to annular as the shell was deformed into the shape of a torous. These collapse modes have been experimentally observed in aluminum hollow hemispheres, with plastic deformation occurring by what has been described as the development of rolling or stationary plastic hinges [11]. Thus, several studies of *macro*balloons have addressed the nature of their collapse modes, but *micro*balloons have yet to be considered [6].

In this paper we apply an FEM code to investigate the compression behavior and failure modes of idealized, perfectly spherical carbon microballoons (CMBs)—linear elastic, brittle materials—which have been experimentally characterized previously [12]. Specifically, the FE effort focuses on the following items:

- Prediction of the location and magnitude of the maximum stresses at failure in the carbon wall material of these CMBs under uniaxial compression.
- Effect of varying CMB size and wall thickness on their failure mode.

Additionally, Weibull statistics, a well-known analysis tool for brittle materials [1, 13], are applied to CMB data, linking experimental work and predicted FE results.

## 2. Procedure

Carbon microballoons (CMBs) have been tested in compression, yielding many properties including load, strain, stiffness, etc. These data have been previously published for three ASTM B 527 [14] tap densities of CMBs [12]. Additionally, wall thickness

measurements from both SEM and quantitative optical microscopy are available for these same CMB lots [12, 15]. The average experimentally derived material, mechanical, and geometric property data for these CMBs, shown in Table I, were used in commercially available finite element (FE) software, ANSYS 8.0, to simulate the compression of CMBs. Additional data in Table I include a literature value for the Poisson's ratio of glassy, amorphous carbon, and the longitudinal modulus and Poisson's ratio for a Saphikon fiber — the 90  $\mu\text{m}$  diameter flat-ended sapphire tip which served as the upper platen in the compression test [1, 16].

We used idealized spherical shell segments, in either two-or three-dimensions as the FE models. The two-dimensional (2D) models used axisymmetric element formulations, and the three-dimensional (3D) models used symmetry to minimize the modeled region to the positive quadrant of the sphere. Compression was modeled as a linear elastic structural, nonlinear contact analysis, using deformable bodies (platen as well as CMB) and large deformation element formulations (necessary to capture buckling behaviors). Individual element types chosen are displayed in Table II. Care was taken to choose only elements that meet the following requirements: compatible with mid-side nodes (for increased accuracy), capable of non-linear contact analysis, and capable of buckling analysis. Modeling was restricted to the linear elastic regime, since the brittle nature of the carbon material being studied did not necessitate plasticity. Boundary conditions (BCs) for the 2D and the 3D models are specified in Table III.

Mesh sizing for both types of models depended on both accuracy and CPU efficiency. For 2D models, a minimum of 4 elements spanned the wall thickness of the CMBs, which we found yielded less than a 2 percent change in the maximum stress

values predicted when 8 or 16 through-thickness elements were used while providing considerably faster solution times. For the 3D models, meshes were coarser than those used in the 2D models, with only 2 elements through the wall thickness, which still produced results which were within a few percent of those predicted by the more accurate 2D models.

Application of load in the FE models was accomplished by assigning load conditions to the platen. All loading was displacement controlled, with the CMB's failure displacement being assigned to either the top line (2D) or top area (3D) of the platen. Using a nonlinear solution process, the indenter tip was slowly sub-stepped downward, impinging upon the CMB until the full assigned displacement was reached and equilibrium of the indenter-CMB contact pair was achieved. For the average property models, the applied displacement was the average listed in Table I for each tap density CMB, but for modeling the effect of CMB radius-to-wall thickness ( $R/t$ ) ratios, the applied displacement was derived from the average experimentally determined failure strain for a CMB of the particular radius ( $R$ ) being modeled. The curve fit of the compressive strain ( $\epsilon_c$ ) vs.  $R$  curve for all CMBs, Fig. 1, provided the basis for deriving the FE displacement ( $\delta$ ) given below as a function of  $R$ , where the units for both are  $\mu\text{m}$ .

$$\delta = 0.5961R^{0.3991} \quad (1)$$

### 3. Results

The average property conditions [12, 15] for each of the three tap densities listed in Table I have been modeled in 2D, using the 2D element parameters listed in Table II. The von Mises stress ( $\sigma_{\text{von}}$ ) distributions under the average failure conditions are shown

in Fig. 2a-c. Figure 3a-c provides the accompanying principal stress distributions ( $\sigma_p$ ) for the 0.143, 0.161, and 0.177 g/cm<sup>3</sup> tap densities, respectively. To verify the 2D results, the 0.143 g/cm<sup>3</sup> tap density simulation was performed as a 3D model, using the 3D elements from Table II. Figure 4 provides the  $\sigma_{von}$ , and the  $\sigma_p$  distributions for the 3D version of this tap density's average property simulations.

To study the effect of R/t on failure mode, a parametric approach was used, with the main goal being to determine whether buckling was a likely in these CMBs. To assess the possibility of buckling, modeled CMBs were compressed in displacement control, with the maximum displacement for a particular radius being dictated by the average experimental failure strain, i.e. from Eqn. 1. The flexure/buckling transition was taken as the R/t value between where a bent curve structure transitioned to a torus-shaped one at *slightly* higher R/t. For instance, at R/t = 17.44 the partial annulus merely deforms, becoming less circular, but when R/t was increased to 17.58, a second (torus-shaped) deformation mode was predicted. The critical R/t ratio for this particular R value would then be taken as between 17.44 and 17.58.

Axisymmetric 2D FE simulations at a fixed R were performed at varying wall thicknesses (t) between the minimum and maximum observed values of 0.35 and 2.4  $\mu\text{m}$ . Figure 5a-d shows 2D FE contour plots for  $\sigma_{von}$  and  $\sigma_p$  immediately above and below the R/t value where the buckling/flexure transition is predicted to occur for a CMB of R = 10.99  $\mu\text{m}$ . Many iterations for additional R values between the minimum (2.52  $\mu\text{m}$ ) and the maximum (35.73  $\mu\text{m}$ ) allowed us to generate the failure mechanism plot shown in Fig 6. The 3D FE simulation data plotted in Fig. 6, show negligible difference from the 2D

predictions, thus verifying the buckling/flexure transitions predicted by the 2D simulations.

From Fig. 6 and Fig. 1, Fig. 7 was constructed. Figure 7 relates the FEM predictions to the original compression data, re-plotting the compression data in terms of  $\epsilon_c$  vs.  $R/t$ , where seven discrete  $t$  values were chosen as the maximum ( $t_{max}$ ), average  $\pm 1$  standard deviation ( $t_{avg \pm sd}$ ), minimum ( $t_{min}$ ), and critical ( $t_{crit}$ ) values. Note that only the trend lines have been plotted, for viewing clarity, but readers who are curious as to the scatter in the data may examine the  $\epsilon_c$  and  $R$  data in Fig. 1, of which Fig. 7 is merely a rearrangement in terms of  $t$ .

Figure 8 provides experimental evidence of the trends established in Figs. 6 and 7, showing double-logarithmic plots of CMB compressive strain at failure ( $\epsilon_c$ ) vs. the reciprocal of the survival probability ( $P$ ), where  $P$  is given as unity minus the failure probability ( $F$ ). The resulting linear trendline slopes are the Weibull modulus, a measure of the variation in strength of the material. The Weibull moduli obtained from Fig. 8 are provided in Table IV. Higher Weibull moduli correspond to more uniform strength distributions. These plots differ from the traditional Weibull usage, primarily from the necessity of using a measurable experimental parameter, failure strain, instead of failure stress. This choice was not without justification, however, as these CMBs did exhibit linear elastic, brittle behavior. Thus, stress and strain were linearly related, and strain can be substituted into the Weibull strength plots in lieu of stress.

#### 4. Discussion

One of the main goals of this work was to use FE analysis to estimate the failure stresses and their distribution in the CMBs previously experimentally tested in compression. These predicted stress distributions are shown in Figs. 2-4 for the average CMB conditions. All show maximum  $\sigma_{\text{von}}$  centered at the initial contact location between platen and MB, with another region of high effective stress on the exterior wall, just off the outer edge of platen-MB contact. Maximum values for all three average conditions were similar, ranging from 1.68 to 1.803 GPa. The  $\sigma_p$  distributions are very similar to those expected in a bend test. Maximum values ranged from 636.7 to 835.9 MPa, and minimum values ranged from -308.1 to -373.9 MPa for the three tap densities. The truly unexpected result was the prediction of relatively low stress levels at the MB's equator. Earlier researchers have assumed, based on a flexure model theory, that the maximum stresses would occur at the equator of an MB [7]. Our FEM results however, predict that the two regions subjected to the highest stresses are located on the inner surface under the contact region, and on the outer wall just past the contact region. Figure 4 provides confirmation that the simplified, 2D formulations of the MB's compression accurately represented the behavior of the 3D shell. Since all of the stress distributions are qualitatively the same in shape and location, and the maximum stress values in each differ from their 2D equivalents by less than 2 percent, with the 3D model using a coarser mesh for CPU efficiency, it was concluded that the 2D models were sufficient for the average property cases.

It can be observed that all of the predicted  $\sigma_p$ , which would be responsible for failure by the Rankine criteria, are within accepted values for certain graphites, which is

not an inappropriate matter to consider, since our earlier Raman spectroscopy work showed these MBs to be disordered  $sp^2$ - $sp^3$  carbon with crystallite sizes between 2 and 24 nm [17]. Assuming that failure in brittle CMBs occurs due to the maximum principal stress exceeding the tensile strength of the MB wall, it can be postulated that failure will initiate either on the outer wall or beneath the platen on the inner wall, both of which are regions of high  $\sigma_p$ . Given the predicted magnitude of these stresses, crack initiation will most likely originate at the inner wall location, although the larger volume (recall this is an axisymmetric 2D model) at the outer wall location might result in failure initiation in this region because of its higher likelihood of containing a critical flaw. We have no experimental verification of this, although other researchers, as mentioned in Section 1, have experimentally observed *macroballoon* failures by vertical splitting along the loading axis [9].

The reasons that the  $\sigma_p$  peaks shift from the equator of the MB toward the platen are likely twofold. The axisymmetry of the model served to partially constrain expansion of the shell in the plane of its equator, unlike a plane stress formulation, which, when modeled using FEM, is the appropriate model for a hollow cylinder (e.g., a pipe) and *does* yield the maximum  $\sigma_p$  distribution centered at the equator of the 2D cross-section. The other factor contributing to shifting the maximum  $\sigma_p$  away from the equator was the large amount of contact between the MB and platen. The supposition of a flexure model assumes point (or very nearly point) contact, rather than the large areal contact predicted in the FE models.

The size of the contact area, aside from being a possible source of the change in the  $\sigma_p$  distribution, is also a valuable entity to be able to predict. We have previously used

handbook formulas [18] and measured displacement at failure, diameter, and stiffness data to predict calculated work-of-fracture values to compare with experiments, and to determine the effective wall thickness for CMBs. It was noted that increased agreement of these calculations with experimental trends could be achieved if the contact were allowed to be non-point, but there was no experimental justification for choosing a contact area radius [12]. The present FE results, however, do provide a qualitative description of the progression of the contact area from initial point contact, via circular area contact, to annular ring contact around the top of the MB. Aside from qualitative, visual evidence, a few measurements of the contact area radius have been made using Altair's Hyperview 7.0 post-processing software. The contact radius at the average failure strain was found to be 4.497, 5.580, and 5.004  $\mu\text{m}$  for the 0.143, 0.161, and 0.177  $\text{g}/\text{cm}^3$  tap density average property models (Figs. 2 and 3), respectively. While a trend between contact radius and tap density for these measurements might initially have been expected, an examination of the average R and t values revealed there was little difference in the R/t ratio for the three average property models; thus the lack of a trend in contact radius, which depends on R *and* t of the MB, is not surprising. Additionally, comparison of FE results for MBs of different R and t values highlights the effect of MB geometry on the size of the contact region.

The effects of R and t, or more appropriately the R/t ratio, are more far-reaching than is shown by their influence on contact area. From basic mechanics of materials, there are situations where large-scale non-linear displacements occur even when loading is within the linear elastic regime. This is the result of elastic instability, namely buckling. In ductile materials, the resulting deformation can lead to stress states that are

intolerable for the material, but in brittle ceramics, the elastic instability itself usually initiates fracture. For cylindrical columns under end loading, buckling depends, via Euler formulation, on the column's slenderness ratio, i.e. length ( $\ell$ ) and diameter ( $d$ ), and its stiffness. For a given stiffness, the value of  $(\ell/d)$  above which buckling will occur is known as the critical  $(\ell/d)_c$  value. While buckling of a hollow spherical shell is much more difficult to predict, it too should have a critical geometric configuration in terms of  $R$  and  $t$ , above which buckling occurs. Figure 5 shows FE results for a CMB of  $10.99 \mu\text{m}$  radius that has been compressed to the failure displacement dictated by Eqn. 1, under conditions immediately bounding  $R/t_{\text{crit}}$  for buckling of the shell. Further parametric study of the  $R$ - $t$  space present in these CMBs reveals that  $R_{\text{crit}}$  is a parabolic function of  $t_{\text{crit}}$ , as shown in Fig.6. This parabolic dependence is likely caused by the geometry of the shell and the resulting non-zero curvature terms in the differential equation that describes the motion of the shell under load. Figure 6 provides a valuable tool in assessing the failure behavior of these CMBs, because it can facilitate predicting whether a given CMB will fail due to flexural stresses exceeding its failure strength, or due to buckling of the shell wall. The range of measured wall thickness from SEM is represented in Fig. 6 by the shaded bar near the  $x$ -axis; it is obvious that real CMBs can fail by either mechanism. To relate the possibility of buckling failure to the experimental CMB data, we revisit the experimental trend containing an engineering property and CMB size,  $\epsilon_c$  vs.  $\phi_v$ . By replotting the data in terms of  $R$  divided by four different thicknesses —  $t_{\text{avg}} \pm \text{sd}$ ,  $t_{\text{min}}$ ,  $t_{\text{max}}$ , and  $t_{\text{crit}}$  — we arrive at Figure 7. It is important to note that the plot of  $R/t_{\text{crit}}$  corresponds to the combination of  $R$ ,  $\epsilon_c$ , and  $t$  values at which buckling will occur. Clearly, CMBs possessing wall thicknesses near the minimum value will fail by buckling, and CMBs of

wall thicknesses near the maximum will fail in flexure. However, the real message from the plot is elucidated by comparing the curves —  $R/t_{avg \pm sd}$  and  $R/t_{crit}$ . CMBs with above average wall thicknesses will fail by flexure, but there is significant overlap (shaded ellipse) between the critical curve and lower standard deviation curve, especially at low failure strains. A significant portion of the lowest failure strain data can therefore be attributed to buckling failures.

Since there are two failure modes in operation, buckling and flexure, the scatter in the compressive strain data is much more understandable. Replotting the experimental data in the classic logarithmic Weibull plot of failure probability against failure strain for three tap-densities, Fig. 8, provided confirmation of large variability in failure properties, as evidenced by the low Weibull moduli (between 1.5 and 10.6) shown in Table IV. These values are more typical of traditional (pottery) ceramics than engineered ceramics. Experimental confirmation of dual failure modes, expected from the FEM predictions, is also provided by Figure 8, since the data for all three tap-densities were best fit by two linear trends for each population. In Weibull analysis, this bilinearity on a log scale is an indication of the existence of multiple mutually exclusive flaw populations, which in this case result in buckling failures for the lowest failure strains and flexural failures for the higher values. Thus, we have indirect experimental evidence of CMB failure by both buckling and flexure.

## 5. Conclusions

Finite element modeling, using ANSYS 8.0, of the uniaxial compression of carbon microballoons of three different tap densities (as per ASTM B-527) gave very

useful results. Average stress distributions were calculated and the predicted fracture stresses, ranging from 636.7 to 835.9 MPa, were determined to be reasonable failure values for the carbon wall material of these microballoons. Additionally, the locations and magnitudes of stresses indicated that failure was most likely to initiate on the microballoon's inner wall directly under the contact region, or, with slightly less likelihood, in an annular region on the outer wall of the microballoon just past the contact area. Both of these results contradicted postulations in previous work, where the maximum bending stress was suggested to occur at the microballoon's equator. The FE results have also provided valuable insight into the nature of the platen to MB contact, both qualitatively, as it transitions from point through circular to annular, and quantitatively, as the contact radius for circular contact was measured to vary between 4.497 and 5.58  $\mu\text{m}$ .

Parametric finite element modeling to assess the effect of the radius-to-wall-thickness ratio was performed, for the entire range of possible radii and thicknesses observed experimentally in these carbon microballoons. From this set of analyses, we conclude that the critical ratio for buckling to occur in these materials varies parabolically in R-t space, and that buckling is a viable failure mode in carbon microballoons of all three tap densities. Using the critical buckling ratios and the experimental strain at failure data, support for a dual-slope Weibull plot of the microballoon failure strains was developed. This instructive Weibull plot provided experimental verification of the existence of both buckling and flexural failure modes in these materials.

## 6. Acknowledgments

This work was financially supported by Los Alamos National Laboratory/DOE subcontract #44277-SOL—02 4X. The authors are grateful to Dr. D. McDowell and Dr. R. Bradt for helpful discussions. KBC is grateful to the Department of Defense for a National Defense Science and Engineering Graduate Fellowship. LA-UR-06-6129.

## 7. References

1. K.K. CHAWLA, in "Composite Materials Science and Engineering". 2nd ed (Springer-Verlag, New York, 1998) pp. 49-54.
2. G.M. GLADYSZ and K.K. CHAWLA, Composite Foams, in "Encyclopedia of Polymer Science & Technology" (John Wiley, New York, 2004) pp. 267-281.
3. M. KOOPMAN, K.K. CHAWLA, G. GLADYSZ, and K.B. CARLISLE, *J. Mater. Sci.* **41** (2006) 4009.
4. N. GUPTA, E. WOLDESENBET, and P. MENSAH, *Composites Part A: Applied Science and Manufacturing* **35** (2004) 103.
5. G.M. GLADYSZ, B. PERRY, G. MCEACHEN, and J. LULA, *J. Mater. Sci.* **41** (2006) 4085.
6. K.B. CARLISLE, K.K. CHAWLA, G.M. GLADYSZ, and M. KOOPMAN, *J. Mater. Sci.* **41** (2006) 3961.
7. P.W. BRATT, J.P. CUNNION, and B.D. SPIVAK, Mechanical Testing of Glass Hollow Microspheres, in "Advances in Materials Characterization", D.R. Rossington, R.A. Condrate, and R.L. Snyder, eds. (Plenum Press, New York, 1983) pp. 441-447.
8. M. KOOPMAN, G. GOUADEC, K. CARLISLE, K.K. CHAWLA, and G. GLADYSZ, *Scripta Materialia* **50** (2004) 593.
9. J.H. CHUNG, JOE K. COCHRAN, AND KON J. LEE, Compressive Mechanical Behavior of Hollow Ceramic Spheres, in Proceedings of Mat. Res. Soc. Symp. (Materials Research Society, 1995). pp. 179-186.
10. T.-J. LIM, B. SMITH, and D.L. MCDOWELL, *Acta Materialia* **50** (2002) 2867.
11. N.K. GUPTA, G.L.E. PRASAD, and S.K. GUPTA, *Thin-Walled Structures* **34** (1999) 21.

12. K.B. CARLISLE, M.C. KOOPMAN, K.K. CHAWLA, R.K. KULKARNI, G.M. GLADYSZ, and M. LEWIS, *J. Mater. Sci.* **41** (2006) 3987.
13. B.A. KSCHINKA, S. PERRELLA, H. NGUYEN, and R.C. BRADT, *J. Am. Ceram. Soc.* **69** (1986) 467.
14. ASTM B 527: Standard Test Method for Determination of Tap Density of Metallic Powders and Compounds, in "Annual Book of ASTM Standards" (American Society for Testing and Materials, 2000).
15. K. CARLISLE, K.K. CHAWLA, G. GOUADEC, M. KOOPMAN, and G.M. GLADYSZ, Nanocompressive properties of carbon microballoons and mechanical properties of carbon based syntactic foam composites, in Proceedings of ICCM-14, San Diego, CA, July 2003 (Society of Manufacturing Engineers, 2003).
16. *Cambridge Engineering Selector*. 2006, Granta Design Limited: Cambridge, UK.
17. G. GOUADEC, K. CARLISLE, K.K. CHAWLA, M.C. KOOPMAN, G.M. GLADYSZ, and M. LEWIS, Nano-compression of carbon micro-balloons with a flat-ended cylindrical indenter, in Proceedings of Indentation Techniques in Ceramic Materials Characterization, Apr 27-30 2004, Nashville, TN., United States (American Ceramic Society, 2004). pp. 143-152.
18. R.J. ROARK, in "Roark's Formulas for Stress and Strain", ed. W.C. Young (McGraw-Hill, New York, 1989) pp. 542-547.

## 8. Tables and Figures

Table I: Material properties for FE models.

	Tap density (g/cm <sup>3</sup> )	Young's modulus of the material, E (GPa)	Poisson's ratio of the material, $\nu$	Radius, R ( $\mu\text{m}$ )	Wall thickness, t ( $\mu\text{m}$ )	Failure displacement, $\delta$ ( $\mu\text{m}$ )
Average microballoon properties by tap density	0.143	12.76	0.22	10.99	1.32	3.88
	0.161	12.76	0.22	12.9	1.53	4.84
	0.177	12.76	0.22	14.65	2.16	4.40
	ALL	12.76	0.22	12.42	1.67	4.37
Indenter tip properties	NA	380	0.27		NA	

Table II: ANSYS elements used in CMB modeling.

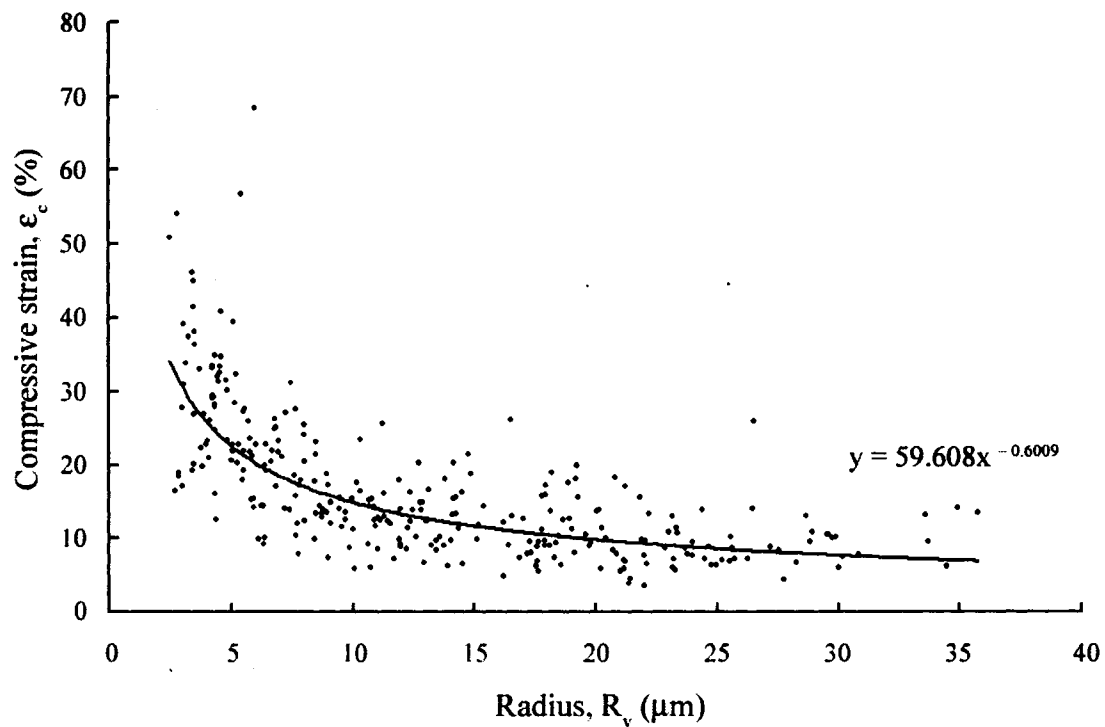
Model dimensionality	Element types		
	Material	Target	Contact
2D	PLANE183	TARGE169	CONTA172
3D	SOLID187	TARGE170	CONTA174

Table III: Boundary conditions for FEM

Model dimensionality	Elements at boundary	Boundary conditions		
		x	y	z
2D	line at x = 0	Fixed	Free	NA
	line at y = 0	Free	Fixed	NA
3D	x = 0 plane	Fixed	Free	Free
	y = 0 plane	Free	Fixed	Free
	z = 0 plane	Free	Free	Fixed

Table IV: Weibull moduli for various tap density CMBs

Tap density (g/cm <sup>3</sup> )	0.177		0.161		0.143	
Trendline	Flexure, m <sub>1</sub>	Buckling, m <sub>2</sub>	Flexure, m <sub>1</sub>	Buckling, m <sub>2</sub>	Flexure, m <sub>1</sub>	Buckling, m <sub>2</sub>
Weibull modulus, m	1.5185	3.1807	2.0105	10.606	2.0774	3.6964



*Figure 1* Experimental compressive strain at failure vs. radius for all tap density CMBs. This trend line was used to determine the displacement applied to the platen during FEM.

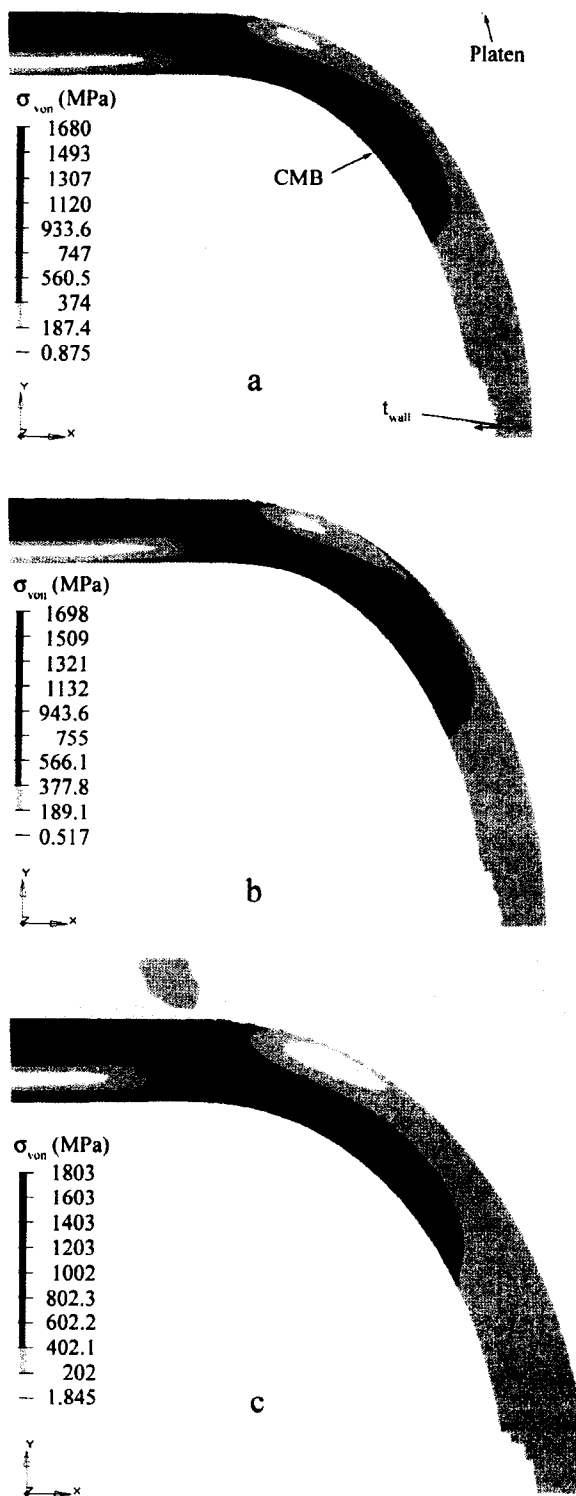
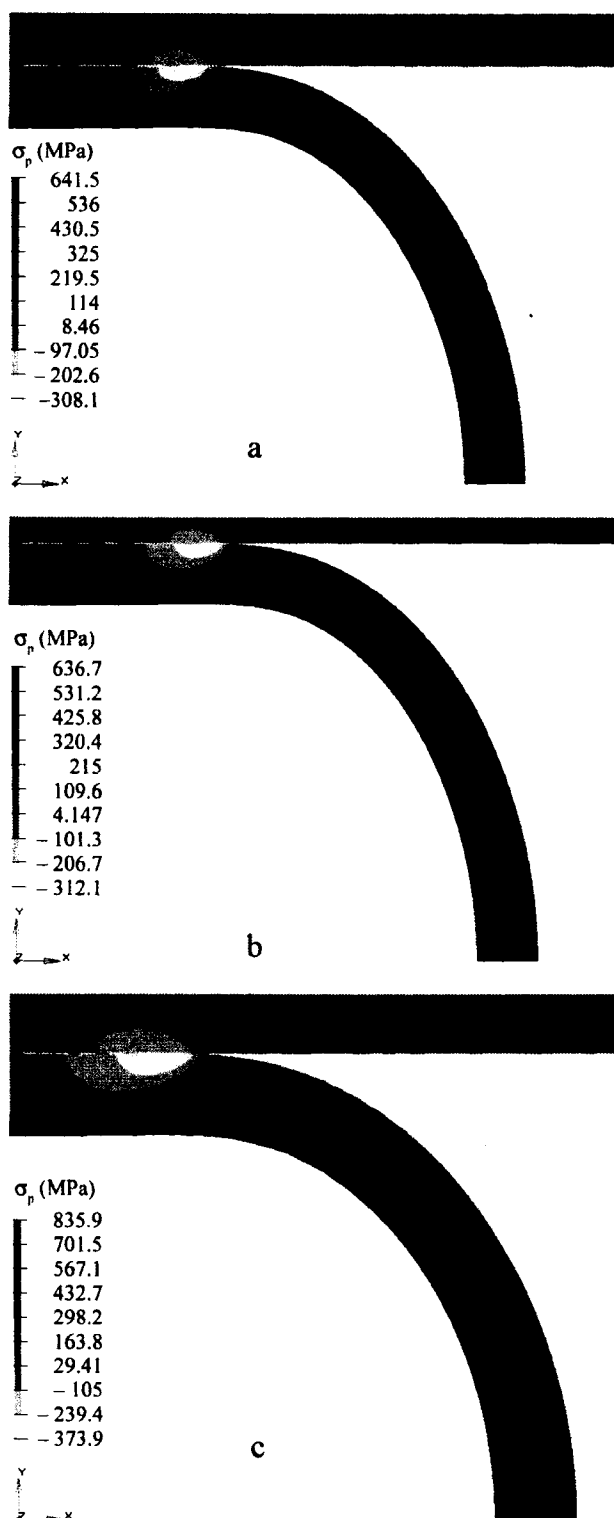


Figure 2  $\sigma_{\text{von}}$  distributions. (a)  $0.143 \text{ g/cm}^3$ , (b)  $0.161 \text{ g/cm}^3$ , (c)  $0.177 \text{ g/cm}^3$ . The trend is toward increasing stress with increasing tap density. The CMB and platen are labeled in (a).



*Figure 3*  $\sigma_p$  distributions. (a) 0.143 g/cm<sup>3</sup>, (b) 0.161 g/cm<sup>3</sup>, (c) 0.177 g/cm<sup>3</sup> tap densities. The highest tap density experiences significantly higher maximum principal stress as compared to the other two tap densities.

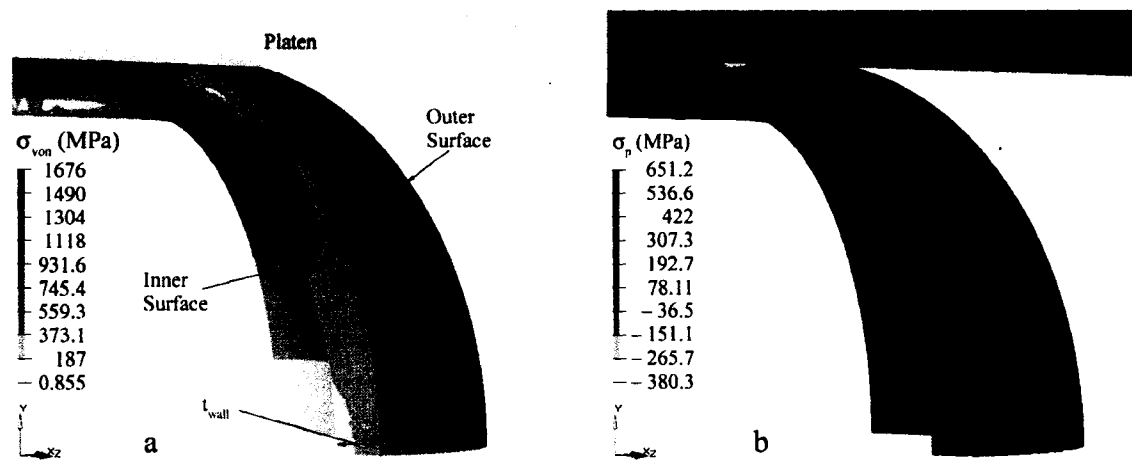


Figure 4 Predicted FE stress distributions for 3D model of  $0.143 \text{ g/cm}^3$  tap density. The CMB's 3D stress distributions are in close agreement with the 2D model predictions. The CMB and platen are labeled in (a).

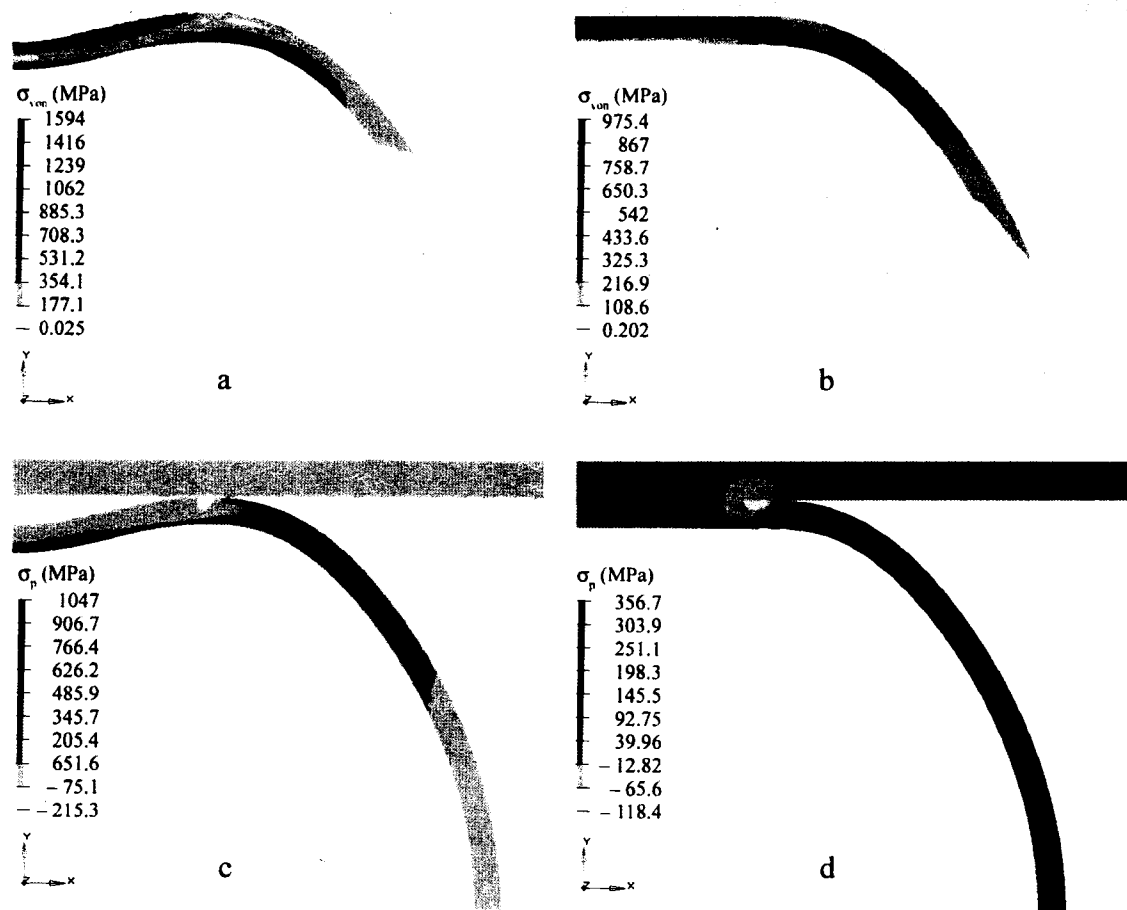
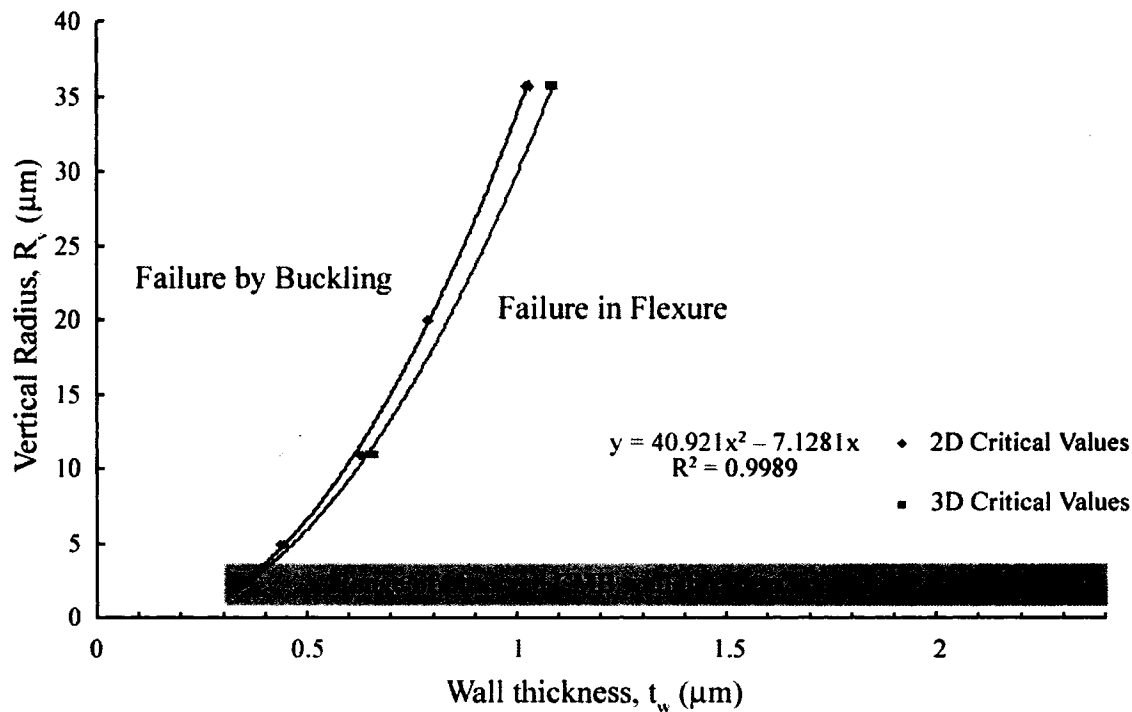
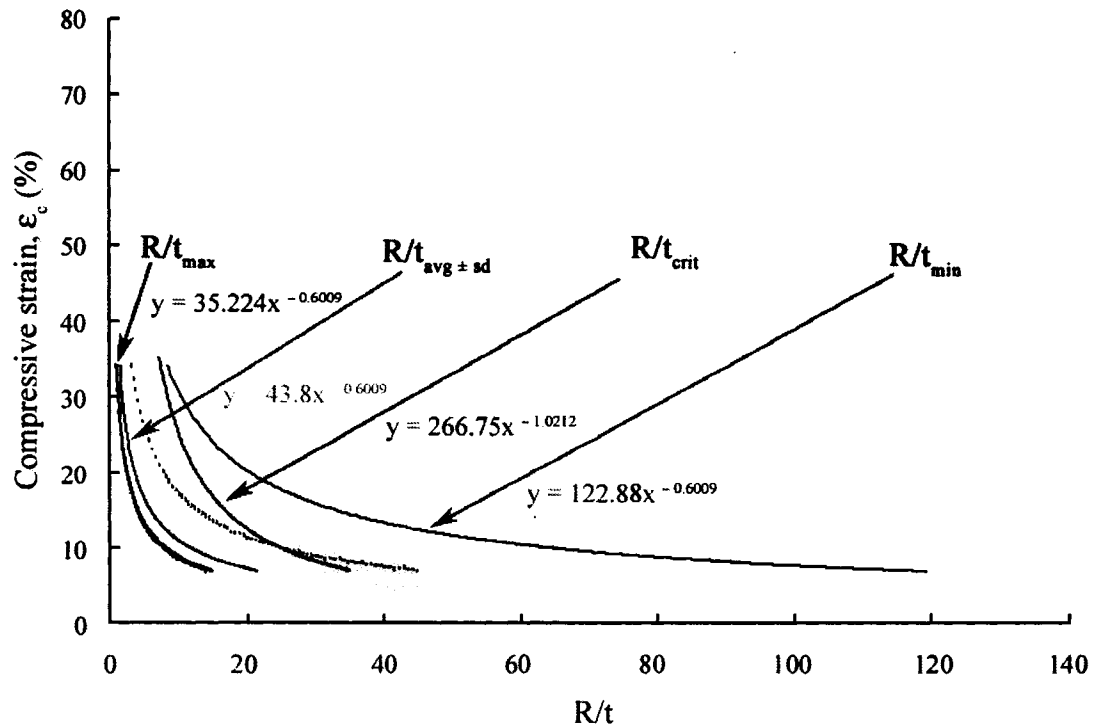


Figure 5 Buckled and unbuckled stress distributions for CMB of  $R = 10.99 \mu\text{m}$ . (a), (c), (e)  $t_{\text{wall}} = 0.625 \mu\text{m}$ ; (b), (d), (f)  $t_{\text{wall}} = 0.63 \mu\text{m}$ .  $(R/t)_{\text{crit}}$  is between 17.44 and 17.58.



*Figure 6* Failure mechanism map for CMBs. This allows the prediction of failure by excessive bending stress or by elastic instability due to buckling. The range of wall thickness, observed (SEM) as 0.3 to 2.4  $\mu\text{m}$ , shows that both failure mechanisms are operable.



*Figure 7* Compressive strain vs.  $R/t$  for minimum, maximum, average with standard deviation (dashed curves), and critical values. The  $R/t_{crit}$  curve indicates CMBs whose combination of  $\epsilon_c$  and  $R$  will yield buckling failure. Overlap, indicated by shaded ellipse, encompasses lowest compressive strains (those with highest  $R$  values), which probably failed by buckling.

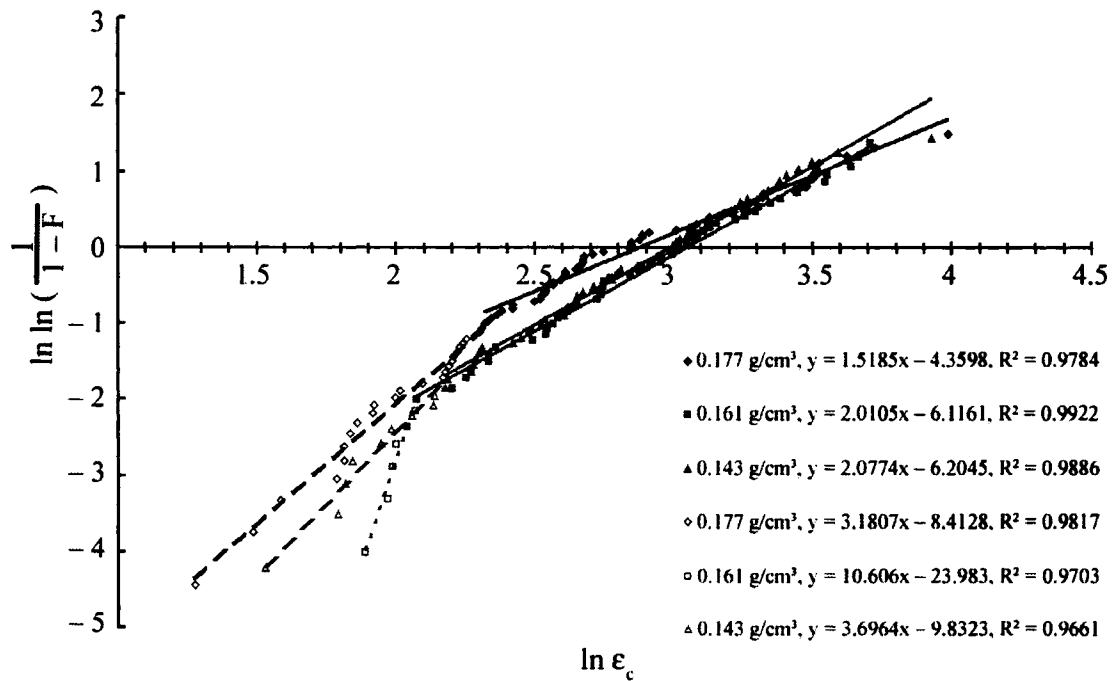


*Figure 8* Weibull plot of CMB compressive failure strains, for CMBs of three different tap densities. Very low Weibull moduli for all CMBs indicate wide variability in strength. Two linear fits for each population indicate the presence of two failure modes, probably (from FEM) flexure and buckling. Open symbols and dashed lines were used for buckling failures, solids for flexure induced failure data.

FINITE ELEMENT MODELING OF THE UNIAXIAL COMPRESSION BEHAVIOR  
OF CARBON MICROBALLOONS II: FLAWED MICROSTRUCTURES

by

K. B. CARLISLE, M. LEWIS, K.K. CHAWLA, M. KOOPMAN, G.M. GLADYSZ

Submitted to *Acta Materialia*

Format adapted for dissertation

## Abstract

Research into the mechanical properties of syntactic foams, consisting of hollow microspheres, binder, and interstitial voids, is motivated by the desire for lightweight, high specific strength materials. In a companion paper, we reported on the testing of individual microballoons (MBs) and finite element modeling of idealized MBs. The real MBs, however, have imperfections. In this paper, we focus on MBs with the two most common experimentally observed flawed microstructures—non-concentricity of inner and outer wall boundaries and through-thickness holes. We have modeled, using ANSYS 8.0, the uniaxial compression of individual carbon microballoons (CMBs) containing defects and obtained deformed shapes and stress states at experimentally determined MB failure conditions. We used published CMB data for linear elastic analysis. Boundary conditions were chosen such that axisymmetry was achieved, and compression was conducted under displacement control. The two flaw types were modeled in different locations on the MB relative to the location of load application, and their effects on the stress state of the material were evaluated. It was concluded that the through-thickness holes in MB walls were the more detrimental defect to the compressive properties of the CMBs, despite the fact that thin regions in an MB's wall could cause buckling in a situation where the MB's average radius and thickness would otherwise predict failure to occur in flexure.

## 1. Introduction

How a material behaves at failure is critical to properly using it in a design, especially for composite materials. With composites, the mechanical behavior of the individual constituents becomes crucial [1]. Syntactic foams, especially three-phase syntactics, are one such composite [2]. Three-phase syntactic foams consist of microballoons (MBs), a binder that is typically a polymer, and intentional interstitial voids, and their void contents often approach 90 percent. Such a high percentage of porosity means that the properties of the MBs are the determining factor for the compressive properties of the entire foam [3-5]. Despite the importance of understanding MB failure behaviors, relatively few studies have attempted to characterize MBs [6], and of them, only Bratt et al. [7] and our own works [8-10] have hypothesized as to the failure mechanism of the MBs. Several studies of *macro*balloons have addressed the nature of their collapse modes, finding that most *macro*balloons fail in uniaxial compression by vertical splitting along the loading axis [11-13], but our companion paper provides the only investigation of MB failure mechanisms [9].

In this paper we explore the compressive behavior and failure modes of *flawed* carbon microballoons (CMBs)—linear elastic, brittle materials—which were experimentally characterized previously [8]. Specifically, the FE effort, using ANSYS 8.0, focuses on the effect of the most commonly observed flaws—through-thickness holes in the walls of MBs and internal hollows that are not concentric with the external surface of the MBs—on the stress state in these materials.

## 2. Procedure

Details of the modeling procedures were outlined in detail in a companion article [9]. Compression testing of carbon microballoons (CMBs) provided us the data for three [14] tap-densities (ASTM B 527) of CMBs, as well as their microstructural aspects [8, 15]. From SEM and optical microscopy, the morphology of these CMBs was determined to possess two common flaws. The first case was one wherein the internal cavity of the CMB was not concentric with the external surface of the shell, resulting in a thin region in the CMB's wall. The second basic flaw observed was that of a through-thickness hole in the CMB's wall. These two flawed geometries were combined with the average experimentally derived material, mechanical, and geometric property data for the CMBs, shown in Table I, in ANSYS 8.0 finite element (FE) software to simulate the compression of CMBs. Additional data in Table I on the upper compression platen was used for the model, namely the longitudinal modulus and Poisson's ratio for a Saphikon fiber — the 90  $\mu\text{m}$  diameter flat-ended sapphire tip used in the compression test [1].

As before, the compression was modeled in two-dimensional (2D) models using axisymmetric element formulations and in three-dimensional (3D) models using symmetry. Since these CMBs are brittle, elastic materials, the simulations were linear elastic structural, nonlinear contact analysis, using deformable bodies and large deformation element formulations. The element types chosen are displayed in Table II, and the boundary conditions (BCs) used for the 2D and the 3D models are given in Table III.

Meshing for 2D and 3D models attempted to balance accuracy and CPU efficiency. A minimum of 4 elements spanned the wall thickness of the CMBs in 2D

models. This number was used since it produced less than a 2 percent loss in the accuracy of the predicted maximum stress values when compared to models using 8 or 16 through-thickness elements. The 3D meshes were generally coarser than those used in the 2D models, using 2 through-thickness elements in regions far from the hole in the wall and 4 or 8 elements through-thickness around the hole.

Load application in *all* models was under displacement control, with the experimentally determined failure displacement for a CMB being assigned to the top of the platen. The applied displacement ( $\delta$ ) was derived from the average failure strain for a CMB of the radius ( $R$ ) being modeled, using the curve fit of the previously published experimental compressive strain ( $\epsilon_c$ ) vs.  $R$  curve for all CMBs, namely,

$$\delta = 0.5961R^{0.3991} \quad (1)$$

where  $\delta$  and  $R$  are in  $\mu\text{m}$ .

### 3. Results

Until this point, the possibility of imperfect CMBs has been ignored, with the only deviation considered being that of the distribution of wall thicknesses and diameters present in the CMB populations. However, a perusal of prior works [6, 8, 15, 16] and of Fig. 1 presents observations of these two very common types of flaws in single-walled CMBs — non-concentric interiors and through-thickness holes in CMBs.

Axisymmetric models containing the two most frequently microscopically observed basic flaw types were studied via the FE analysis procedures described above. In both cases,  $R = 20 \mu\text{m}$  was used, to facilitate comparison. In the concentricity study, the average wall thickness ( $t_{\text{avg}}$ ) was held at  $1.67 \mu\text{m}$  while the minimum thickness ( $t_{\text{min}}$ )

was varied between 0.2 and 1.67  $\mu\text{m}$ . A representative micrograph of a through-thickness hole, verified by observing the wall thickness of the CMB when tilting the sample, is shown in Fig. 1. The overall average size of the holes observed via SEM was a 3  $\mu\text{m}$  radius, in a CMB averaging 40  $\mu\text{m}$  in diameter. In the FE models, the position of the hole was varied from 0°-90° with respect to the y-axis.

In studying the non-concentricity flaw, it was determined that the thin region would be modeled in two locations. This was an attempt to ascertain the effect of the MB's orientation with respect to axis of load application. Figures 2 and 3 provide the von Mises ( $\sigma_{\text{von}}$ ) and principal ( $\sigma_{\text{p}}$ ) stress distributions for models where the thin region was positioned directly under the initial platen contact. Figures 4 and 5 exemplify the same three distributions for the thin area located on the MB's equator. All of these models are axisymmetric, 2D representations of the MB's behavior when these thin regions are introduced in the MB's wall.

Figure 6 illustrates the FE morphology used for modeling a CMB with a hole, and provides explanation for the sectioned views shown in subsequent figures. Figures 7 and 8 provide the 3D distributions of  $\sigma_{\text{von}}$  and  $\sigma_{\text{p}}$ , at a constant wall thickness of 1.67  $\mu\text{m}$ , for both the perfect shell (no hole) and the following hole positions: 0°, 45°, and 90°. Finally, the effect of wall thickness on the stress distribution around a hole in an MB wall is demonstrated in Figs. 9 and 10, which display  $\sigma_{\text{von}}$  and  $\sigma_{\text{p}}$  distributions for wall thickness variations between 0.85  $\mu\text{m}$  and 2.4  $\mu\text{m}$ , where the position of the hole was constant throughout.

#### 4. Discussion

As can be seen in Fig. 2a-d, the maximum  $\sigma_{von}$  decreased from 1095 MPa for a CMB of uniform wall thickness to 821.6 MPa for a CMB with a non-concentric interior that created a  $t_{min}$  of 0.9  $\mu\text{m}$ . An examination of Fig. 3 revealed that the location of the maximum  $\sigma_p$  was directly under the platen on the inner wall of the CMB for the uniform wall thicknesses but shifted towards to the outer surface just past the platen-MB contact region as the wall became thinner. The decrease in thickness reduced the distance from  $\sigma_p$  to the neutral axis, reducing the flexural stresses in the region beneath the platen; hence, the shift in the region possessing the maximum  $\sigma_p$ . For parts (e) and (f) of Figs. 2 and 3, failure would have occurred at the onset of buckling, at a  $t_{min}$  similar to that already identified for idealized CMBs as the critical value for buckling at this CMB radius [9]. Thus, the thinnest region of an otherwise thick-walled CMB controls the failure mechanism.

The effect of placing the thin region in a location less-likely to occur during the experimental compression of a single CMB (gravity is likely to place the thinnest spot at the top of a CMB resting freely on a flat surface) was modeled, and the results are shown in Figs. 4 and 5. Maximum  $\sigma_{von}$  and maximum  $\sigma_p$  values showed little difference from the prior case, but the  $\sigma_p$  distribution and buckling behavior were greatly affected. It was expected that the maximum  $\sigma_p$  values would shift to the CMBs equator due to the presence of the flaw. However, this was not the case. The maximum values, as seen in Fig 5b-e, were predicted on the inner wall under the platen, as in the uniform thickness model in Fig. 7a. The difference, caused by the decreasing cross-sectional area near the equator, was the increased stress in the wall at the equator as thickness decreased.

Buckling, resulting in a torus-shaped internal cavity, did finally occur in this configuration, as seen in Fig 5f, but at a  $t_{\min}$  of 0.2  $\mu\text{m}$ , below the minimum CMB wall thickness observed via SEM.

The effect of through-thickness holes in the CMB walls was also evaluated by modeling, and a sample FE geometry is shown in Fig. 6. The position of the hole in these models was fixed in the sectioning plane shown in Fig. 6a, but the angular position of the hole in the plane was varied from 0 to 90 degrees with respect to the y-axis. Figure 6b shows the zoomed, cut view, which was used to evaluate the effect of the hole in subsequent figures. Figures 7 and 8 provide the  $\sigma_{\text{von}}$  and  $\sigma_{\text{p}}$  distributions for four different hole conditions: (a) a perfect (no hole) shell, (b) a hole centered about the y-axis, (c) a hole at a 45° angle to the y-axis, and (d) a hole positioned in the  $y = 0$  plane. Comparing Fig. 7b-d to Fig. 7a, the hole, as expected, did act as a stress riser, and its position determined the amount of increase in the effective stress. The closer the hole was located to the maximum stress position for the perfect shell, the greater was the increase in stresses (up to 49 % increase), whereas a hole located at the MB's equator only increased the maximum stress by 3 %. Also note that in each position, the maximum or very near the maximum equivalent stresses were present at the hole. From Fig. 8a-d, the effect on  $\sigma_{\text{p}}$  was seen to be most detrimental in the 45° position, where the principal stress increased by a factor of two over values of the perfect, unpenetrated shell. Thus, the increase in stress caused by the hole was a function of the hole's position relative to the maximum stress location for a perfect, unpenetrated CMB. The closer that the hole was to the region of high stress, the greater was the detrimental effect on the CMB's stress state. The last goal of hole modeling was to determine the effect of wall thickness

changes on the stress states of CMBs containing a hole. For this, the hole position of  $45^\circ$  was chosen and wall thickness varied from 0.85 to 2.4  $\mu\text{m}$ . As can be seen in Fig. 9a-e, the maximum effective stress, located at the y-axis and at the hole, increased with wall thickness. There was a 69 % increase in stress caused entirely by increasing the CMB wall thickness, a much more profound increase than that caused by introducing or moving the hole, as in Figs. 7 and 8. Why did an increase in wall thickness and in cross-sectional area lead to increased stresses? Figure 10, showing  $\sigma_p$  distributions, predicted increases in maximum  $\sigma_p$  of 15 % over the range of thicknesses. The location and distribution of these maxima resembled those in flexure of a beam. Flexural stresses depend strongly on the distance of the stressed elements from the neutral axis of the beam. Thus, increasing thickness increased the distance from the free surfaces (location of maximum stress values) to the neutral axes, which explained the increased stress values.

A comparison among all of the flawed models, which plotted stresses at a given average strain, revealed the relative detrimental effect of each flaw type to the structural integrity of the CMB under compression. For each case, we observed that the presence of a hole led to significantly higher stress levels in the material than did the presence of a thin region in the wall. The only exception to this rule was that of buckling failures. CMBs with holes did not seem to exhibit greater propensities to fail in buckling; however, once the minimum thickness of a non-concentric CMB reached a value near the critical buckling value for a uniform-walled CMB, buckling was predicted to occur if the thin region was oriented directly beneath the load.

## 5. Conclusions

Finite element modeling, using ANSYS 8.0, of the uniaxial compression of flawed carbon microballoons of three different tap-densities (as per ASTM B-527) gave very useful results. The effects of non-concentricity and through-thickness holes on the compressive stress distributions in CMBs were obtained. When thin regions were present in CMB walls, the propensity of buckling failures increased, as thin regions tended to produce buckling even when the average wall thickness was well above that critical for buckling of uniform CMBs. Otherwise, non-concentric defects were concluded to have little detrimental effect on mechanical properties, as only marginal stress increases were observed as  $t_{\min}$  decreased. For CMBs with holes in their walls, it was apparent that the hole acted as a stress riser, both increasing the maximum stress experienced by the shell and serving to locate much higher stresses in the region around the hole, regardless of its location in the shell. Wall thickness was also observed to play a major role in increasing stress values when a hole was present, with higher stresses observed at greater wall thicknesses. Comparatively, the presence of holes was seen to increase the stresses in the CMBs to a far greater extent than thin regions, thus heightening the chance of failure more than moderately thin regions in a CMB's wall.

## 6. Acknowledgments

This work was financially supported by Los Alamos National Laboratory/DOE subcontract #44277-SOL—02 4X. The authors are grateful to Dr. D. McDowell and Dr. R. Bradt for helpful discussions. KBC is grateful to the Department of Defense for a National Defense Science and Engineering Graduate Fellowship. LA-UR-06-6129.

## 7. References

1. K.K. CHAWLA, in "Composite Materials Science and Engineering". 2nd ed (Springer-Verlag, New York, 1998) pp. 49-54.
2. G.M. GLADYSZ and K.K. CHAWLA, Composite Foams, in "Encyclopedia of Polymer Science & Technology" (John Wiley, New York, 2004) pp. 267-281.
3. M. KOOPMAN, K.K. CHAWLA, G. GLADYSZ, and K.B. CARLISLE, *J. Mater. Sci.* **41** (2006) 4009.
4. N. GUPTA, E. WOLDESENBET, and P. MENSAH, *Composites Part A: Applied Science and Manufacturing* **35** (2004) 103.
5. G.M. GLADYSZ, B. PERRY, G. MCEACHEN, and J. LULA, *J. Mater. Sc.* **41** (2006) 4085.
6. K.B. CARLISLE, K.K. CHAWLA, G.M. GLADYSZ, and M. KOOPMAN, *J. Mater. Sci.* **41** (2006) 3961.
7. P.W. BRATT, J.P. CUNNION, and B.D. SPIVAK, Mechanical Testing of Glass Hollow Microspheres, in "Advances in Materials Characterization", D.R. Rossington, R.A. Condrate, and R.L. Snyder, eds. (Plenum Press, New York, 1983) pp. 441-447.
8. K.B. CARLISLE, M.C. KOOPMAN, K.K. CHAWLA, R.K. KULKARNI, G.M. GLADYSZ, and M. LEWIS, *J. Mater. Sci.* **41** (2006) 3987.
9. K.B. CARLISLE, M. LEWIS, K.K. CHAWLA, M. KOOPMAN, and G.M. GLADYSZ, *Acta Materialia* (2006) This issue.
10. M. KOOPMAN, G. GOUADEC, K. CARLISLE, K.K. CHAWLA, and G. GLADYSZ, *Scripta Materialia* **50** (2004) 593.
11. J.H. CHUNG, JOE K. COCHRAN, AND KON J. LEE, Compressive Mechanical Behavior of Hollow Ceramic Spheres, in Proceedings of Mat. Res. Soc. Symp. (Materials Research Society, 1995). pp. 179-186.
12. N.K. GUPTA, G.L.E. PRASAD, and S.K. GUPTA, *Thin-Walled Structures* **34** (1999) 21.
13. T.-J. LIM, B. SMITH, and D.L. MCDOWELL, *Acta Materialia* **50** (2002) 2867.
14. ASTM B 527: Standard Test Method for Determination of Tap Density of Metallic Powders and Compounds, in "Annual Book of ASTM Standards" (American Society for Testing and Materials, 2000).

15. K. CARLISLE, K.K. CHAWLA, G. GOUADEC, M. KOOPMAN, and G.M. GLADYSZ, Nanocompressive properties of carbon microballoons and mechanical properties of carbon based syntactic foam composites, in Proceedings of ICCM-14, San Diego, CA, July 2003 (Society of Manufacturing Engineers, 2003).
16. G. GOUADEC, K. CARLISLE, K.K. CHAWLA, M.C. KOOPMAN, G.M. GLADYSZ, and M. LEWIS, Nano-compression of carbon micro-balloons with a flat-ended cylindrical indenter, in Proceedings of Indentation Techniques in Ceramic Materials Characterization, Apr 27-30 2004, Nashville, TN., United States (American Ceramic Society, 2004). pp. 143-152.

## 8. Tables and Figures

Table I: Material properties for FE models

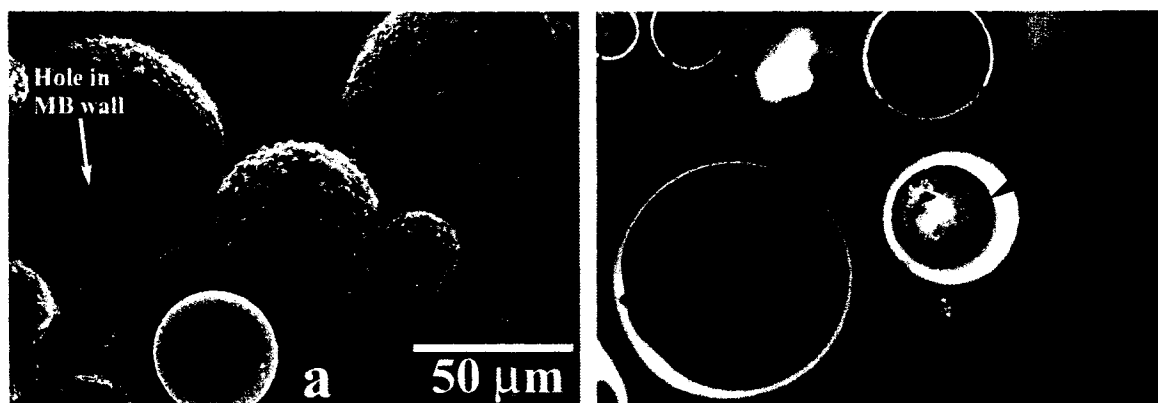
	Tap density (g/cm <sup>3</sup> )	Young's modulus of the material, E (GPa)	Poisson's ratio of the material, $\nu$	Radius, R ( $\mu\text{m}$ )	Wall thickness, t ( $\mu\text{m}$ )	Failure displacement, $\delta$ ( $\mu\text{m}$ )
Average microballoon properties by tap density	0.143	12.76	0.22	10.99	1.32	3.88
	0.161	12.76	0.22	12.9	1.53	4.84
	0.177	12.76	0.22	14.65	2.16	4.40
	ALL	12.76	0.22	12.42	1.67	4.37
Indenter tip properties	NA	380	0.27		NA	

Table II: ANSYS elements used in CMB modeling

Model dimensionality	Element types		
	Material	Target	Contact
2D	PLANE183	TARGE169	CONTA172
3D	SOLID187	TARGE170	CONTA174

Table III: Boundary conditions for FEM

Model dimensionality	Elements at boundary	Boundary conditions		
		x	y	z
2D	line at x = 0	Fixed	Free	NA
	line at y = 0	Free	Fixed	NA
3D	x = 0 plane	Fixed	Free	Free
	y = 0 plane	Free	Fixed	Free
	z = 0 plane	Free	Free	Fixed



*Figure 1* Representative micrographs of flawed CMBs. (a) The average size of all holes observed in these CMBs was a 3  $\mu\text{m}$  radius, in a CMB averaging 40  $\mu\text{m}$  in diameter. SEM. (b) Non-concentric internal hollows were commonly observed in single-walled CMBs, over a wide range of CMB diameters.

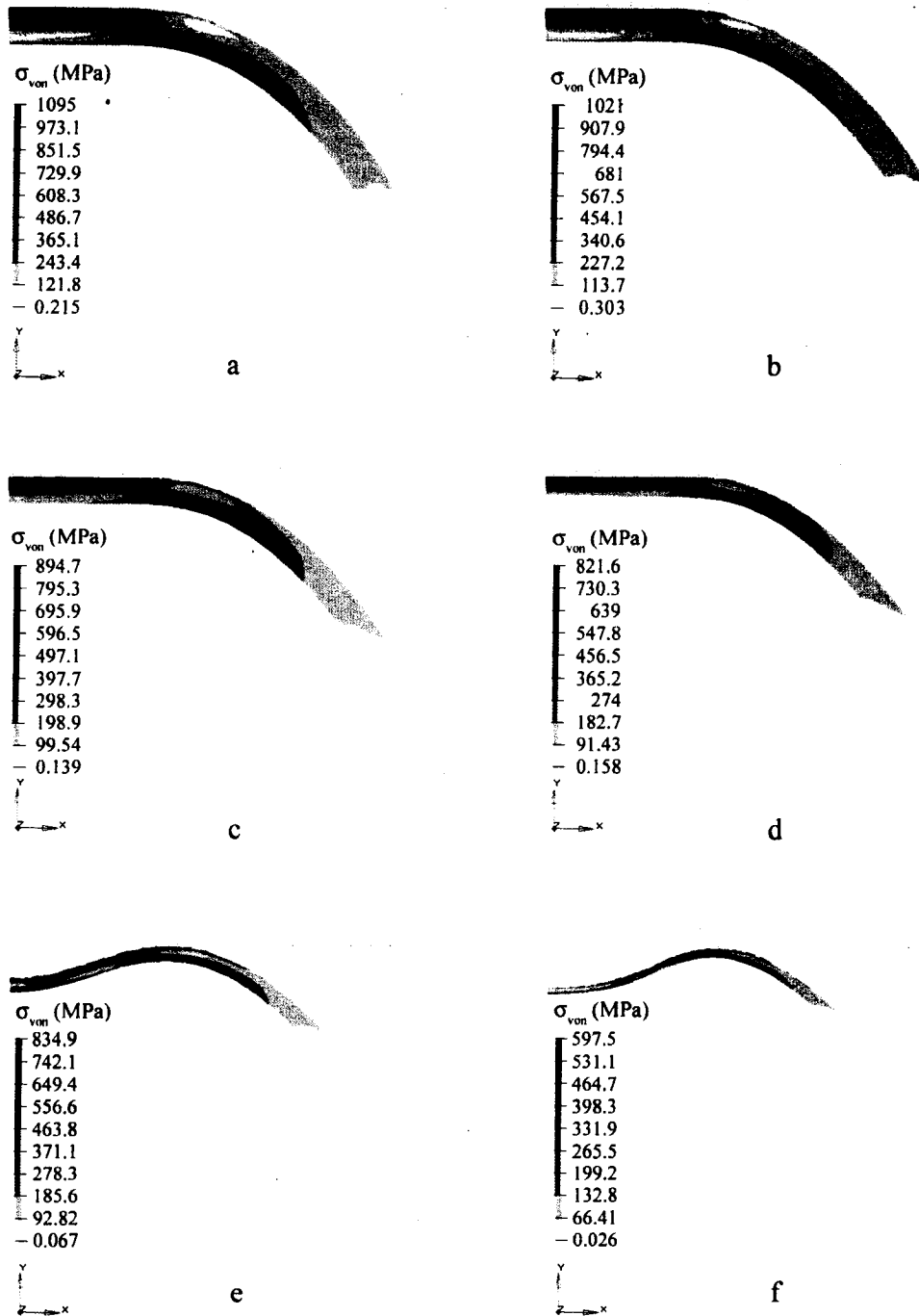


Figure 2  $\sigma_{von}$  distribution for CMB of  $R = 20 \mu\text{m}$  and  $t_{avg} = 1.67 \mu\text{m}$ , with thin region on loading axis. (a) Uniform  $t_{wall}$ , (b)  $t_{min} = 1.6 \mu\text{m}$ , (c)  $t_{min} = 1.2 \mu\text{m}$ , (d)  $t_{min} = 0.9 \mu\text{m}$ , (e)  $t_{min} = 0.6 \mu\text{m}$ , (f)  $t_{min} = 0.3 \mu\text{m}$ . The maximum stress decreased as  $t_{min}$  decreased, until buckling occurred.

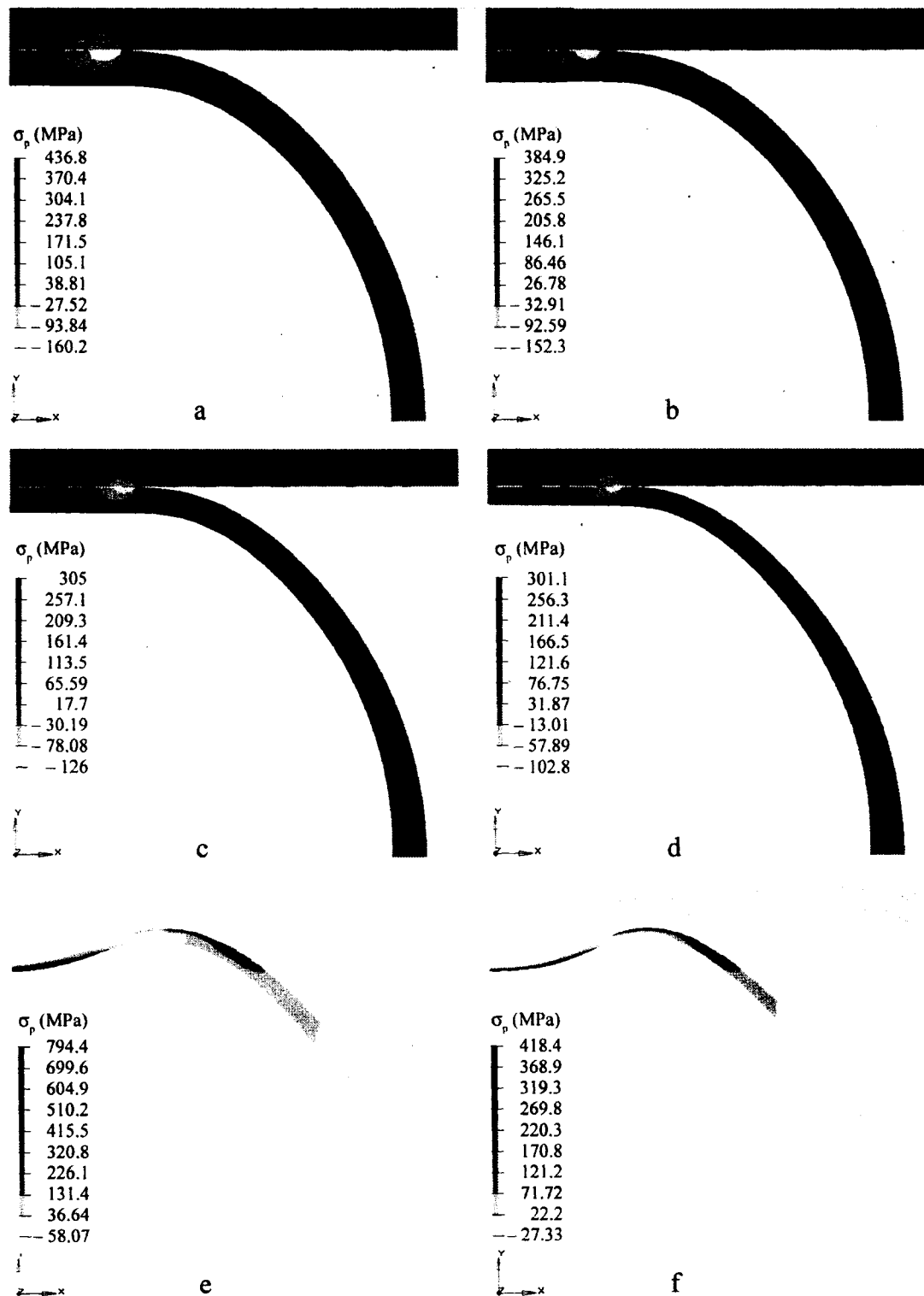


Figure 3  $\sigma_p$  distribution for CMB of  $R = 20 \mu\text{m}$  and  $t_{\text{avg}} = 1.67 \mu\text{m}$ , with thin region on loading axis. (a) Uniform  $t_{\text{wall}}$ , (b)  $t_{\min} = 1.6 \mu\text{m}$ , (c)  $t_{\min} = 1.2 \mu\text{m}$ , (d)  $t_{\min} = 0.9 \mu\text{m}$ , (e)  $t_{\min} = 0.6 \mu\text{m}$ , (f)  $t_{\min} = 0.3 \mu\text{m}$ . The principal stress decreased directly under the platen but increased on the external wall of the MB near the contact region as  $t_{\min}$  decreased.

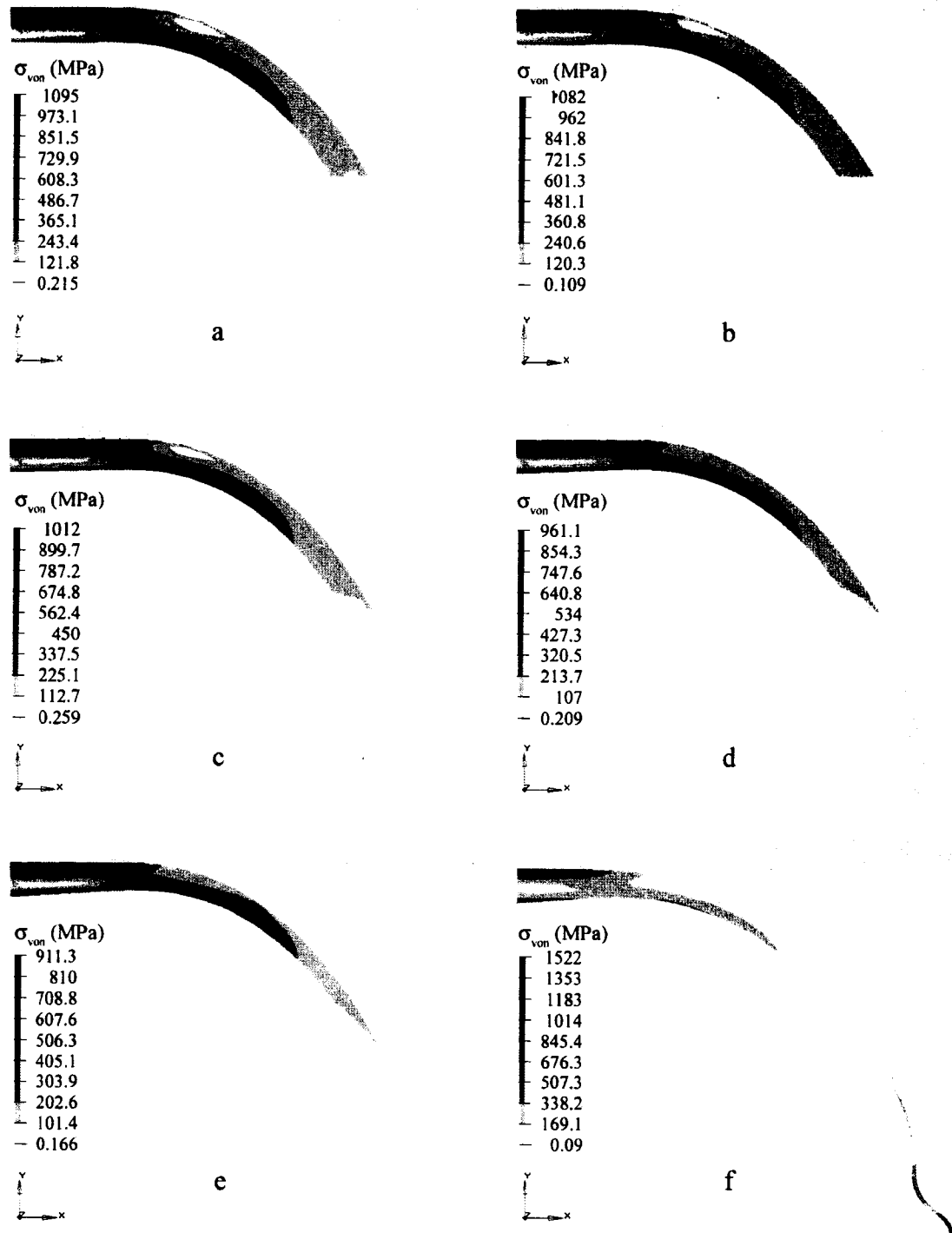


Figure 4  $\sigma_{von}$  distribution for CMB of  $R = 20 \mu\text{m}$  and  $t_{avg} = 1.67 \mu\text{m}$ . (a) Uniform  $t_{wall}$ , (b)  $t_{min} = 1.6 \mu\text{m}$ , (c)  $t_{min} = 1.2 \mu\text{m}$ , (d)  $t_{min} = 0.9 \mu\text{m}$ , (e)  $t_{min} = 0.6 \mu\text{m}$ , (f)  $t_{min} = 0.2 \mu\text{m}$ . The maximum stress decreased slightly as  $t_{min}$  decreased, until buckling occurred.

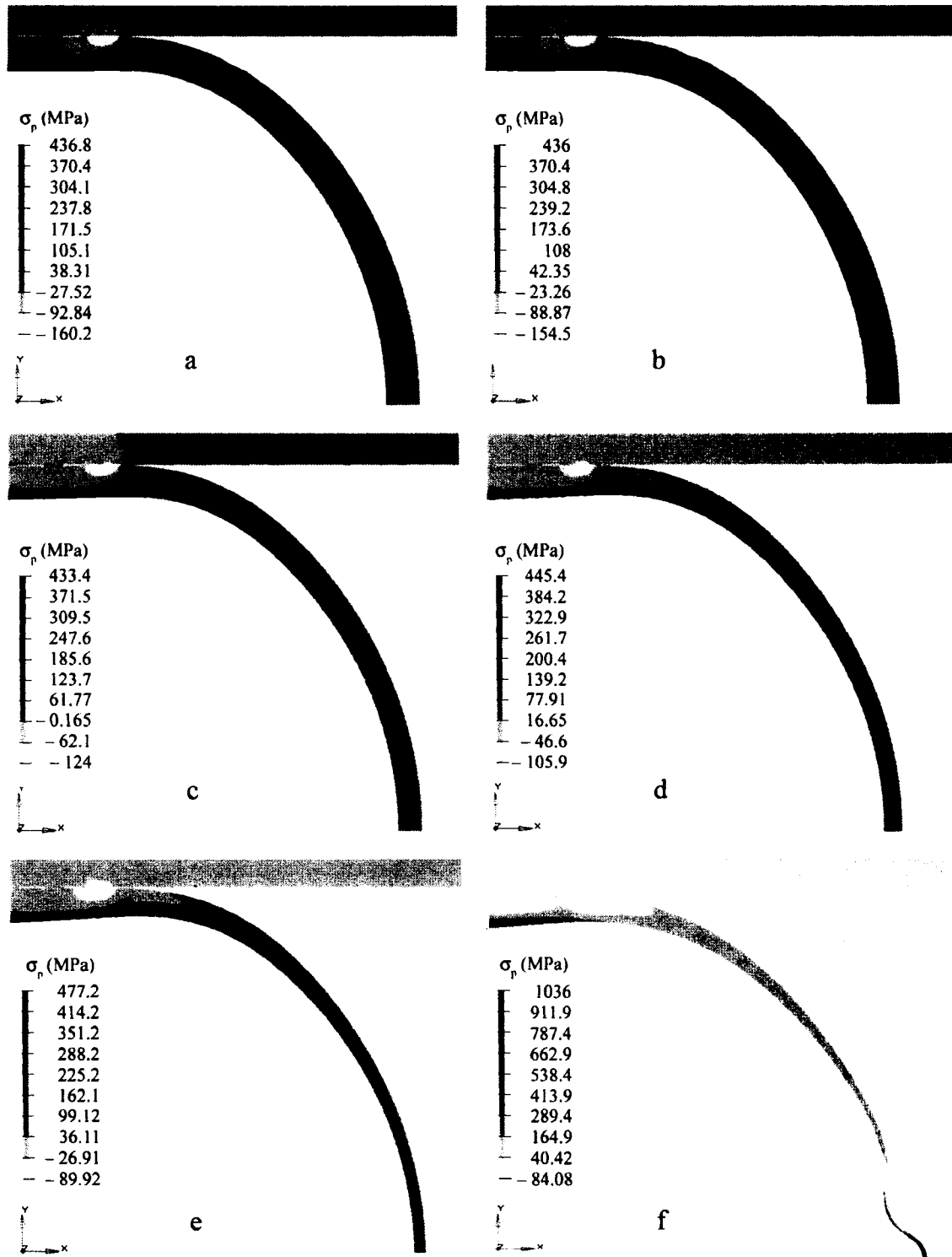
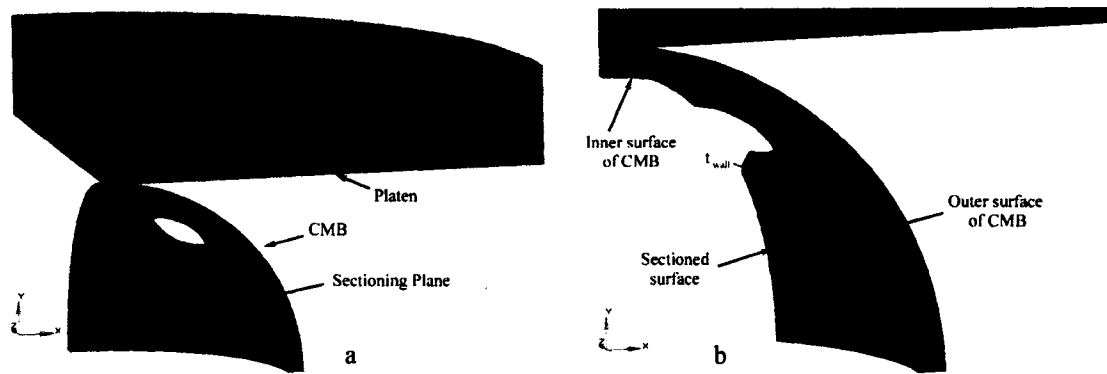
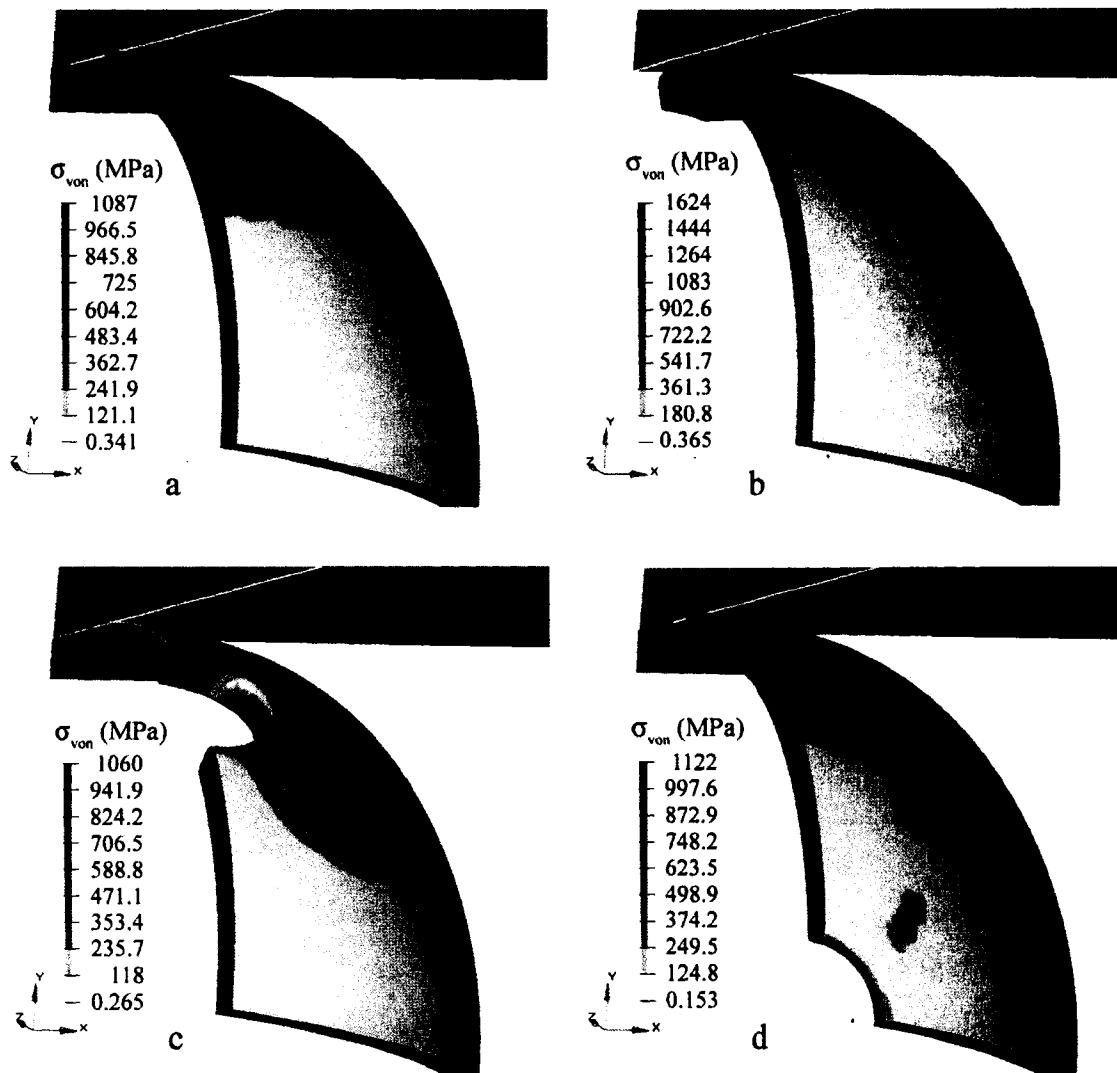


Figure 5  $\sigma_p$  distribution for CMB of  $R = 20 \mu\text{m}$  and  $t_{\text{avg}} = 1.67 \mu\text{m}$ . (a) Uniform  $t_{\text{wall}}$ , (b)  $t_{\min} = 1.6 \mu\text{m}$ , (c)  $t_{\min} = 1.2 \mu\text{m}$ , (d)  $t_{\min} = 0.9 \mu\text{m}$ , (e)  $t_{\min} = 0.6 \mu\text{m}$ , (f)  $t_{\min} = 0.2 \mu\text{m}$ . The maximum principal stress decreased slightly as  $t_{\min}$  decreased until buckling occurred.



*Figure 6* Schematic of 3D models. (a) Full model, showing hole and sectioning plane, and (b) Zoomed view of cut surface. The CMB, platen, and other relevant features are labeled.



*Figure 7* Effect of hole position on  $\sigma_{\text{von}}$ . (a) No hole, (b) hole centered on y-axis, (c) hole at 45°, (d) hole at  $y = 0$  plane. The presence of the hole intensifies the maximum stress level, more so when the hole is positioned in regions of the highest stress in (a).

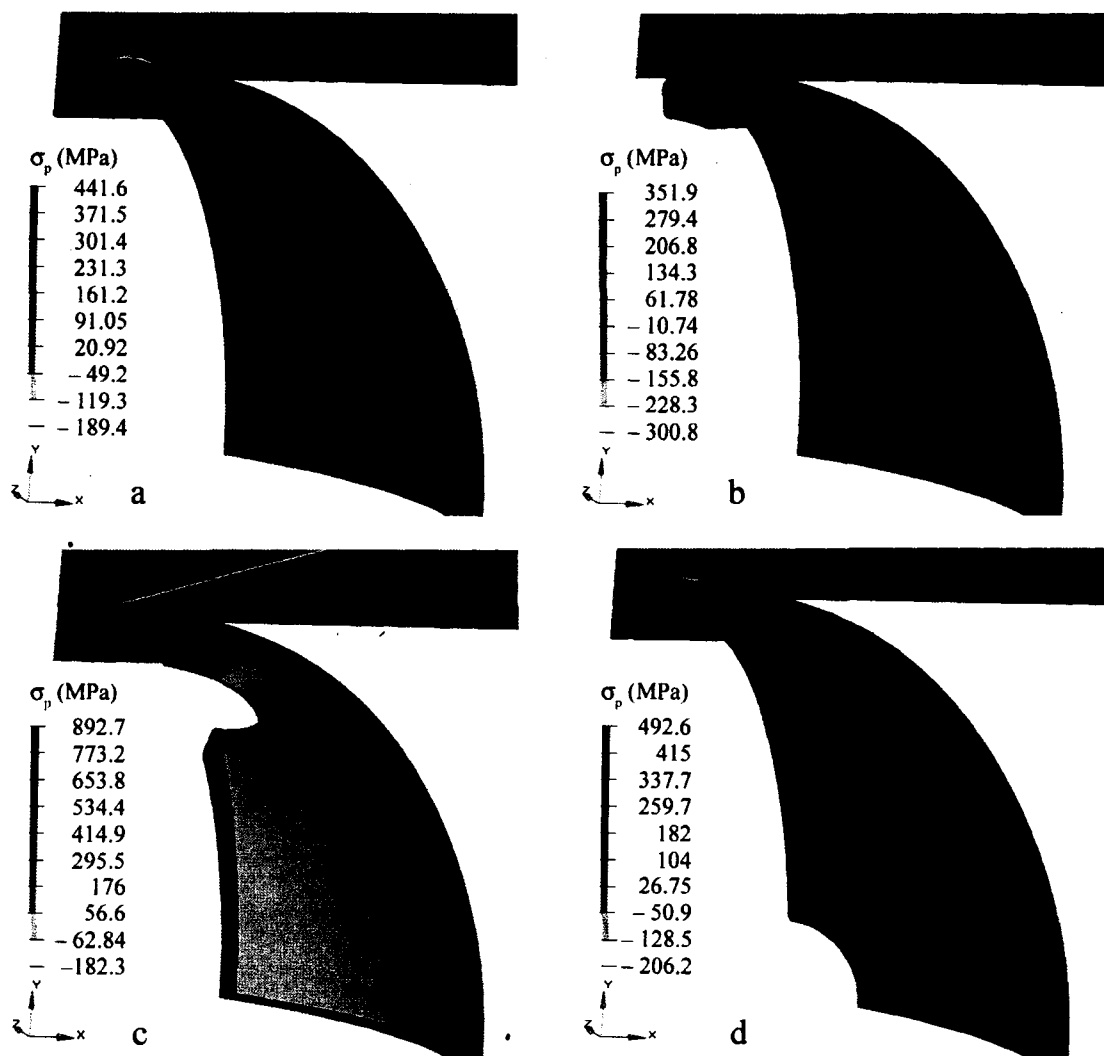


*Figure 8* Effect of hole position on  $\sigma_p$ . (a) No hole, (b) hole centered on y-axis, (c) hole at 45°, (d) hole at  $y = 0$  plane. The presence of the hole intensifies the maximum stress level, more so when the hole is positioned in regions that possessed higher stresses in (a).

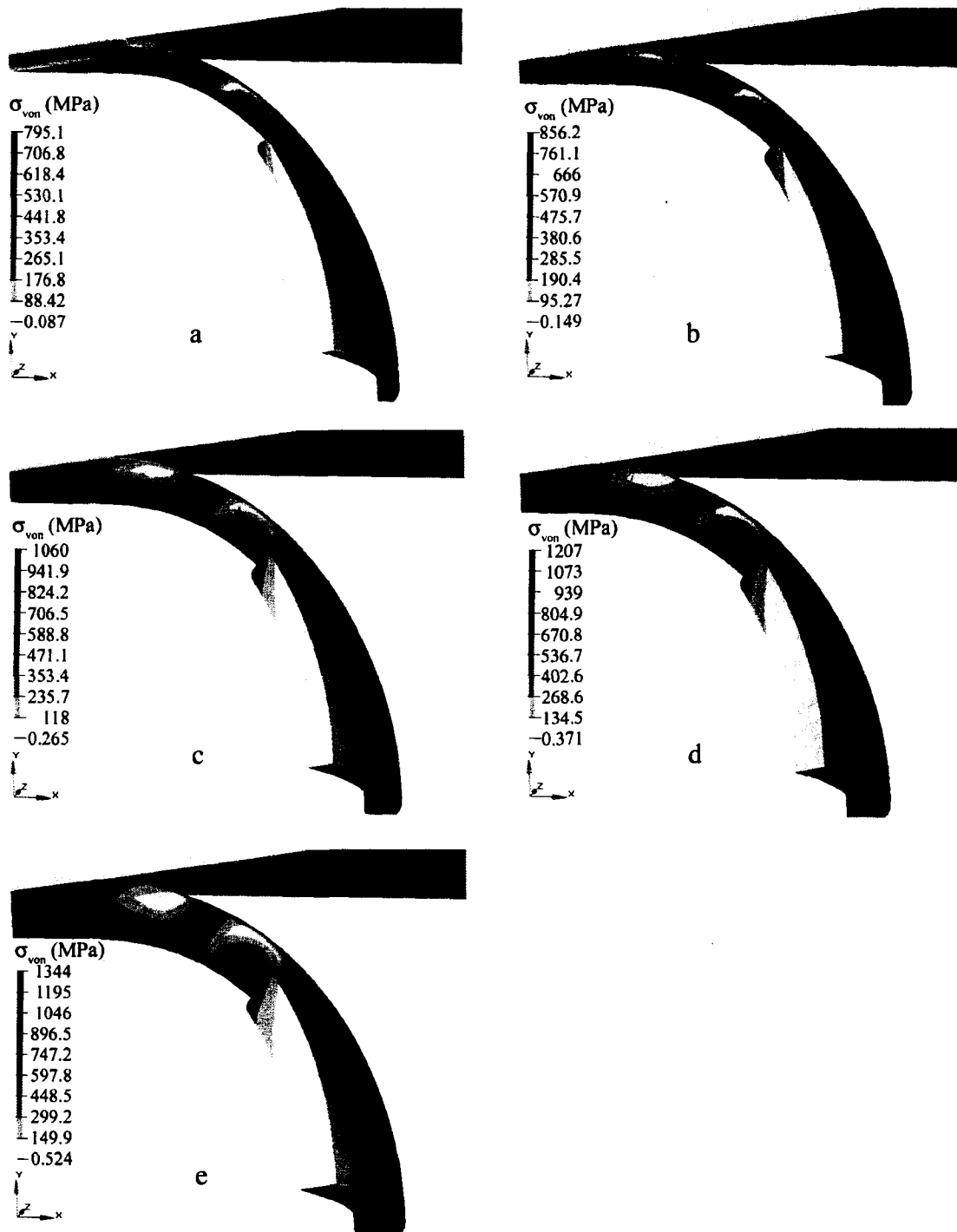


*Figure 9* Effect of varying wall thickness on  $\sigma_{von}$  distribution around hole in MB wall. (a)  $t_{wall} = 0.85 \mu\text{m}$ , (b)  $t_{wall} = 1.2 \mu\text{m}$ , (c)  $t_{wall} = 1.67 \mu\text{m}$ , (d)  $t_{wall} = 2 \mu\text{m}$ , (e)  $t_{wall} = 2.4 \mu\text{m}$ . The maximum stress intensity increased with wall thickness.

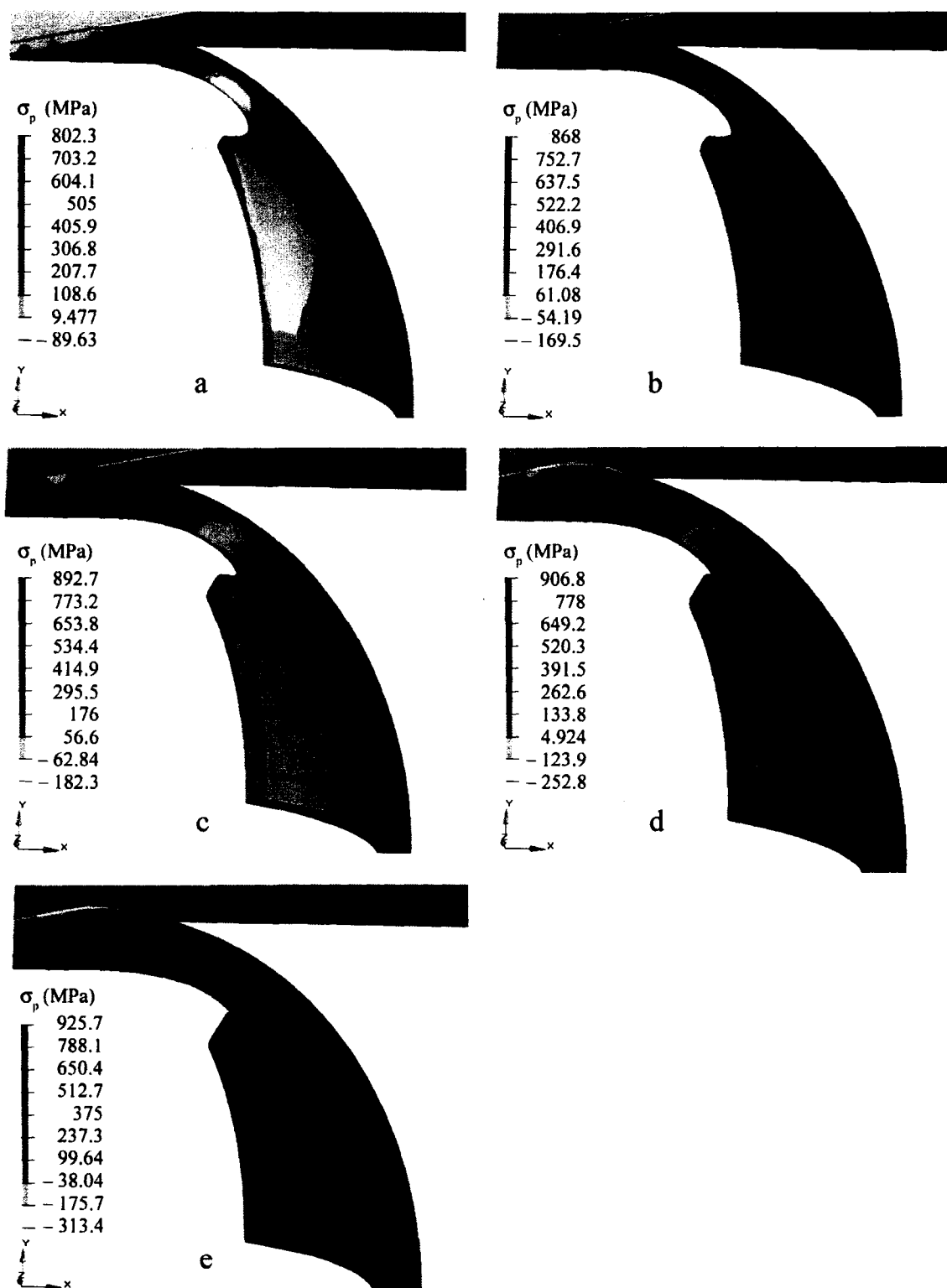


**Figure 10** Effect of varying wall thickness on  $\sigma_p$  distribution around hole in MB wall. (a)  $t_{\text{wall}} = 0.85 \mu\text{m}$ , (b)  $t_{\text{wall}} = 1.2 \mu\text{m}$ , (c)  $t_{\text{wall}} = 1.67 \mu\text{m}$ , (d)  $t_{\text{wall}} = 2 \mu\text{m}$ , (e)  $t_{\text{wall}} = 2.4 \mu\text{m}$ . The maximum principal stresses were always located at the hole and increased with wall thickness.

## CONCLUSIONS

A combination of differential scanning calorimetry (DSC), impulse excitation, microscopy, innovative nanoindentation adaptations, and finite element modeling (FEM) has provided for a thorough characterization of four tap densities of CMBs and their syntactic foams. We have used optical and electron microscopy to determine the sphericities, wall thicknesses, and diameters of these CMBs. Compressive property characterization was performed using a nanoindenter, both in its native configuration determining Young's modulus via Berkovich indentations and in a novel adaptation to compress individual CMBs. Finally, FEM, using ANSYS 8.0, of the nanoindentation compression test was performed, providing new insights into the deformed shapes and stress distributions present in CMBs under uniaxial compression.

Several conclusions were possible with respect to the CMBs' structural morphology. First was the existence of many irregular CMB shapes, including joined and nested CMBs. Additionally, microscopy proved that there was no correlation between wall thickness and CMB size. However, there was a trend toward increasing average wall thickness with increasing tap density, with the  $0.177 \text{ g/cm}^3$  tap density statistically testing at the 95 percent confidence level as possessing thicker walls than the  $0.143$  and  $0.161 \text{ g/cm}^3$  tap densities. Furthermore, numerous flaws in the materials were identified from SEM and optical imaging, with the two most commonly observed in *single-walled* CMBs being non-concentric internal hollows and through-thickness holes.

From experimental mechanical testing, several trends were observed. Primary among these was that compressive strain at failure was proportional to the inverse three-fifths root of diameter for all tap densities. Additionally, CMB stiffness was found to be linearly related to CMB failure load within any tap density, and, intra-tap density, lower slopes in the linear trends corresponded to higher tap densities. Average properties, namely failure load, fracture energy, and pseudo-stiffness, increased with increasing tap density, although not always with statistical significance. The compressive properties of APO-BMI coated CMBs were seen to follow the same trends as uncoated CMBs, with no statistical difference in properties observed in coated and uncoated CMBs of the same tap density. From this comparison, it was concluded that a thin coating of APO-BMI on the surfaces of CMBs does not affect their compressive properties, thus the compression strength of these three-phase syntactic foams will be due to the CMBs and the binder ligaments connecting them, not to the thin layer of binder on the CMB surfaces throughout the foam. Additionally, comparison of average properties proved single-walled CMBs superior to nested CMBs.

Characterization of the APO-BMI nanoindentation represents the only known mechanical characterization efforts of this material. The Young's modulus of APO-BMI was measured as 6.4 GPa, using both neat and foam samples. Additionally, DSC was performed on neat and *in situ* APO-BMI, from which the melting temperature was seen to be 120 °C and the curing exotherm was observed at 228 and 205 °C for the neat and *in situ* samples, respectively. This difference was hypothesized to be the result of the CMBs catalyzing the curing reaction. It was further supported by the drop in the heat of reaction for the *in situ* samples.

Finite element modeling, using ANSYS 8.0, of the uniaxial compression of *single-walled* CMBs provided very useful results, which helped elucidate many of the trends in the experimental data. From predicted average stress distributions for each tap density, two conclusions were possible: (i) the failure stress values were reasonable for this type of carbon, and (ii) failure most likely initiates on the microballoon's inner wall directly under the contact region. This failure site prediction was in contradiction to postulations in previous work on MBs but more in agreement with results for *macroballoons*. The FE results have also qualitatively described the transitions, from point to circular to annular, of the MB-platen contact and allowed quantitative measurement of the circular contact radius, which varied between 4.497 and 5.580  $\mu\text{m}$  for the average property models.

FE models parametrically varying radius and wall thickness allowed characterization of the critical values for failure by buckling in these CMBs, which was seen to be a parabolic function in R-t space. Based on the R-t values where buckling was predicted and the microscopic observations of these CMBs, buckling was concluded to be a viable failure mechanism. Experimental evidence of two flaw populations was also provided by a dual-slope Weibull plot of the microballoon failure strains, where the lower failure probabilities were attributed to buckling and the higher failure probabilities to failure in flexure.

Simulations of the compression of *single-walled* CMBs with non-concentric interiors or through-thickness holes have delineated the relative detriment of each flaw type. The thin regions in CMB walls, caused by offset internal hollows, tended to produce buckling failures even when the average wall thickness was well above that

critical for buckling of uniform CMBs. Little other increased failure propensity was noted. In the hole modeling results, it was noted that holes did act as stress risers, increasing the maximum stresses in the carbon walls by 3 to 63 percent, depending on the particular location where the hole was modeled. In each hole position, very nearly the maximum stress values in the model were observed at the hole. Comparison of the two types of flaw models revealed that the presence of non-concentricity in a CMB was a more tolerable defect than a through-thickness hole. This is because the holes significantly heighten the stress levels in the material and thus increase the probability of CMB failure more than a moderately thin region in the CMB's wall.

This characterization effort could be more complete, if some additional research and resources were available. Further study should attempt to experimentally confirm the deformation of MBs under uniaxial loading. Compression tests of individual MBs should be performed while optically recording the progression of loading, through the acquisition and use of a traveling microscope/high speed camera. This would either validate or refute the present FE predictions and could be used to eliminate some of the scatter in the compression data. Additional efforts in characterizing the effect of coatings and surface treatments on bonding between binder resins and MBs would be beneficial, potentially allowing for tailoring of the MB-binder interface and the construction of syntactic foams with improved flexural and tensile properties. FEM of the compression of coated MBs and of MB-binder systems is also recommended and would hopefully prove as insightful as has the FEM of the compression of individual CMBs.

## GENERAL LIST OF REFERENCES

1. L.J. GIBSON and M.F. ASHBY, in "Cellular Solids: Structure and properties" (Cambridge University Press, Cambridge, 1997).
2. K. OKUNO and R.R. WOODHAMS, *Cellular Plastics* **10** (1973) 237.
3. G.M. GLADYSZ and K.K. CHAWLA, Composite Foams, in "Encyclopedia of Polymer Science & Technology" (John Wiley, New York, 2004) pp. 267-281.
4. S.T. BENTON and C.R. SCHMITT, *Carbon* **10** (1972) 185.
5. C.R. THOMAS, *Materials Science and Engineering* **12** (1973) 219.
6. H.L. PRICE and J.B. NELSON, *J. Composite Materials* **10** (1976) 314.
7. L. BARDELLA and F. GENNA, *International Journal of Solids and Structures* **38** (2001) 7235.
8. L. BARDELLA and F. GENNA, *International Journal of Solids and Structures* **38** (2001) 307.
9. N. GUPTA, KISHORE, E. WOLDESENBET, and S. SANKARAN, *Journal of Materials Science* **36** (2001) 4485.
10. N. GUPTA, E. WOLDESENBET, and KISHORE, *Journal of Materials Science* **37** (2002) 3199.
11. H.S. KIM and H.H. OH, *Journal of Applied Polymer Science* **76** (2000) 1324.
12. H.S. KIM and P. PLUBRAI, *Composites Part A: Applied Science and Manufacturing* **35** (2004) 1009.
13. G. L'HOSTIS and F. DEVRIES, *Composites Part B: Engineering* **29** (1998) 351.
14. M. PALUMBO and E. TEMPESTI, *Acta Polym.* **49** (1998) 482.
15. M. PALUMBO and E. TEMPESTI, *Applied Composite Materials* **8** (2001) 343.
16. D. RITTEL, *Materials Letters* **59** (2005) 1845.

17. E. RIZZI, E. PAPA, and A. CORIGLIANO, *International Journal of Solids and Structures* **37** (2000) 5773.
18. E. WOLDESENBET, N. GUPTA, and A. JADHAV, *Journal of Materials Science* **40** (2005) 4009.
19. E.M. WOUTERSON, F.Y.C. BOEY, X. HU, and S.-C. WONG, *Journal of Cellular Plastics* **40** (2004) 145.
20. E.M. WOUTERSON, F.Y.C. BOEY, X. HU, and S.-C. WONG, *Composites Science and Technology* **65** (2005) 1840.
21. E.M. WOUTERSON, F.Y.C. BOEY, X. HU, and S.C. WONG, Fracture toughness and impact resistance of syntactic foam, in Proceedings of ANTEC 2003, Nashville, TN, United States (Society of Plastics Engineers, 2003). pp. 1742-1746.
22. T. FINE, H. SAUTEREAU, and V. SAUVANT-MOYNOT, *Journal of Materials Science* **38** (2003) 2709.
23. E.M. WOUTERSON, F.Y.C. BOEY, X. HU, and S.-C. WONG, Effect of the filler content on the specific properties of syntactic foam, in Proceedings of ANTEC 2004, Chicago, IL., United States (Society of Plastics Engineers, 2004). pp. 3176-3180.
24. G. KARST, Novel Processing of High-Performance Structural Syntactic Foams, in Proceedings of 47th International SAMPE Symposium (SAMPE Society, 2002). pp. 492-501.
25. N. GUPTA and W. RICCI, *Materials Science and Engineering: A* **427** (2006) 331.
26. KISHORE, R. SHANKAR, and S. SANKARAN, *Materials Science and Engineering: A* **412** (2005) 153.
27. N. GUPTA and E. WOLDESENBET, *Journal of Cellular Plastics* **40** (2004) 461.
28. N. GUPTA, E. WOLDESENBET, and P. MENSAH, *Composites Part A: Applied Science and Manufacturing* **35** (2004) 103.
29. N. GUPTA and E. WOLDESENBET, *Composite Structures* **61** (2003) 311.
30. N. GUPTA, *JOM* **56** (2004) 342.
31. N. GUPTA, C.S. KARTHIKEYAN, S. SANKARAN, and KISHORE, *Materials Characterization* **43** (1999) 271.

32. N. GUPTA, G. LI, H.D. JERRO, E. WOLDESENBET, and S.-S. PANG, Effect of nano-size clay particles on the flexural properties of syntactic foams, in Proceedings of ANTEC 2004, Chicago, IL., United States (Society of Plastics Engineers, 2004). pp. 1320-1324.
33. N. GUPTA and R. MAHARSIA, *Applied Composite Materials* **12** (2005) 247.
34. N. GUPTA, R. MAHARSIA, and H. DWAYNE JERRO, *Materials Science and Engineering A* **395** (2005) 233.
35. Y.-J. HUANG, L. VAIKHANSKI, and S.R. NUTT, *Composites Part A: Applied Science and Manufacturing* **37** (2006) 488.
36. C.S. KARTHIKEYAN, S. SANKARAN, M.N. JAGDISH KUMAR, and KISHORE, *Applied Polymer Science* **81** (2001).
37. C.S. KARTHIKEYAN, S. SANKARAN, and KISHORE, *Polym Int* **49** (2000) 158.
38. C.S. KARTHIKEYAN, S. SANKARAN, and KISHORE, *Materials Letters* **58** (2004) 995.
39. R. MAHARSIA, N. GUPTA, and H.D. JERRO, *Materials Science and Engineering: A* **417** (2006) 249.
40. M. NARKIS, M. GERCHCOVICH, M. PUTERMAN, and S. KENIG, *Journal of Cellular Plastics* **18** (1982) 230.
41. M. NARKIS, S. KENIG, and M. PUTERMAN, *Polymer Composites* **5** (1984) 159.
42. M. NARKIS, M. PUTERMAN, H. BONEH, and S. KENIG, *Polymer Engineering and Science* **22** (1982) 417.
43. M. NARKIS, M. PUTERMAN, and S. KENIG, *Journal of Cellular Plastics* **16** (1980) 326.
44. M. NARKIS, M. PUTERMAN, and S. KENIG, Three-phase Glass Microballoon-containing Syntactic Foams, in Proceedings of 38th Annual Reinforced Plastics/Composites Institute, Society of the Plastics Industry, RP/C '83: Composite Solutions to Material Challenges., Houston, TX, USA (SPI, New York, NY, USA, 1983). p. 8.
45. M. PUTERMAN, M. NARKIS, and S. KENIG, *Journal of Cellular Plastics* **16** (1980) 223.
46. E. BRUNETON, C. TALLARON, N. GRAS-NAULIN, and A. COSCULLUELA, *Carbon* **40** (2002) 1919.

47. G.W. MCEACHEN, Carbon Syntactic Foam Mechanical Properties Testing. Topical Report: KCP-613-6043. (Kansas City) 1998.
48. G.M. GLADYSZ, B. PERRY, G. MCEACHEN, and J. LULA, *J. Mater. Sc.* **41** (2006) 4085.
49. M. KOOPMAN, K.K. CHAWLA, G. GLADYSZ, and K.B. CARLISLE, *J. Mater. Sci.* **41** (2006) 4009.
50. K. MASTERS, in "Spray Drying Handbook" (John Wiley and Sons, New York, 1991).
51. F. VEATCH and R.W. BURBANS, Process of Producing Hollow Particles and Resulting Product. (The Standard Oil Company, United States, 1953). US Patent 2,797,201.
52. V.S. SHABDE, S.V. EMETS, U. MANN, K.A. HOO, N.N. CARLSON, and G.M. GLADYSZ, *Computers & Chemical Engineering* **29** (2005) 2420.
53. D.L. WILCOX, SR. and M. BERG, Microsphere fabrication and applications: An overview, in Proceedings of Materials Research Society Symposium 1995, Boston, MA, USA (Materials Research Society, Pittsburgh, PA, USA, 1995). pp. 3-13.
54. M. SHARON, K. MUKHOPADHYAY, K. YASE, S. IJIMA, Y. ANDO, and X. ZHAO, *Carbon* **36** (1998) 507.
55. K. ESUMI, S. ESHIMA, Y. MURAKAMI, H. HONDA, and H. ODA, *Colloids and Surfaces A: Physicochemical and Engineering Aspects* **108** (1996) 113.
56. H. SUGII, K. ESUMI, H. HONDA, and H. ODA, *Carbon* **33** (1995) 821.
57. B.J. BRISCOE, K.K. LIU, and D.R. WILLIAMS, *Journal of Colloid and Interface Science* **200** (1998) 256.
58. K.K. LIU, D.R. WILLIAMS, and B.J. BRISCOE, *Physical Review E.* **54** (1996) 6673.
59. K.K. LIU, D.R. WILLIAMS, and B.J. BRISCOE, *Journal of Physics D: Applied Physics* **31** (1998) 294.
60. T. LIU, A.M. DONALD, and Z. ZHANG, *Materials Science and Technology* **21** (2005) 289.
61. N.K. GUPTA, G.L.E. PRASAD, and S.K. GUPTA, *Thin-Walled Structures* **34** (1999) 21.

62. F. PETKUNAS, The Properties and Applications of, Syntactic Foam SF-1 Potting Compound as used in Sabre Electronics. Topical Report: E-1844. 1965.
63. P.B. RAND, *Journal of Cellular Plastics* 9 (1973) 3.
64. P.B. RAND, *Journal of Cellular Plastics* 14 (1978) 277.
65. B. SONG, W. CHEN, T. YANAGITA, and D.J. FREW, *Composite Structures* 67 (2005) 289.
66. K.B. CARLISLE, K.K. CHAWLA, G.M. GLADYSZ, and M. KOOPMAN, *J. Mater. Sci.* 41 (2006) 3961.
67. K.B. CARLISLE, M.C. KOOPMAN, K.K. CHAWLA, R.K. KULKARNI, G.M. GLADYSZ, and M. LEWIS, *J. Mater. Sci.* 41 (2006) 3987.
68. G. CHAVEZ, M. LEWIS, and L. LENKE, *Journal of Materials Science* 41 (2006) 4015.
69. V. SHABDE, K. HOO, and G. GLADYSZ, *Journal of Materials Science* 41 (2006) 4061.